AD
A038438

MICROCOPY RESOLUTION TEST CHART
NATIONAL BUREAU OF STANDARDS-1963-A

Final Report

INK JET PRINTING SYSTEM — ANALYTICAL COMPUTER MODEL AND MODEL VERIFICATION

By: S. H. JOHNSON
C. M. ABLOW
D. G. FALCONER
R. L. KIANG
S. D. RAMSEY, Jr.

DDC

RECEIVED

APR 19 1977

D

STANFORD RESEARCH INSTITUTE
Menlo Park, California 94025 · U.S.A.

REPORT DOCUMENTATION PAGE		READ INSTRUCTIONS BEFORE COMPLETING FORM
1. REPORT NUMBER	2. GOVT ACCESSION NO.	3. RECIPIENT'S CATALOG NUMBER
4. TITLE *(and Subtitle)* INK-JET PRINTING SYSTEM – ANALYTICAL COMPUTER MODEL AND MODEL VERIFICATION		5. TYPE OF REPORT & PERIOD COVERED Final
		6. PERFORMING ORG. REPORT NUMBER SRI – ISU-2055
7. AUTHOR(s) S. H. Johnson, R. L. Kiang C. M. Ablow, S. D. Ramsey, Jr. D. G. Falconer,		8. CONTRACT OR GRANT NUMBER(s) DAAB03-72-C-0292
9. PERFORMING ORGANIZATION NAME AND ADDRESS Stanford Research Institute Menlo Park, CA 94025		10. PROGRAM ELEMENT, PROJECT, TASK AREA & WORK UNIT NUMBERS
11. CONTROLLING OFFICE NAME AND ADDRESS Department of Defense Fort George G. Meade, MD 20755		12. REPORT DATE 30 June 1972 to 15 August 1973
		13. NUMBER OF PAGES 169
14. MONITORING AGENCY NAME & ADDRESS*(if different from Controlling Office)* Final rept. 30 Jun 72 – 15 Aug 73,		15. SECURITY CLASS. *(of this report)* Unclassified
		15a. DECLASSIFICATION/DOWNGRADING SCHEDULE
16. DISTRIBUTION STATEMENT *(of this Report)* Approved for public release; distribution unlimited.		
17. DISTRIBUTION STATEMENT *(of the abstract entered in Block 20, if different from Report)*		
18. SUPPLEMENTARY NOTES		
19. KEY WORDS *(Continue on reverse side if necessary and identify by block number)* Ink-Jet Printing Analytical Computer Model Drop Charging Character Formation		

20. ABSTRACT *(Continue on reverse side if necessary and identify by block number)*

An analytical computer model was created to describe performance of an A.B. Dick Company printing head in a specific configuration. The computer model consists of an executive routine that calls on 11 subroutines; each subroutine treats a particular aspect of the ink-jet printing process. The analytical basis for the subroutine was compared with laboratory observations; modifications and refinements were made as necessary. The resulting program is a useful tool over defined ranges of input conditions; output parameters are predicted with modest →next page

DD FORM 1473 EDITION OF 1 NOV 65 IS OBSOLETE
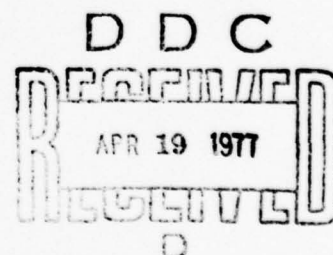1 JAN 73

332 500

UNCLASSIFIED

cont.

accuracy.   Experimental hardware was constructed for testing the program.
Several recommendations for operation of ink-jet printing systems have evolved.
The Analytical Computer Model should be tested under additional combinations
of input conditions to better define its capabilities and limitations.

ABSTRACT

An Analytical Computer Model was created to describe performance
of an A. B. Dick Company printing head in a specific configuration.
The computer model consists of an executive routine that calls on 11
subroutines; each subroutine treats a particular aspect of the ink jet
printing process. The analytical basis for the subroutines was compared
with laboratory observations; modifications and refinements were made
as necessary. The resulting program is a useful analytical tool over
defined ranges of input conditions; output parameters are predicted
with modest accuracy. Experimental hardware was constructed for testing
the program. Several recommendations for operation of ink jet printing
systems have evolved. The Analytical Computer Model should be tested
under additional combinations of input conditions to better define its
capabilities and limitations.

CONTENTS

ILLUSTRATIONS

TABLES

I INTRODUCTION

This final report summarizes all work performed by Stanford Research Institute under a research Contract------,, "Ink Jet Printing System--Analytical Computer Model and Model Verification." The period of this contract was from 30 June 1972 to 15 August 1973. During that time, two major tasks were undertaken. Task I, Creation of the Analytical Computer Model, resulted in a working program to predict ink jet printer operation, based solely on analytical work. This phase of the contract effort was briefly described in the Task I report, dated 15 November 1972. Task II, Verification of the Analytical Computer Model, entailed laboratory measurements and data taking in an effort to verify or refine the program.

This report describes in detail the Analytical Computer Model, including the theoretical basis for analysis and the verification procedures used. Details of the analyses are presented in Appendices A-E. Current performance and limitations of the program are described. Hardware constructed for use in this contract is discussed. A number of recommendations for the operation of ink-jet printing systems are given in the hope that implementation of such recommendations will lead to increased reliability and predictability. Recommendations for future work are also presented. Fiscal data related to this contract are presented in Appendix F (separately bound).

SRI will deliver three items to the client with this final report.

- A copy of the program in punched card form
- A final listing of the program with sample input and output information
- Data Package, including schematics of electrical circuits, mechanical drawings, and sample data taken during the program verification procedures.

1

II SUMMARY

SRI has created an Analytical Computer Model as a useful tool to describe performance of the A. B. Dick printing head in the client's configuration. The work was done in two phases: the first phase dealt with analysis of physical phenomena; the second phase included experimental tests and observations that were used to modify or refine the analytical work.

The Analytical Computer Model consists of an executive routine calling on 11 subroutines. The program user provides input data to the model and receives predictions of drop behavior (see Section III-A,B,C). Numerous optional output branches in the program allow review of drop motion and subroutine behavior while the drops are in flight. Program structure and operation are straightforward, following the sequence in which physical events occur. Ink drops are created by the print head and are incremented through space to an imaginary printing surface.

Each subroutine treats a particular aspect of the ink-jet printing process. Creating and verifying the subroutines (Section III-D) was the primary task of this project. The subroutines together form the Analytical Computer Model; the executive routine calls them at the appropriate time and transfers information among them.

The overall program is a functioning tool that delivers predictions of drop behavior with modest accuracy (Section IV). Drop characteristics and initial velocity are predicted within ±3 percent under all input conditions. Drop deflection distances are predicted within + 10 percent to - 20 percent in the cases studied so far. In some cases, deflections are

3

predicted within ±3 percent. The largest errors occur when deflection plate angle is large. The main cause of the errors is the nonideal geometry of the deflecting plates. Random errors in the predictions result from the approximations made to permit analytical study.

Accurate prediction of drop separation point was achieved under only a few conditions; in most cases, the predicted distance from the orifice is too small. The source of this error was the difficulty in treating every detail of jet perturbation and breakup and in accounting for the mechanical intricacies of the print-head assembly.

Limitations on the values of the input parameters (identified in Section V) are based primarily on experimental observations and practical considerations. The limits are contained within the computer model; warning messages or program termination result when they are exceeded.

Experimental hardware was constructed for verifying the analysis (Section VI). The hardware permitted adjustment and measurement of input and output parameters. Drops in flight could be observed under stroboscopic illumination. A charging signal could be delivered to the charging electrode in the same manner as it was presented to the computer model.

The analysis and experimental work resulted in numerous recommendations for system operation (Section VII). These indicate the conditions under which the apparatus and the model perform best. They should also serve to upgrade reliability of ink-jet printing systems.

The overall computer model has been tested under only a few experimental conditions. The individual subroutines, however, have a broader experimental base. To better define the capabilities and limitations of the Analytical Computer Model, it is suggested that comparisons between computer predictions and observations be made over a wide range of input conditions (Section VIII).

4

III ANALYTICAL COMPUTER MODEL

An Analytical Computer Model was created for an ink-jet printing system in the client's configuration. This assembly consists of an A. B. Dick ink jet printing head with charging electrode (Part No. 338018), plus deflecting plates of the client's design (Drawing ONO-71606). The assembly is shown in Figure 1. The ink collector shown in the figure was not used during SRI's work, since it was frequently necessary to observe the ink drops in flight at distances from the orifice greater than that to the collector.

The computer program treats the printing process in the same sequence that the physical events occur. Ink is forced under pressure through a small orifice that is vibrated axially by two piezoelectric crystals. The crystal vibrations create a pressure disturbance in the ink within the metal tube that supports the orifice. The pressure disturbances are transformed into velocity perturbations as the ink passes through the orifice; these velocity perturbations are superimposed on the mean jet velocity. The perturbations cause the jet to break up into uniform drops. As each drop separates from the jet, it traps an induced charge (or zero charge) on its surface, depending on the potential applied to the charging electrode at the moment of separation. The drops then pass into an electrical deflecting field, in which the charged drops are deflected from the normal jet trajectory. By appropriately manipulating the charging voltages and deflecting field, drops can be deflected to print characters on surfaces moving rapidly past the printer.

The computer model contains analytical treatment of all aspects of the printing process that were found to be necessary and that could be

5
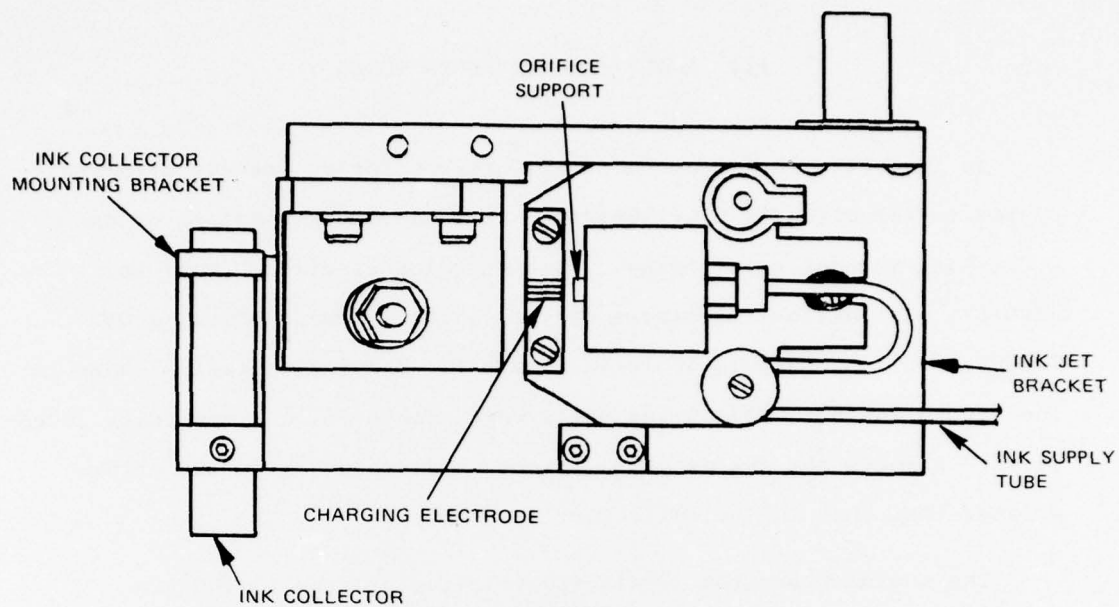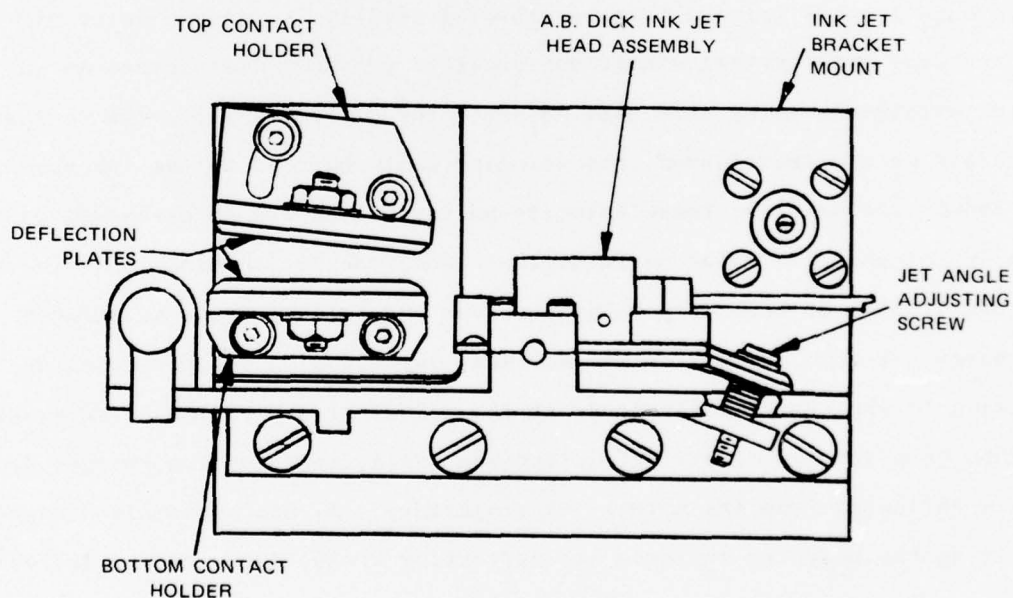
FIGURE 1   INK-JET PRINTING STATION

SA-2055-3

6

approached within the time and budget limits of the contract. Topics that were not considered and assumptions that were made also are discussed in the report.

The approach used in developing the Analytical Computer Model was as follows. The physical processes were broken down as far as possible into separate events. Each event led to a separate subroutine in the program. For each event, an initial analysis was performed. In some cases, such as describing orifice behavior, the analysis was based on conventional fluid mechanics. In other cases, the first analysis was based on original work performed under this contract or on prior work in the ink-jet printing field. When these analyses were completed, the first version of the Analytical Computer Model was assembled and run. The work just described was conducted under Task I of the contract.

During Task II, numerous laboratory experiments were performed to check the agreement between the program predictions and the physical values that were measured. Refinements in the analysis then were made on the basis of the measurements. In some cases, such as that of orifice performance, the measurements simply led to determination of orifice coefficients. In other cases, such as predicting drop separation point, laboratory tests indicated flaws in the original analysis and led to quite different computing routines. Computer model verification also led to defining limits for which the model was valid.

The analytical basis for each subroutine and the verification procedures used are discussed in detail in Section III-D, Subroutine Description and Verification, and in Appendices A through E.

The computer program is written in FORTRAN IV language and was developed on SRI's CDC-6400 computer facility. The text of the program is liberally filled with comment cards to make reading and understanding

of the program easier. All variables used in the subroutines, including units, are explicitly defined within the subroutines themselves.

A.   Flow Chart

Figure 2 is a flow chart of the Analytical Computer Model. It shows the order in which the subroutines are used, together with the logical program branches. The primary function of each subroutine is noted. Input and output points during the program are indicated. The executive routine is used to call the subroutines and to perform functions that are not part of a subroutine. Most numerical calculations are performed within the subroutines themselves, with data communicated to and from the executive routine as necessary. Limit checks are performed within the subroutines, with error messages and possibly program termination whenever critical limits are exceeded.

B.   Program Operation

Operation of the program is quite straightforward. For a given combination of operating point variables, the numerical values of the input parameters are read in on punched cards. The program then manipulates the input parameters via the executive routine and the subroutines to arrive at numerical values for the output parameters. Program output normally consists of two printed pages. On the first page the input variables are defined in words and their values with units given. The second page lists the corresponding output variables with their unit values.

As seen in the flow chart, the program can be considered as two large segments, each containing several subroutines. The first segment deals with the formation and charging of the drops. Here the program calls the subroutines in straight sequence, following the sequence of physical events. The second segment of the program deals with drop

8

ENTER EXECUTIVE ROUTINE

SET VALUES—
MAXPTS = NUMBER OF DROPS TO BE CREATED
NDAT = MAXIMUM POSSIBLE NUMBER OF DROPS

CALL DATIN
READ IN INPUT VARIABLE VALUES, COMPUTE INK PROPERTIES, CONVERT ALL VALUES TO MKS UNITS

PRINT INPUT VARIABLES

INPUT VARIABLES
INK TYPE
INK TEMPERATURE
INK SUPPLY PRESSURE
VOLTAGE APPLIED TO PZ CRYSTALS
FREQUENCY OF CRYSTAL VOLTAGE
CHARGING ELECTRODE SPACING
DEFLECTION PLATE LENGTH
DEFLECTION PLATE SEPARATION
DEFLECTION PLATE ANGLE
DEFLECTION PLATE VOLTAGE
ORIFICE-TO-PAPER DISTANCE
DROP CHARGING VOLTAGES

CALL ORIFIC
COMPUTE JET VELOCITY AND FLOW RATE

PRINT OUT VALUES FROM ORIFIC (Optional)

CALL JETPER
COMPUTE VELOCITY PERTURBATION IN JET; COMPUTE DROP SIZE, MASS, RATE, AND SPACING

PRINT OUT VALUES FROM JETPER (Optional)

CALL SEPDIS
COMPUTE DROP SEPARATION POINT

PRINT OUT VALUES FROM SEPDIS (Optional)

PRINT OUT DROP CHARACTERISTICS (Optional)

CALL CHARGE
COMPUTE CHARGE ON MAXPTS NUMBER OF INK DROPS

COMPUTE TIME INTERVAL FOR DROP STEPPING

INITIALIZE DROP COUNTER NPTS = 0

HAVE DESIRED NUMBER OF DROPS BEEN CREATED? (NPTS = MAXPTS)   Yes / No

INCREMENT COUNTER NPTS = NPTS + 1

CALL CREATE
CREATE AN INK DROP AND INITIALIZE ITS STATE VECTOR

(NPTS = MAXPTS)

ARE ANY DROPS NEAR PAPER?   Yes / No

USE SHORT TIME INTERVAL FOR DROP SETTING

USE LONG TIME INTERVAL FOR DROP STEPPING

FIGURE 2   FLOW CHART FOR INK JET PRINTER COMPUTER MODEL

SC-2055-1R

ballistics. In this part, the drops are stepped through space in small increments to an imaginary printing surface. The subroutines in this segment are called many times to account for the motion and forces on each drop during flight.

In the flow chart, several optional print statements are included in the program in addition to the primary outputs. The optional outputs, when used, deliver interim values from either the executive routine or from several of the subroutines. These interim outputs have been used throughout the verification procedures to indicate the predictions and performance of individual subroutines and to describe drop motion and imposed forces through flight. Because this information was quite valuable during this project, the capacity for interim output is still included. When interim values are delivered, they appear between the listings of input and output variables.

Within the executive routine, setting the logical variable, IPRT = 0, suppresses optional printout from the executive routine. If IPRT = 1, the executive routine will deliver values of position, velocity, and acceleration of all the drops and the forces acting on the drops as they travel from the orifice to the paper. Within the subroutines, variable values can be printed via the optional PRINT statements. Printing is suppressed by inserting the letter C in Column 1 of the print card so that the computer sees a comment instead of a PRINT command.

In selecting a system of units for the computer model, both experimental convenience and computational ease had to be considered. For experimental purposes, it is most advantageous to work with common laboratory units. Variables can thus be measured with typical measuring apparatus in everyday units. However, to avoid computational difficulties and unit conversions within the program, it is most desirable to work with a single system of units. To do this, numerical values are inputted to and

11

outputted from the program in typical laboratory units. Immediately after input they are converted to rationalized meter-kilogram-second (MKS) units, and immediately before output they are converted back to laboratory units. All computations are done in the rationalized MKS system of units. As an example of this process, pressure of the ink upstream from the orifice is measured in pounds-force per square inch, but at input the numerical value is converted to newtons per square meter.

As the flow chart shows, a number of input parameter values are given to the program to describe the operating points of interest. These are provided in punched card form and are read during the DATIN subroutine. Several other parameters also have an effect on printer operation and must be given to the computer model. These include orifice diameter, air density, and other properties. These parameters are held constant. They are explicitly defined within the appropriate subroutines, with numerical values given in MKS units.

When interim values are delivered via the print options, they are always given in MKS units. Interim values are never converted to laboratory units before output.

Two integer variables of importance are set via data cards within the executive routine. The first is NDAT. This number should be equal to or greater than the maximum number of drops that will ever be studied, and less than or equal to the first dimension of the arrays STATE, STATIC, DRAG, REPEL, DRCHLV, and DRDFDS in the executive routine. NDAT is used only to set the size of the storage arrays that contain values for drop position and dynamics and values of force components acting on the drops. The second variable is MAXPTS. This number is equal to the number of drops to be considered during a particular data run. For example, if MAXPTS = 15, fifteen drops will be created and propagated through space to the imaginary printing surface.

After submission of the Task I report with an initial version of the punched card deck, it became evident that several notations used on the SRI computer facility were not compatible with the client's computer. Most of these difficulties concerned logical expressions and output formats. In all such cases, the coding used by the SRI facility was changed so that the program would be as computer-independent as possible.

C.   Character Formation

For an ink jet printer to be useful, it must be able to print machine- or human-readable characters. Under this contract, however, the main objective was to go only so far as to develop a capability to predict drop behavior. Such a capability is directly related to character formation, since characters are formed from sequences or matrices of drops.

As an example, consider printing the letter "L" within a 6 by 4 drop matrix. The vertical stroke would correspond to a decreasing "staircase" of 6 charging voltages applied to the first six drops. In the next 3 columns of the matrix, only the sixth drop in each would be charged and deflected. Thus, an "L" would be formed from applying a discrete charge to drops 1 through 6 and to drops 12, 18, and 24. In the computer program, such a sequence of charging voltages will lead to predictions of drop deflection distance and arrival time at an imaginary printing surface. With such information, the resulting character shape can be visualized.

The hardware built for verification of the computer model permits a repeating sequence of 24 selectable charging voltages to be applied to the ink drops as they separate from the jet. This then permits characters or components of characters to be observed in flight and at an imaginary printing surface. Thus, although specific characters were not printed

13

under the contract, predictions of character appearance and observation of drop patterns have been realized. Printing characters would then require only the appropriate charging signal and a surface to print on.

D.   Subroutine Description and Verification

The program executive routine calls on 11 subroutines in the printer analysis. One of these in turn calls on a function routine. The subroutines contain the analytical tools used in manipulating the input variables to arrive at the output parameter values. The executive routine also contains calculating steps.

The ink jet printing process was broken down into as many discrete events as possible, with a subroutine treating each event. For each event, an analysis was performed. Based on the original analysis, a computing subroutine was written. This formed the substance of the Task I effort. During Task II of this project, all necessary subroutines were checked against experimental observations, with modifications made to the program as required. This section of the report describes in detail the analytical basis for each subroutine and the verification procedures used. Pertinent results and conclusions related to the individual subroutines are given below, with overall program performance discussed in Section IV. Subroutine limitations are mentioned, with the individual discussions when appropriate; overall program limits are discussed in Section V.

1.   DATIN

DATIN is used to read or compute the input parameter values that describe the operating point of interest. The input values are recorded on user-made punched cards and contain the following information:

14

- Type of ink being used

- Ink temperature, degrees F

- Gauge pressure of the ink, pounds-force per square inch

- Voltage applied to piezoelectric crystals (zero-to-peak), volts

- Frequency of voltage applied to crystals, Hertz

- Charging electrode spacing, inches

- Deflection plate length, inches

- Deflection plate separation, inches

- Angle between deflection plates, degrees

- Deflection plate voltage, volts

- Orifice to printing surface separation distance, inches

- Drop charging voltage, 24 values, volts.

The ink being used is identified by a number corresponding to the A. B. Dick type. The identifying number for each ink is shown in Table 1. After reading the input data cards, the subroutine determines if the ink number is valid. If so, it branches to a series of steps to determine ink properties. If not, an error message is printed and the program stops; ink properties cannot be determined without an acceptable number.

Table 1

A. B. DICK INKS AND IDENTIFYING NUMBERS

Ink Identifying Number	A. B. Dick Ink Type
1000	Videojet Ink, Black, A. B. Dick Type 16-1000
2000	Videojet Ink, Black, Multiple Copy, A. B. Dick Type 16-2000
4000	Videojet Ink, Black, Film Titling, A. B. Dick Type 16-4000
189	Videojet Ink, I. R. Buffered, A. B. Dick Type 70R6-12-189
6000	Videograph, Fast Dry Ink, A. B. Dick Type 16-6000

If the ink number is valid, the following properties are determined for that ink as a function of ink temperature:

- Ink density, grams per cubic centimeter
- Ink surface tension, dynes per centimeter
- Electrical resistivity of the ink, ohm-centimeter
- Viscosity of the ink, centipoise
- Sonic velocity within the ink, meters per second.

For each ink property to be computed, an algebraic expression can be found within DATIN. The expressions are based on data taken under this contract. Twelve pints of each of the five A. B. Dick inks were purchased. For each ink, a measurement of each property was made at approximately 10°F intervals between 50°F and 90°F. This temperature range was chosen (with the client's approval) as typical of most indoor operation. The data were plotted graphically. When the data appeared to follow a straight line, a simple linear expression was derived. When the graphical data exhibited curvature, a second degree polynomial expression was fitted to the curve. A second degree polynomial was thought to be sufficient since none of the properties showed radical changes over the given temperature range.

In measuring the ink properties, density was determined using a simple Westphal specific gravity balance. Although this instrument is designed to be used at 20°C (68°F), the small variation in imposed temperature about this point and the relative constancy of density made a temperature correction to the measurement unimportant. It was found that density change is approximately linear with temperature, and shows only about 1 percent variation over the given temperature range.

Surface tension was measured by noting the rise of ink, within a capillary tube, above a fluid surface. If D is the inside diameter of the capillary, ρ is ink density, g is the acceleration of gravity, and h

16

is the height of rise, then surface tension is found from

$$T = \frac{1}{4} \rho \, Dhg \quad .$$

Unfortunately, this method is not entirely accurate because of the dependence of capillary rise on wettability and surface condition of the tube bore. Although the surface tension from ink to ink showed notable differences, the greatest variation over the given temperature range for a single ink was about 10 percent.

Electrical resistivity was measured using a commercial platinum electrode conductivity cell and an impedance bridge. This test showed a significant variation between inks and with temperature. In all cases, however, the resistivity was found to be relatively low (below 220 ohm-cm).

Viscosity was measured with a Brookfield Synchro-Lectric Viscometer with U. L. adapter. This gave the instrument a range of 0 to 10 centipoise. Viscosity was found to drop rapidly with temperature rise as expected.

Sonic velocity was measured using acoustic apparatus at SRI and a fluid chamber. A sonic pulse was sent from a transducer through the fluid to a reflector that returned the pulse to the transducer. By measuring the pulse transit time and path length, sonic velocity could be calculated. Sonic velocity was found to rise with temperature, as expected, although the variation was only about 2 percent over the given temperature range.

Graphs of the original data from the above tests are included in the Data Package.

17

As an independent check on the SRI property measurements, we were supplied with a copy of A. B. Dick test data on ink 16-6000.[1*] The company's data for new ink and our data were in agreement with less than 3 percent difference.

Our measurements of ink properties were taken on new samples after approximately three months' storage. No measurements were taken on any inks after longer storage periods or after use. It was assumed that ink properties would not change appreciably over moderate (several months) storage times. Also, the A. B. Dick report[1*] gives evidence of only small changes (~ 10 percent or less) in ink properties with use.

Once the ink properties have been computed, DATIN goes through three steps with each input variable. It:

- Prints the input variable value, with units
- Performs a limit test on the value, if necessary
- Converts the value to MKS units, if necessary.

In the limit test operation, the input parameter values are compared with minimum or maximum values based on the physical apparatus or on experimental findings. For example, charging electrode spacing cannot exceed 0.120 inch because of geometric construction of parts; charging voltage should not exceed 400 volts because of the effects of high surface charge on jet breakup. The limits used are described more fully in the discussion of subroutines that follow.

Whenever a limit is exceeded in the DATIN tests, a warning message is printed, but the program continues to run. Thus, the input values can be varied beyond the normal limits, with a note to the user that such has happened.

---

* Superscripts refer to references listed at the end of this report.

The only limits related specifically to DATIN are those for ink temperature. If ink temperature is less than 50°F or greater than 90°F, a warning message is delivered. This is because ink properties were measured and curve-fit only between these temperatures. As ink temperature rises beyond these limits, increasingly large errors will be incurred.

After DATIN has printed, tested, and converted units for the input parameters, control is returned to the executive routine. The executive routine immediately branches to ORIFIC subroutine.

2. ORIFIC

ORIFIC is used to compute the velocity and flow rate of ink through the orifice.

The analytical basis for this subroutine lies in the traditional fluid mechanics equations regarding orifice flow. Velocity of the jet is a function of pressure differential across the orifice, fluid density and surface tension, jet diameter, and flow losses. Pressure differential is the excess of upstream gauge pressure over residual pressure in the free jet from surface tension forces. Flow losses are taken into account via a velocity coefficient. Thus, the expression for jet velocity is

$$v_{jo} = C_v \sqrt{\frac{1}{\rho}\left(2P_g - 4\frac{\sigma_i}{d_{jo}}\right)} \quad ,$$

where

$\quad v_{jo}$ = jet velocity outside of orifice

$\quad C_v$ = velocity coefficient

$\quad \rho$ = fluid density

19

P_g = gauge pressure upstream from orifice

σ_i = surface tension of ink

d_{jo} = jet diameter.

With jet velocity known, flow rate is found by multiplying velocity and jet cross-sectional area. Jet area is not the same as orifice area because of the vena contracta phenomenon. This contraction is described through a contraction coefficient. Thus,

$$Q = C_c \frac{\pi}{4} D_o^2 v_{jo}$$

where

Q = flow rate

C_c = contraction coefficient

D_o = orifice diameter.

To verify this subroutine, it was necessary to accurately measure Q, v_{jo}, and P_g so that the orifice coefficients could be determined. Jet velocity was measured by breaking the stream into uniform drops, as in actual printer operation. By observing drop-to-drop spacing near the orifice under a microscope and knowing drop rate, jet velocity is found from the expression

$$v_{jo} = f\lambda \quad,$$

where

f = drop rate, drops/sec

λ = drop spacing, inches/drop.

20

Flow rate was measured by catching and weighing a sample taken during a timed interval. This method was found to be more accurate than simply catching a sample in a graduated cylinder. Ink supply pressure was measured by a pressure gauge; the gauge was connected to the ink line via a "T" at the entrance to the printing head.

It was also necessary to know the diameter of the orifice in the printing head being used. This was done on a precision measuring microscope with 0.5 μ divisions. After observing several printing heads, several facts were apparent:

- None of the holes was perfectly round; major and minor diameters varied by from 1 μ to 5 μ.
- The "mean" orifice diameter varied by as much as 12 μ between printing heads.
- Some of the orifices had small chips on the outer edges.

The A. B. Dick Company quality control specification on orifice diameter is such that, with a supply pressure of 43 psig, a flow rate of 3.78 ml/min to 4.04 ml/min must be observed. Thus, variation in orifice diameter is acceptable. It is also expected that the orifice coefficients will vary from assembly to assembly; a small orifice could be acceptable if the coefficients were large and vice versa.

For work under this contract, a printing head with the roundest, most chip-free orifice was selected. Its mean diameter was 77.6 μ; at 43 psig, a flow rate of 3.95 ml/min was observed.

During verification of this subroutine, data showed that the orifice coefficients varied slightly with Reynolds number, as was expected. Reynolds number for orifice flow, $R = vd\rho/\mu$, is taken in the ink supply tube just upstream from the orifice. A graph showing the variation in C_c and C_v with Reynolds number is provided in Figure 3. When these data were plotted on log-log paper, it was found that the data could be approximated by a straight line. This discovery lent itself to the empirical

21
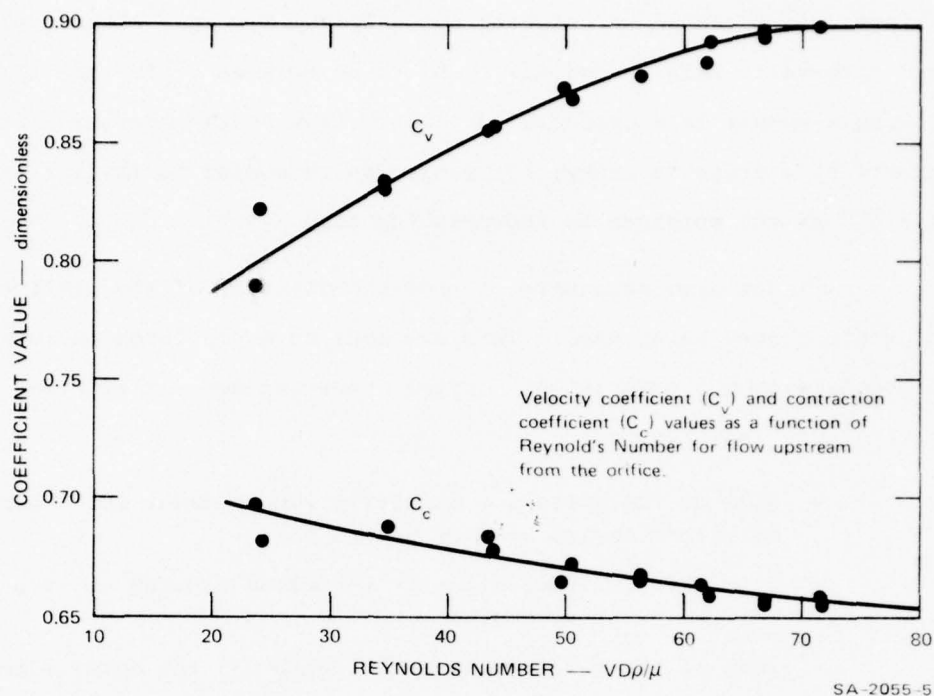
FIGURE 3   ORIFICE COEFFICIENTS VERSUS REYNOLDS NUMBER

expressions for orifice coefficients as a function of Reynolds number appearing in the program. It was also necessary to relate Reynolds number from the tests to ink supply pressure. This required another log-log plot and resulted in a third empirical expression with ORIFIC.

To actually compute jet velocity and flow rate, it is first necessary to compute the coefficient values. Since these are a function of Reynolds number, which is a function of flow, an iterative approach was required. In ORIFIC, a Reynolds number from the experimental work, based on input pressure, is calculated. This value is then corrected to account for the density and viscosity of the ink in the model. A loop then calculates velocity and flow rate based on the modified Reynolds number and then determines the Reynolds number for the predicted flow. When the two Reynolds numbers agree within a small difference, the correct

22

values of jet velocity and flow rate are known. Tests of the ORIFIC subroutine show convergence to the velocity and flow rate predictions with as few as three iterations.

The study of orifice geometry and coefficient values points to a limitation on the existing program. Namely, for accurate prediction of jet velocity and flow rate, the orifice diameter and expressions for coefficient values for the printing head in use must be determined and used in the program.

In the verification process, accurate measurements of initial jet velocity and flow rate were taken. This information is shown in Figures 4 and 5. For these graphs, the data were taken using A. B. Dick ink type 16-1000 at about 76°F. Other combinations of ink and temperature will cause deviations from the graphs of up to $\pm$ 10 percent. This small deviation shows a relative independence from fluid properties and is characteristic of orifice behavior. This is true in our case because (1) density shows little variation from ink to ink, (2) the pressure induced by surface tension is small compared with ink supply pressure, and (3) ink properties appear in the equations to the one-half or smaller power. Also, the plotted data were taken between 10 psig and 80 psig. Operation at 10 psig or below is impractical because of the low stream momentum. At pressures above 80 psig, the safety of the ink supply system was in doubt and pressed-on tube connections would occasionally separate. Furthermore, at 80 psig and above, the jet is traveling so fast that only small deflection can occur unless the distance to the printing surface is large. A final comment on the graph is that the jet or drop velocity decreases with increasing distance from the orifice because of aerodynamic drag.

The role of ink viscosity should also be mentioned. Viscosity appears only in the expression for Reynolds number, on which the orifice coefficients are weakly dependent. This dependence of orifice behavior

23

SA-2055-6
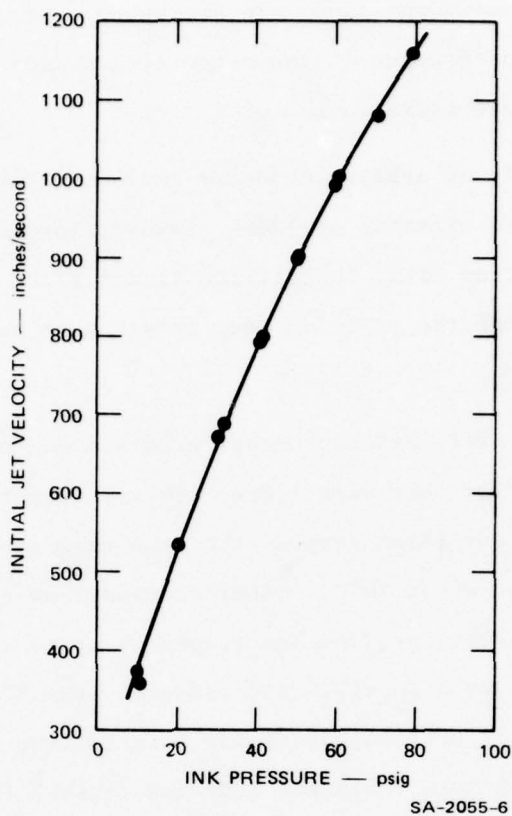
FIGURE 4   JET VELOCITY VERSUS
            PRESSURE

            Data taken with ink type 16-1000 at
            76° F

on viscosity can be inferred from Figure 3, where halving or doubling
the Reynolds number via viscosity change results in only a few percent
change in coefficient value. Thus, viscosity is seen to play only a
minor role in formation of the jet.

        Once initial jet velocity and flow rate are found, control is
returned to the executive routine. An immediate branch is made to the
next subroutine, JETPER.

24
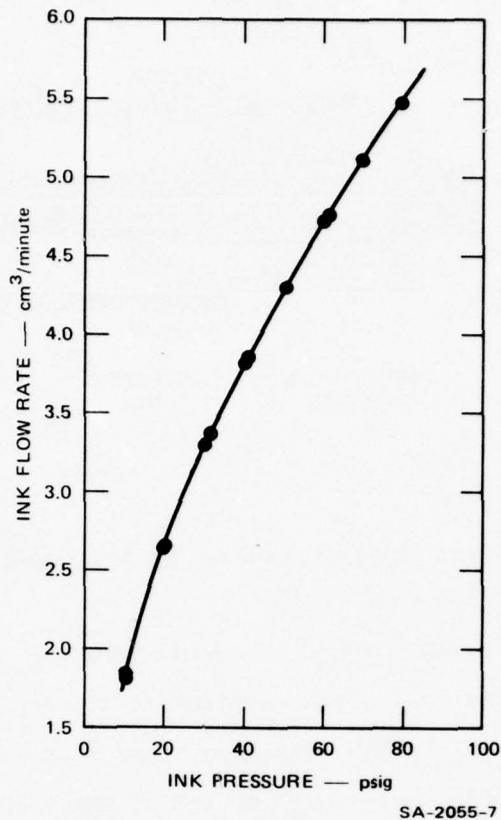
FIGURE 5   INK FLOW RATE VERSUS
PRESSURE

Data taken with ink type 16-1000 at
76°F

3.   JETPER

Ink is supplied to the ink jet head through a flexible plastic
line. The head contains a metal tube for ink passage and has a jewel
orifice in the downstream end. Two piezoelectric crystals surround the
metal tube and are rigidly clamped in an axial direction. The junction
between the crystals contains a thin electrode through which a sinusoidal
signal is presented to them. The outer axial crystal surfaces contact
the grounded ink tube and clamping nut. This physical arrangement is
shown in Figure 6.

25
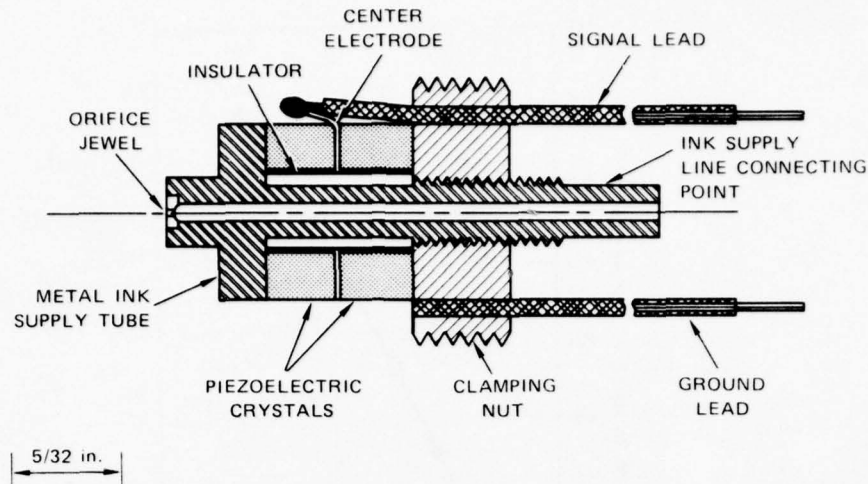
FIGURE 6   CROSS SECTION OF JET PERTURBING APPARATUS

Ink is forced through the metal tube and out the jewel opening as a jet. The sinusoidal signal applied to the crystals creates an axial vibration in the tube. This vibration is coupled to the ink by the jewel orifice, which nearly closes off one end of the tube. The vibrations create a pressure disturbance in the ink column, which in turn causes a velocity perturbation to be added to the mean jet velocity. The purpose of JETPER subroutine is to compute the magnitude of the velocity perturbation. Drop rate, initial spacing, and volume are also computed.

A detailed account of the analytical background for predicting perturbation velocity is given in Appendix A, JETPER Theory. General considerations and assumptions are discussed in the following paragraphs.

The ink in the metal tube is assumed to be a homogeneous column of compressible, inviscid fluid in one-dimensional motion. The fact that viscosity can be neglected is verified in Appendix A. The uniform flow to the orifice is perturbed by a standing wave oscillating at the impressed frequency. The motion of fluid particles in the wave is determined by the relationships between oscillatory pressure and velocity at the two ends of the tube.

26

At the upstream end of the metal tube, a flexible plastic hose leads to the ink supply. Since it is assumed that this hose is unable to sustain high frequency pressure oscillations, the perturbed pressure is assumed to be zero at this end. At the downstream end of the tube, the oscillatory pressure and velocity through the orifice are related by a dynamic equation.[2] The perturbation velocities and pressure in the wave within the tube can then be found once the motion of the orifice is determined. These considerations establish the boundary conditions for the problem.

The geometric arrangement of the printing head is accounted for by referring to Figure 6. The flanged end of the metal tube and the clamping nut are taken as separate masses. They are connected by a thin-wall section of the tube, which acts as a spring in tension. The two piezoelectric crystals lie between the masses and serve as a force input to the mechanical system. The crystals also display compliance. Thus, forces on the clamping nut arise from piezoelectric effects and the tube in tension; forces on the tube flange arise from these sources and also from the oscillating fluid pressure at the orifice. The orifice is rigidly connected to the tube flange. The mechanical assembly shown in Figure 6 is physically supported in a plastic mounting block. Since the block is unresponsive to impressed high frequency vibrations, the mechanical ground for the system is assumed to be the center of gravity of the parts shown in the figure.

The above considerations yield a group of simultaneous differential equations. Solution of this dynamic problem, as described in Appendix A, gives the oscillatory orifice displacement and the flow perturbation due to the voltage signal applied to the crystals. Taking account of the flow contraction through the orifice then gives the amplitude of the initial jet velocity perturbation.

27

A few physical details entailed in the perturbation theory are not treated because of the difficulty in doing so. For example, the amount of energy transferred from the crystals to the orifice tube and clamping nut depends on the mechanical connection. An ideal connection would provide perfectly parallel faces between the crystals, flange, electrode, and nut. Nonparallel faces will reduce the energy transfer and thus result in less velocity perturbation. Another point is that the plastic block that supports the tube will act to absorb some of the mechanical energy coming from the crystals. This, too, has been ignored and would reduce the perturbation magnitude if included.

The presence of resonances in the fluid column should also be mentioned. It is experimentally observable that when the head is excited at certain frequencies, the drop separation point is nearer the orifice than at slightly higher or lower frequencies. Furthermore, these critical frequencies correspond to odd quarter wavelengths of a perturbation within the ink column. This suggests the presence of resonance effects in the fluid column, and consequently the theory has had to include fluid compressibility. The attenuation due to viscosity is shown in *Appendix A* to be negligible, so viscous terms have been dropped. The error in the remaining idealization of one-dimensional flow has not been treated. Since the orifice end of the tube has a configuration like that in Figure 7, initial and reflected waves cannot both be planar and moving axially. Resonance effects will be discussed further in the following section covering the SEPDIS subroutine.

The calculations for drop size and spacing are included in JETPER since this subroutine provides a convenient place for them. These calculations must follow the ORIFIC results and are simply based on mass conservation. The rate of drop production, for all usable printing applications, is the same as the frequency of crystal vibration. Given *this fact and the jet flow rate yields drop volume, mass, and diameter;*

28

METAL INK SUPPLY TUBE

ORIFICE JEWEL

JET DIRECTION
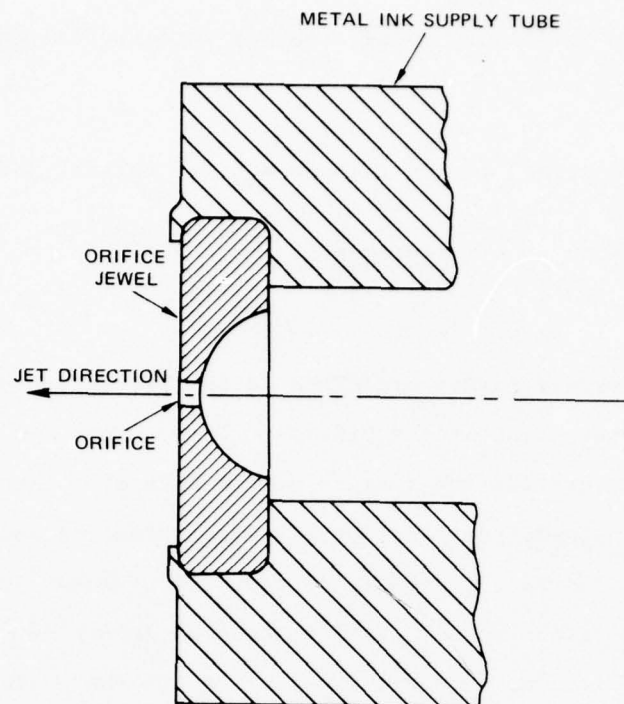
ORIFICE

SA-2055-9

FIGURE 7   ORIFICE MOUNTING DETAIL

Drop Volume $= \dfrac{Q}{f}$, where Q $=$ flow rate, $\dfrac{\text{volume}}{\text{unit time}}$.

f $=$ drop rate, $\dfrac{\text{number}}{\text{unit time}}$.

Drop Mass $= \rho \cdot$ Drop Volume, where $\rho =$ ink density .

Drop Diameter $= \sqrt[3]{\dfrac{6 \cdot \text{Drop Volume}}{\pi}}$.

29

The initial drop spacing is found from jet velocity and drop rate:

$$\text{Drop Spacing} = \frac{v_{jo}}{f}, \text{ where } v_{jo} = \text{ initial jet velocity,}$$

$$\frac{\text{distance}}{\text{unit time}} .$$

The primary result of JETPER is the prediction of the amplitude of velocity perturbation at the orifice. This output did not lend itself to experimental verification because of the lack of a direct way of measurement. Instead, verification of this subroutine and the following one, SEPDIS, had to take place at the same time through the observation of the drop separation point. Verification of drop volume, mass, diameter, and spacing predictions were not required, since these are simple functions of jet velocity and flow rate which are accurately found in the verified ORIFIC subroutine.

When JETPER is completed, control returns to the executive routine, which branches immediately to the next subroutine, SEPDIS.

4.   SEPDIS

As the ink issues in a jet from the orifice, it has a perturbation velocity imposed on its mean velocity. This causes the jet to bunch into nodules that grow to form discrete drops. SEPDIS subroutine predicts the distance from the orifice at which drop separation takes place. The theory used in this prediction of drop separation point is discussed in detail in Appendix B, SEPDIS Theory. As with JETPER subroutine, general considerations and assumptions are presented here.

The distance to break-off depends on the ratio of initial velocity perturbation (computed in JETPER) to mean jet velocity and on

30

two nondimensional parameters, w and T. Parameter w is the reduced frequency of oscillation,

$$w = \frac{2\pi f r}{u} \quad ,$$

and T is the reduced surface tension,

$$T = \frac{T_1}{\rho u^2 r} \quad ,$$

where f(Hertz) is the frequency of oscillation, r(meters) is the jet radius, u (meters/second) is the jet velocity, ρ (kilogram/meter^3) is the ink density, and T_1 (newton/meter) is the ink surface tension. It follows that various trade-offs are possible that maintain the same separation distance. Thus a change in the ink surface tension can be compensated by appropriate flow velocity and oscillation frequency changes.

The theory for the calculation of the separation distance (described in Appendix B) is based on linearized equations of axisymmetric perturbed flow of a cylindrical jet. Once fluid has emerged as a jet, it is assumed to be incompressible and without viscosity. Flow is also assumed to be irrotational. This fundamental method was used by Rayleigh[3] for an unlimited jet but apparently has not been applied before in the case of a jet issuing from an orifice. This is an important difference between Rayleigh's study and the SEPDIS theory. In Rayleigh's work, an infinite fluid cylinder of zero velocity was considered, with an initial spatially periodic perturbation applied the length of the column at one instant. In the case of the ink jet printer, the column is issuing as a jet, with the perturbation imposed over time as the fluid passes a single point (through the orifice).

31

For a perturbation to grow to produce a drop, it must create an unstable condition where the interplay of surface tension and inertial forces leads to jet disintegration. In Rayleigh's work, it was found that such an instability could result only if the disturbance wavelength were equal to or greater than the jet circumference.

$$\lambda \geq 2\pi r \qquad ,$$

where λ is the disturbance wavelength (meters). Since $\lambda = \dfrac{u}{f}$, it is seen that Rayleigh's criterion for drop formation was

$$\frac{2\pi r f}{u} \leq 1 \qquad .$$

The term on the left is the same as w in SEPDIS theory.

The SEPDIS analysis shows that unstable oscillations of the jet radius, for small values of T, were of two kinds. One kind corresponds to $w \leq 1$, as Rayleigh discovered. These oscillations lead to drop formation at the perturbing frequency. If w becomes larger than 1, the SEPDIS theory predicts that a new unstable region can be entered, where drop frequency is several times greater than the impressed frequency. Figure 8 depicts these results. For large enough values of the surface tension parameter T, the jet is predicted to be unstable at all impressed frequencies, with drop rate and perturbation rate likely to differ.

This theory has implications related to satellite formation. If the impressed oscillation contains high enough frequency components, they will be unstable and could produce satellites. This suggests that satellites would be suppressed by reducing the high frequency content of impressed oscillations. The trailing off of the stability boundary in Figure 8 shows that high frequency instability is also suppressed by

32
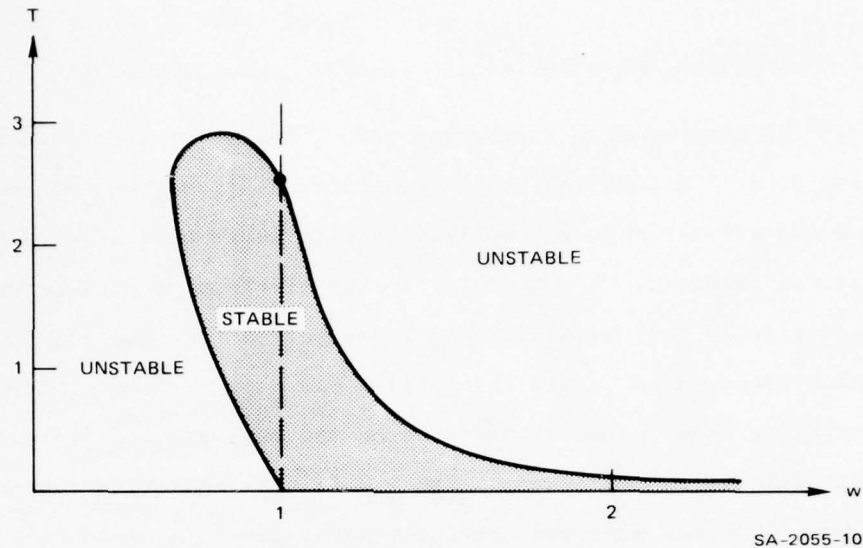
FIGURE 8   STABILITY REGIONS FOR CIRCULAR JET

reducing the surface tension parameter T.   Under typical ink jet printing conditions, the value of T is roughly 0.01 to 0.1.

The prediction of regular jet breakup for $w > 1$ is a new and unexpected result of the SEPDIS analysis, and experimental verification of this part of the theory has not been undertaken.   The fact that the drop production rate is predicted to be different from perturbation frequency in this case makes droplet control difficult and therefore may preclude using the $w > 1$ condition in printing applications.   Thus, SEPDIS subroutine considers cases only where $w \leq 1$.   The case of possible drop production for $w > 1$ has important implications in fluid mechanics. Regular drop formation with $w > 1$ has been observed in a small number of cases.

The most reliable way of verifying the JETPER and SEPDIS subroutines was to compare predictions of drop separation point with observations.   Unfortunately, a test of this kind indicates only if all computing

33

details are correct; no indication is made of where an error has occurred if the theoretical and experimental results do not coincide.

To measure drop separation point, ink was forced through the printing head at a constant pressure. Crystal drive frequency was then set, as was crystal voltage amplitude. With these quantities fixed, the jet was observed. A time delay in the electronics package permitted stroboscopically following a stream perturbation from the orifice to the instant of separation. This observation was done through a microscope on a translating base. A dial indicator on the base allowed distance to the separation point to be measured with 0.001 inch resolution. Such measurements were made for numerous combinations of pressure, frequency, and voltage. At each measuring point, the quality of drop formation and presence or absence of satellites were noted.

Figure 9 shows drop separation as a function of crystal drive voltage, with crystal drive frequency as a parameter. Experimental data and theoretical predictions are shown for four different drive frequencies. One sees from the figure that theory and observation of the distance from the orifice to the point of drop separation show similar trends in that the distance generally decreases as either drive voltage or drive frequency increases. An experimental variation of about ± 0.020 inches in the observations of each point partly explains the quantitative discrepancy at 20 kHz. At the other frequencies, the theory simply fails to explain the observations. A possible reason for this is that the mechanism is sufficiently imperfect in alignment, tightness of fit, and cylindrical symmetry of the parts that the lowest mode resonance is excited at any driving frequency. This fundamental frequency is slightly greater than 20 kHz.

Additional data from the SEPDIS verification work are shown in Figures 10 and 11. Figure 10 shows separation point versus voltage at

34

FIGURE 9   DROP SEPARATION POINT VERSUS CRYSTAL DRIVE VOLTAGE

Data taken with A.B. Dick ink 16-1000; Supply Pressure = 30 psig

35
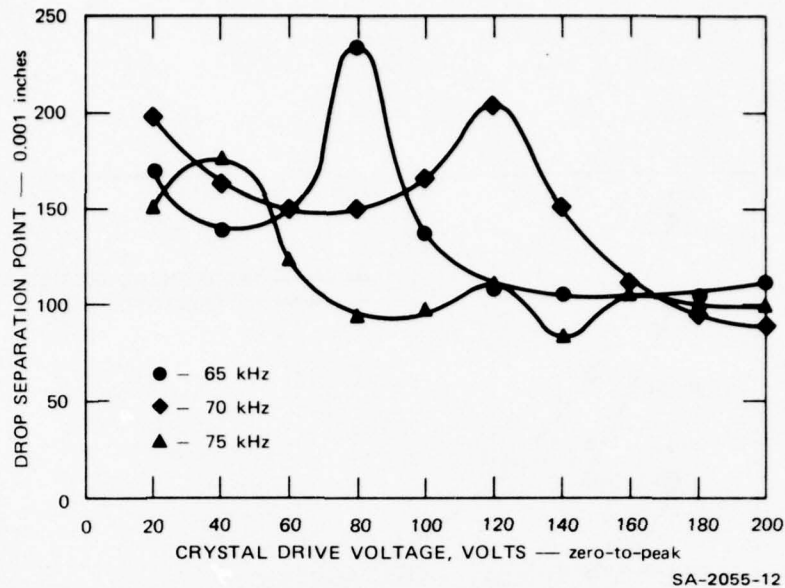
FIGURE 10   DROP SEPARATION POINT VERSUS CRYSTAL DRIVE
VOLTAGE, NEAR RESONANCE
Data taken with A.B. Dick ink 16-1000; Supply Pressure = 30 psig

frequencies near a critical tube resonance ($\approx$ 69 kHz). Here it is seen
that the distance to the separation point can actually increase with an
increase in crystal voltage, which is contrary to expectations when more
energy is delivered to the system. Figure 11 shows distance to separation
point versus crystal drive frequency, with crystal voltage as a parameter.
Here it is also clear that peculiarities exist near the tube resonance.
Additional data from the study of jet breakup are included in the Data
Package.

Regarding resonance, the metal tube carrying ink to the orifice
acts like an organ pipe open at one end and (nearly) closed at the other.
In such a case, the fundamental pipe frequency is:

$$f_1 = \frac{c}{4L} \quad , \qquad \text{where } c = \text{sonic velocity}$$
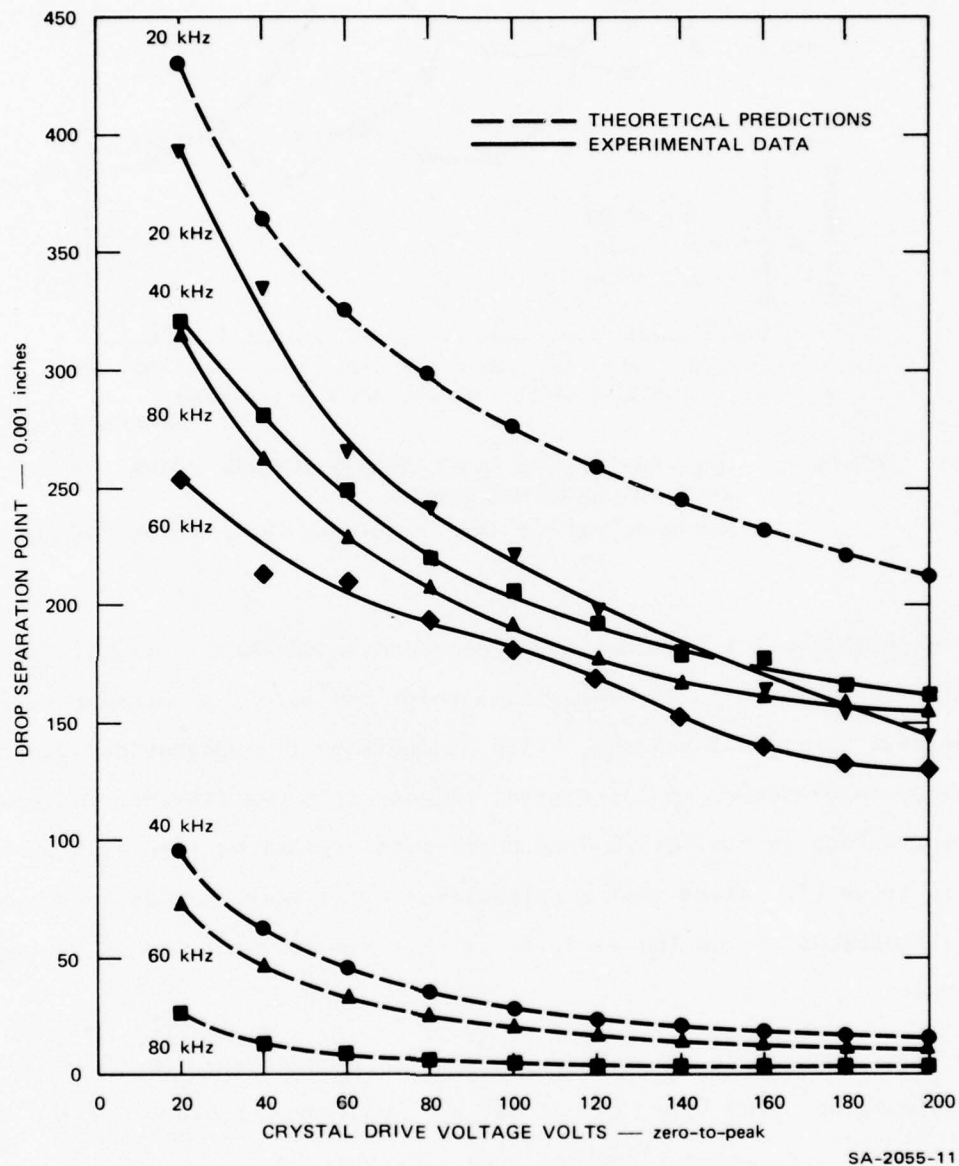$$L = \text{pipe length.}$$

36
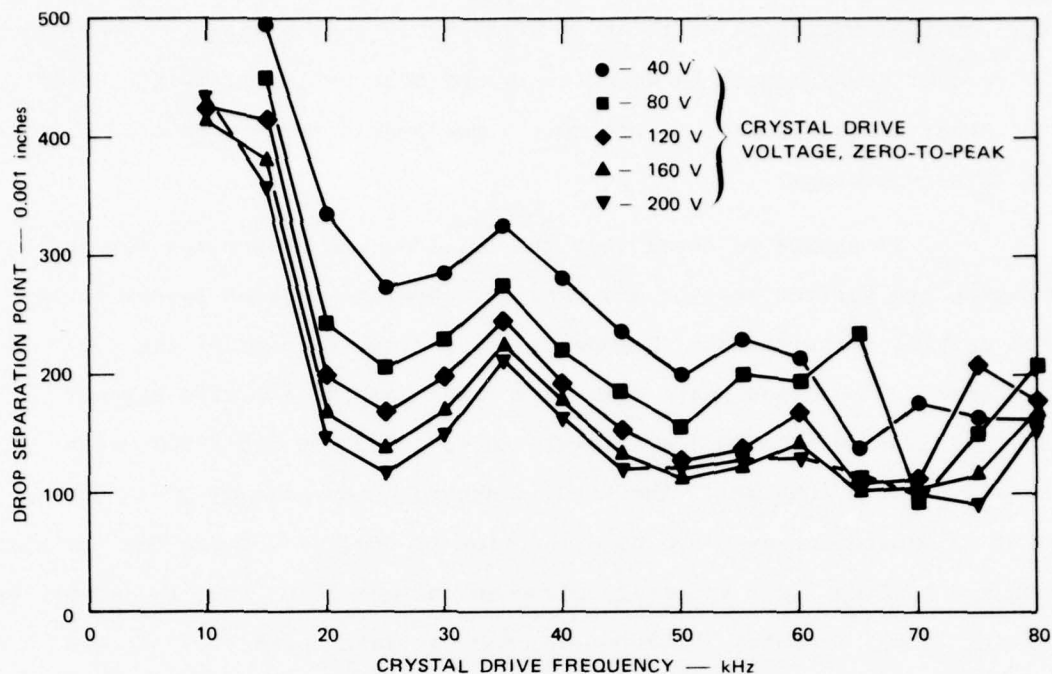
FIGURE 11   DROP SEPARATION POINT VERSUS CRYSTAL DRIVE FREQUENCY
Data taken with A.B. Dick ink 16-1000; Supply Pressure = 30 psig

Odd harmonics of this frequency are also important. In the ink jet printer, $f_1 \approx 23$ kHz, which is too low for most applications. The next important harmonic is near 69 kHz. At these frequencies, resonance effects will generally act to impart more perturbing energy to the issuing jet. Figure 11 shows a decrease in separation distance near these frequencies.

In summary, the large discrepancies between theory and experimentation at frequencies above 20 kHz are likely to result from the presence of more than the single frequency of the driver. As seen in Figure 10, the fundamental tube frequency seems to be excited for all driving frequencies. The observed shape of the jet before breakup shows swellings and ligaments that are far from sinusoidal. Near breakup, non-linear behavior is necessarily important, while the perturbation flow

37

through the orifice is still an uncertainty in the analysis. The 20 to 25 percent disagreement between theory and observation at 20 kHz, with the observed values low, is probably a reasonable reflection of the state of this technology.

It should be noted that the critical ink properties for jet breakup are surface tension and density. Surface tension forces cause the initial perturbations to grow; as they grow, inertia of the field is overcome. Separation point data were taken for the ink with highest surface tension (16-6000) and lowest surface tension (16-1000), with density nearly constant. The results showed a decrease of 20 to 40 percent in separation distance as a function of crystal voltage for the high surface tension ink. Viscosity plays an insignificant role in jet break-up and is not included in the model, for the same reason that it was neglected in the JETPER theory. Also, Rayleigh has stated that the ability to regularly break the jet into uniform drops is evidence of the unimportance of viscosity.

In the ink jet printer, the charging electrode covers a distance of 0.110 to 0.360 inches from the orifice. For proper charging of the drops, separation must take place within about the first two-thirds of the electrode, as explained in Section III-D-5. Thus, SEPDIS subroutine tests the separation point prediction. If it lies within this region, it is accepted; if not, separation point is set at the midpoint of the charging electrode. This is justified, since the separation point must lie near electrode center in any printing configuration.

The printing head displays numerous jet profiles and drop separation characteristics, depending on ink pressure, crystal voltage, and frequency. Some of the possibilities are shown in the series of photographs of Figure 12, which illustrates acceptable drop separation, as well as fast and slow satellites and irregular jet profiles. This
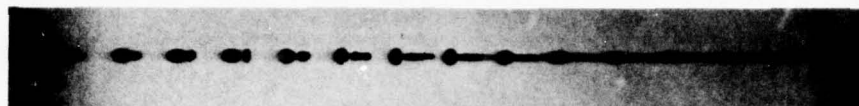
(a) P_g = 40 psi; V = 150 v, z – p; f = 35 kHz; v_{jO} = 785 ips; λ = 22.4 mils; λ/d_{jO} = 8.9.
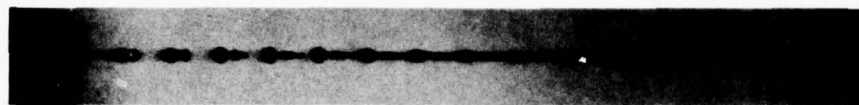
(b) P_g = 40 psi; V = 80 v, z – p; f = 40 kHz; v_{jO} = 785 ips; λ = 19.6 mils; λ/d_{jO} = 7.8.
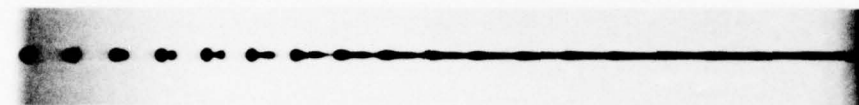
(c) P_g = 40 psi; V = 160 v, z – p; f = 45 kHz; v_{jO} = 785 ips; λ = 17.4 mils; λ/d_{jO} = 6.9.
Note mini-satellite.

(d) P_g = 40 psi; V = 200 v, z – p; f = 50 kHz; v_{jO} = 785 ips; λ = 15.7 mils; λ/d_{jO} = 6.2.
Excessive satellites.

(e) P_g = 40 psi; V = 65 v, z – p; f = 60 kHz; v_{jO} = 785 ips; λ = 13.1 mils; λ/d_{jO} = 5.2.
No satellites.

(f) P_g = 40 psi; V = 80 v, z – p; f = 60 kHz; v_{jO} = 785 ips; λ = 13.1 mils; λ/d_{jO} = 5.2.
One mini-satellite present.

(g) P_g = 40 psi; V = 65 v, z – p; f = 65 kHz; v_{jO} = 785 ips; λ = 12.1 mils; λ/d_{jO} = 4.8.
Fast satellites.

SA-2055-42A

FIGURE 12   PHOTOGRAPHS OF DROP FORMATION

39
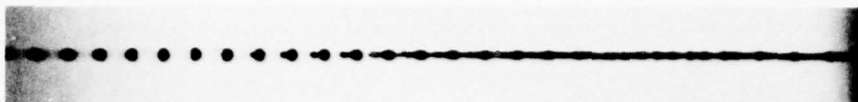
(h) P_g = 40 psi; V = 100 v, z – p; f = 65 kHz; v_{jO} = 785 ips; λ = 12.1 mils; λ/d_{jO} = 4.8. No satellites.
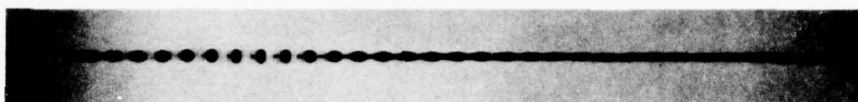
(i) P_g = 40 psi; V = 120 v, z – p; f = 80 kHz; v_{jO} = 785 ips; λ = 9.8 mils; λ/d_{jO} = 3.9. Slow satellites.
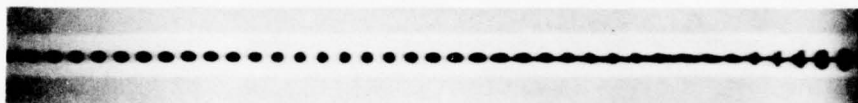
(j) P_g = 40 psi; V = 35 v, z – p; f = 111 kHz; v_{jO} = 785 ips; λ = 7.1 mils; λ/d_{jO} = 2.8. Break-up beyond Rayleigh's regime.

(k) P_g = 30 psi; V ≈ 80 v, z – p; f = 50 kHz; v_{jO} = 660 ips; λ = 13.2 mils; λ/d_{jO} = 5.2. One mini-satellite present.

(l) P_g = 20 psi; V = 100 v, z – p; f = 60 kHz; v_{jO} = 520 ips; λ = 8.7 mils; λ/d_{jO} = 3.5. Two slow satellites.
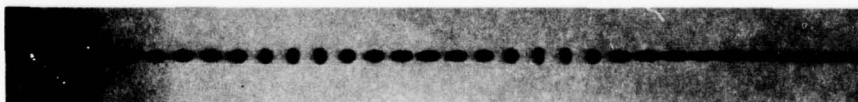
(m) P_g = 20 psi; V = 140 v, z – p; f = 54.5 kHz; v_{jO} = 520 ips; λ = 9.5 mils; λ/d_{jO} = 3.8.
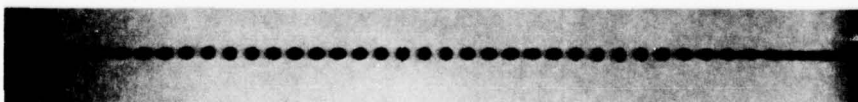
(n) P_g = 20 psi; V = 65 v, z – p; f = 69 kHz; v_{jO} = 520 ips; λ = 7.5 mils; λ/d_{jO} = 3.0. Slow satellites.

SA-2055-42B

FIGURE 12   PHOTOGRAPHS OF DROP FORMATION (Continued)
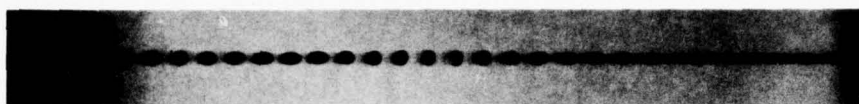
(o) P_g = 30 psi; V = 65 v, z – p; f = 69 kHz; v_{j0} = 660 ips; λ = 9.6 mils; λ/d_{j0} = 3.8.
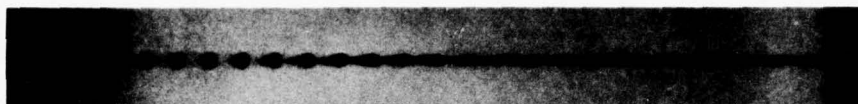
(p) P_g = 40 psi; V = 65 v, z – p; f = 69 kHz; v_{j0} = 785 ips; λ = 11.4 mils; λ/d_{j0} = 4.5.
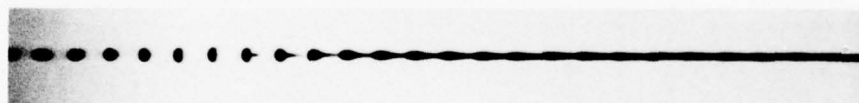
SA-2055-42C

FIGURE 12   PHOTOGRAPHS OF DROP FORMATION (Concluded)

illustrates a critical aspect of ink jet printing. Namely, the operating
point must be chosen where jet breakup is acceptable.

An attempt was made to define "acceptable" drop formation.
First, the separation point had to lie within the charging electrode.
Second, no more than five satellites were allowed at any instant, although
either fast or slow satellites were permitted. Observations of drop forma-
tion quality were made during data taking. Conditions of "acceptable"
performance were then mapped out, as in Figure 13. Additional maps are
found in the Data Package.

The primary cause of unacceptable drop formation was the pres-
ence of satellites. Under most conditions, the jet perturbations would
grow into primary nodules connected by thin ligaments, as seen earlier in
Figure 12. The ligament would frequently separate at both ends and then
move to combine with either the leading or trailing drop. Occasionally,
the satellite would remain between the main drops for a large distance.
The formation of fast and slow satellites is shown in Figure 14. The
relative velocity of the satellite is traced to the end of the ligament
that first separates, and it is caused by a momentary imbalance of sur-
face tension forces. As drive frequency increased, the satellites became

41
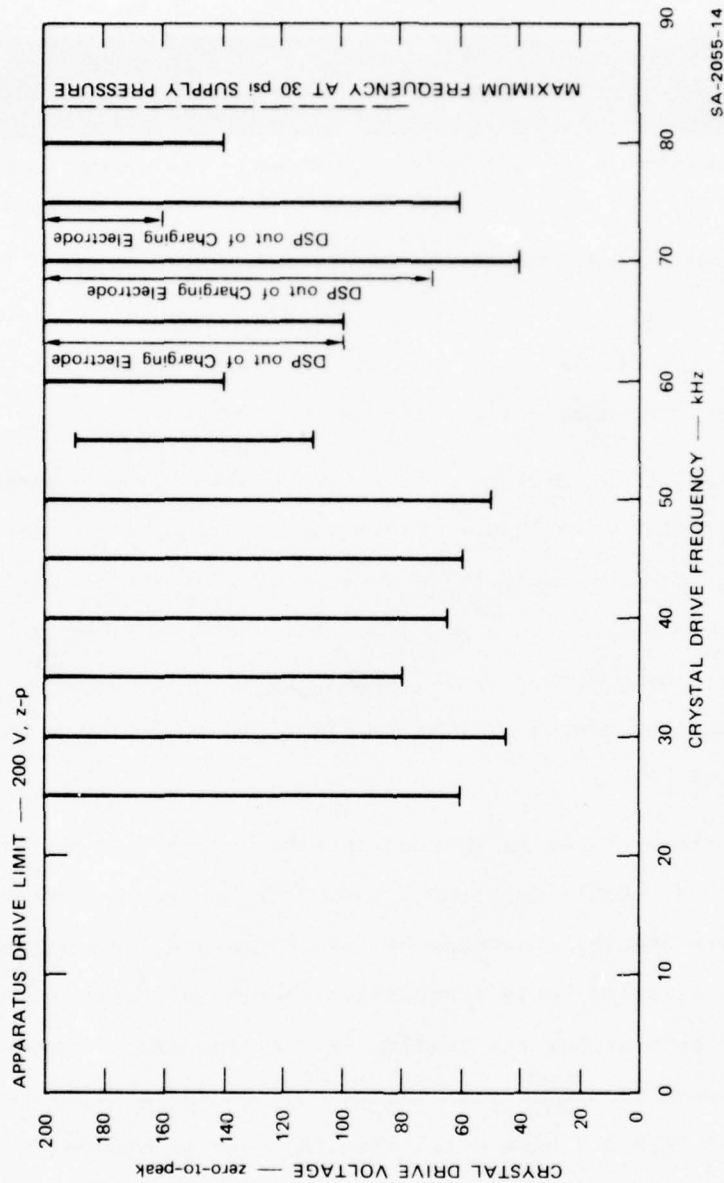
FIGURE 13   CONDITIONS FOR ACCEPTABLE DROP FORMATION

Data taken with A.B. Dick ink 16-1000; Supply
Pressure = 30 psig.

42

JET DIRECTION

(a) MAIN DROP WITH LIGAMENT JUST BEFORE SEPARATION

JET DIRECTION

RELATIVE SATELLITE VELOCITY

(b) FAST SATELLITE CONDITION, DUE TO INITIAL SEPARATION AT
    POINT X

JET DIRECTION

RELATIVE SATELLITE VELOCITY

(c) SLOW SATELLITE CONDITION, DUE TO INITIAL SEPARATION AT
    POINT Y
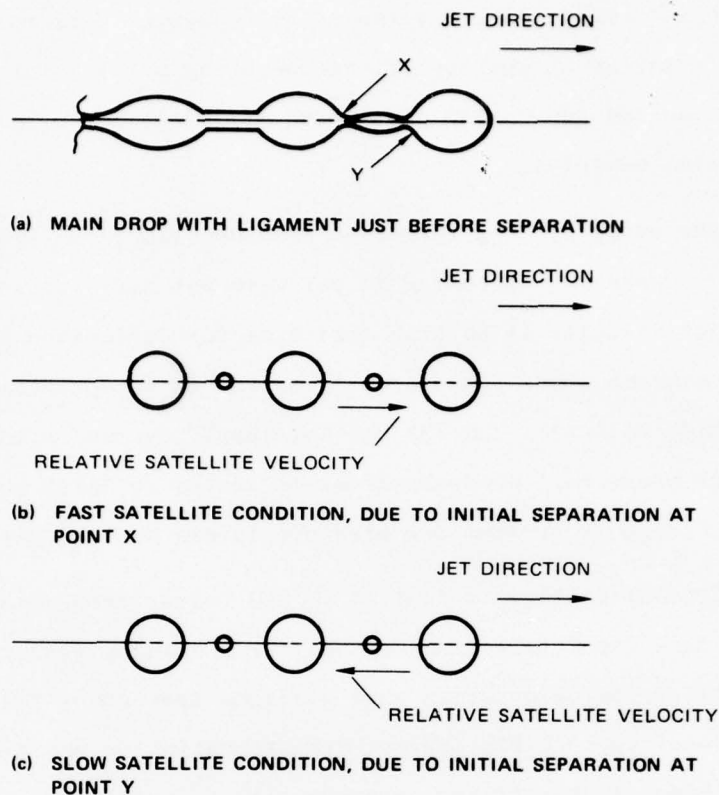
SA-2055-15

FIGURE 14   FAST AND SLOW SATELLITES

smaller, until they were estimated to be 1/10 to 1/20 of the drop diameter. Furthermore, at higher frequencies, it was found that slight changes in drive voltage could shift satellites from fast to slow or vice versa, and could render formation unacceptable. Satellites had to be either fast or slow and quickly join the main drops so that they would not be forced apart in the deflecting field.

The presence of satellites has implications in ink jet printing, since they are undesirable. An attempt to define the conditions for satellite presence was fruitless, so this could not be included in the program. Thus, SEPDIS subroutine will predict a drop separation point

43

for any imposed conditions, but the printing system user must experimentally verify the acceptability of the operating point. Variations in drop formation and separation point with different printing head assemblies are also expected.

The study of drop formation provided limits on several operating parameters. Pressures exceeding 80 psi were not used, because (1) at high pressure, jet velocity is so high that time for deflection is limited; (2) the conditions under which drop formation is acceptable are less common at high velocity; and (3) the ink supply system is more likely to fail at high pressure. Pressure level is tested in DATIN subroutine, and a warning message is printed for pressure levels over 80 psi.

Crystal voltage is limited to 200 volts, zero-to-peak. DATIN also tests this input value and can deliver a warning message. This limit is set by the observation that voltages from about 150 to 200 volts usually did not appreciably improve drop formation or shorten separation distance. Also, high voltages were more likely to produce an irregular jet profile and satellite formation was more sensitive to small voltage changes. Furthermore, the amplifiers used in experimental work had difficulty providing high voltage, high frequency output.

Drive frequency is limited by the requirement that

$$w \leq 1 \quad .$$

Therefore, SEPDIS subroutine tests w and terminates the program if the combination of frequency and jet velocity is too large. Figure 15 shows the approximate frequency limit as a function of supply pressure. Some experimental maximum points are plotted, showing that operation at $w > 1$ has been observed.

44
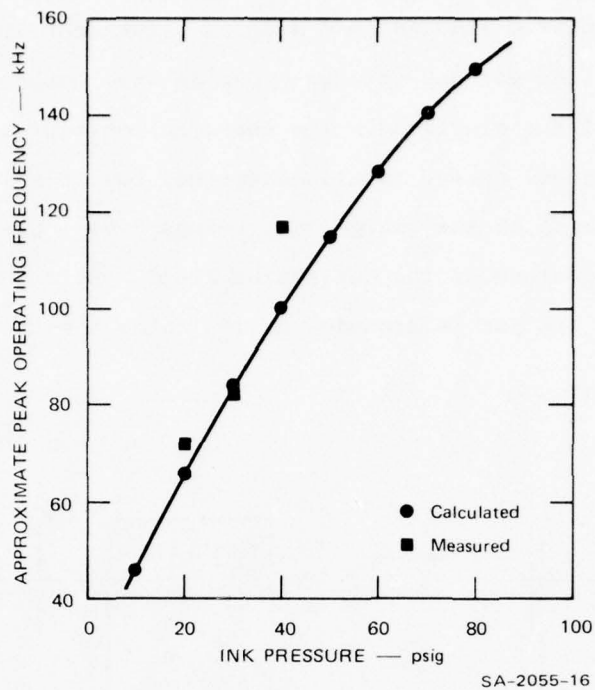
FIGURE 15   PEAK OPERATING FREQUENCY
VERSUS SUPPLY PRESSURE

When SEPDIS subroutine is completed, control is returned to the executive routine. The executive print control is checked and an output of drop characteristics can occur. Control then transfers to CHARGE subroutine.

5.   CHARGE

In the ink jet printer, the area near the drop separation point is surrounded by a charging electrode. When a voltage signal is delivered to the electrode, it causes a charge of opposite polarity to be induced on the conductive jet. When the drop separates from the jet, it carries the induced charge with it. Coupling to the drop being formed is capacitive. Subroutine CHARGE is used to compute the quantity of charge that will be deposited on each drop to be created in the computer run.

45

The charge induced on a drop is affected primarily by the charging electrode gap and voltage. Gap is the spacing between the vertical leaves of the electrode. The charging configuration is shown in Figure 16. Induced charge is also affected, but to a lesser degree, by other factors such as the charge on previous drops, pressure of the fluid stream, and magnitude of the deflection field. Note that the continuous portion of the ink jet is grounded by its contact with the metal ink supply tube.
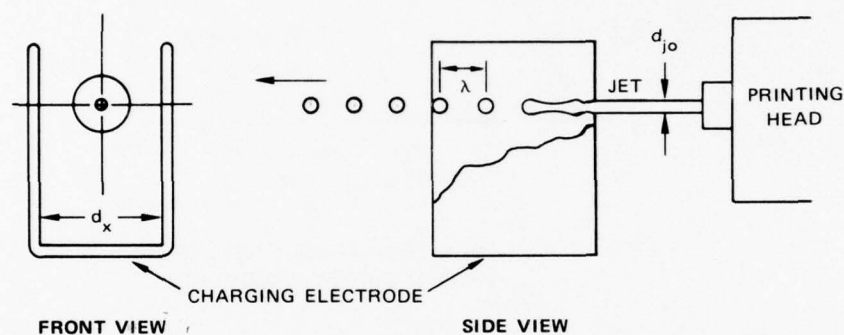
SA-2055-35

FIGURE 16   CHARGING STATION

To determine the effects of the relevant parameters, two methods were considered for developing an analytical model for drop charging. In the first method, the numerical solution to Laplace's equation in the volume of interest would be obtained by relaxation algorithms. Since the geometry of the charging configuration is relatively complex and the computing algorithms iterative, the amount of computer core memory and the time required for a solution suggested that this was not an acceptable method for calculating the induced charge.

The second method, which was used in formulating the subroutine, consisted of correcting an approximate closed form analytical solution to Laplace's equation. The correction to the approximate model was obtained

46

by fitting curves to experimental data. The approximate model chosen
was one used by Sweet[4].

Sweet's method for calculating the induced charge was to assume
a charging capacitance and multiply this by the charging voltage. The
charging capacitance was modeled after a cylindrical conductor of diam-
eter d_{jo} centered between two infinite conducting planes with spacing d_x;
the planes are at the same potential. The capacitance per-unit length
was multiplied by one wavelength of jet disturbance, λ, to obtain the
capacitance that contributes to the charge on one drop. The model thus
assumes that a uniform distributed charge is on the cylindrical conductor.

This model is an approximation since the actual electrode is
finite in size and the center electrode (the jet) is not a smooth cylinder.
These two deviations from the model are not severe enough to necessitate
a modification of the model. The significant deficiency of the model is
that it does not allow for a nonuniform charge distribution. If the
charging voltage is the same for each drop (i.e., steady-state operation),
then the effective charge per-unit length will be the same as in Sweet's
model. If, however, the charging voltage changes from drop to drop, then
the captive charge will vary. When this condition occurs, there is no
longer a uniform charge distribution along the center electrode and Sweet's
model fails.

With a nonuniform charge distribution, the effect of capacitance
between a newly formed drop and the next one to separate can be observed.
If a single drop is given a charge, and the charging voltage for the fol-
lowing drop is zero, the following drop will be found to carry a smaller
charge of opposite sign to that of the first drop.

Sweet's model was modified by obtaining experimental data and
by deriving solutions to Laplace's equation for other electrode configura-
tions. Specifically, the configurations that were considered were two

47

equal-sized conducting spheres in free space and one conducting sphere between two infinite conducting planes. The relevant capacitances for these two configurations were applied to Sweet's model, and then an empirical correction factor was generated to fit the resulting model to the experimental data.

The analytical model for the charge induced on the i-th drop, q_i, is of the form

$$q_i = -CV_i - F_1 (q_{i-1} + CV_i) - F_2 (q_{i-2} + CV_i) \quad ,$$

where

C is the primary electrode-to-jet capacitance derived from Sweet's model,

q_{i-1} is the charge on the (i-1)th drop,

q_{i-2} is the charge on the (i-2)th drop,

V_i is the charging voltage for the ith drop, and

F_1 and F_2 are ratios of capacitances of the drops and electrodes.

The derivation of this equation and the capacitance models is described in Appendix C, CHARGE Theory. Basically this model indicates that the charge induced on the ith drop is the product of C and V_i. This product is the steady-state charge; when the system is in a transient state, then the steady-state charge must be compensated according to the charges on the two preceding drops, q_{i-1} and q_{1-2}. This compensation is in the form of the difference between the steady-state charge and the two previous charges, since the q's will be negative for positive charging voltage. F_1 and F_2 scale the difference to the proper magnitude, as determined by such factors as drop rate (f, drops/second), electrode gap (d_x), and jet diameter (d_{jo}).

48

The experimental conditions under which the model has been verified are:

- Frequency, f, was varied from 26.8 to 51.8 kHz.

- Charging electrode spacing, d_x, was varied from 40 to 100 mils.

- Charging voltage, V_i, was varied from 0 to 400 volts.

- Gage pressure of the ink was kept constant at 30 psig.

- Deflection plate angle was varied from 0 to 20 degrees.

- Deflection plate voltage was varied from 0 to -4 kV.

The verification procedure compared the measured induced charge on individual drops with the charge as calculated by the model. The steady-state charges were also compared. Charge was determined experimentally by measuring the current caused by the moving charges and then dividing by the frequency at which the drops are charged. For steady-state operation, this frequency is f, the rate at which drops are formed, since all drops are charged. If only one of every 24 drops were charged, the drop charging frequency was $f/24$.

The effect that each of the six parameters had on drop charging and their limitations is discussed below.

Frequency--The charge induced per drop is roughly proportional to the inverse of f, primarily because the charging capacitance, C, is directly proportional to λ, the length of the jet stream that forms one drop, and $\lambda = v_{jo}/f$. The frequencies used in the experiments were limited to those at which stable drops could be formed. If satellites formed at a particular frequency, that frequency would be used only if the satellites reformed with the main drops in less than four drop spacings. Also, the satellite had to be connected to the main drop at break-off. Drop formation was not too reliable at frequencies below about 26 kHz. At frequencies above about 52 kHz, drop formation was more susceptible to small variations in operating conditions. The frequency range from 26 to 52 kHz was thus chosen for testing the model.

49

Frequency has an important role in determining the effect of previous drops on a drop being charged. Since $\lambda = v_{jo}/f$, frequency determined the distance between drops and thus the inductive capacitance between drops. It was determined experimentally that the capacitance between nonadjacent drops could be neglected if there were more than one drop between them. Thus, only the two previously charged drops have a significant influence on a drop being charged.

At the lower frequencies, a drop at break-off was not immediately spherical but rather elongated and cylindrical, as seen in Figure 12. Since the inductive capacitance was modeled on spheres spaced λ apart, a correction factor was introduced to model the effective separation as a function of frequency.

Charging Electrode Spacing--Charging capacitance C is inversely proportional to the logarithm of electrode spacing. Thus, induced charge is roughly related in the same manner. At close spacing the field strength was high enough to cause satellites to form with only moderately high charging voltages. This effect was accentuated at low frequencies, since drop diameter and λ increase with decreasing frequency. Figure 17 shows maximum allowable charging voltage as a function of electrode spacing. If drop formation is marginal, a high charging voltage can seriously disrupt jet breakup. The charging electrode also serves the important function of shielding the jet from stray fields, such as the deflecting field. Generally, the smaller the d_x, the more complete is the shielding effect.

Charging Voltage--Induced charge is linearly related to charging voltage. As previously noted, an excessive charging voltage could cause satellites to form. For single drop charging, the maximum pulsed charging voltage available was +400 volts; therefore, the model has been verified only to that value.
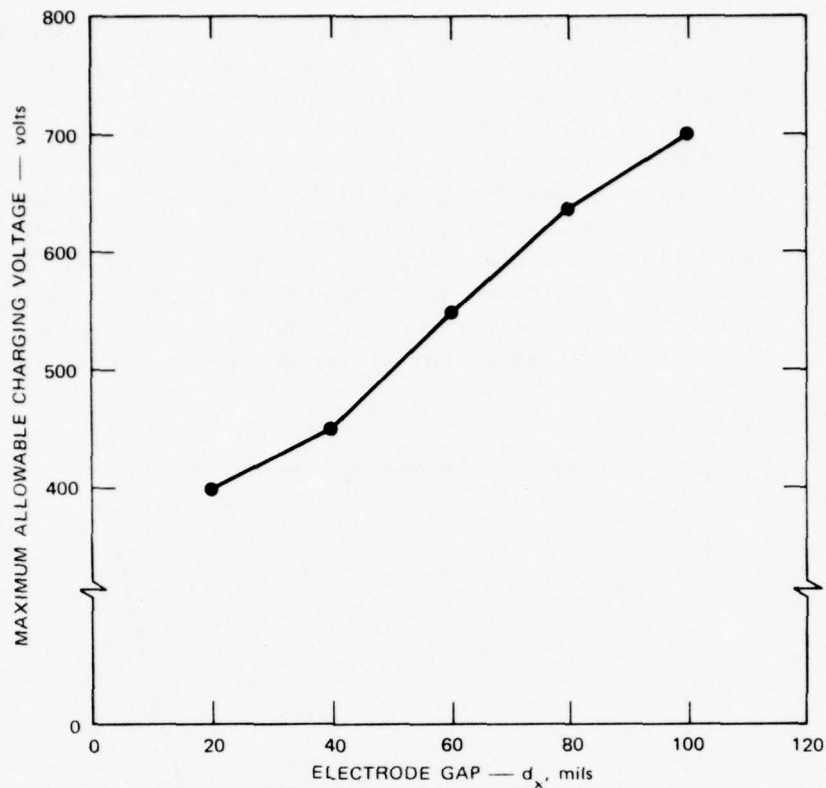
FIGURE 17   MAXIMUM CHARGING VOLTAGE AS A FUNCTION OF
ELECTRODE GAP

Ink Supply Pressure--Ink supply pressure was kept at 30
psig throughout the verification procedure. Varying it
would mean that an increase in pressure would result in
an increase in jet velocity, and vice versa. Since λ
is directly proportional to velocity for a constant
frequency, the induced charge would increase. The
experimental variation in λ was realized by varying
frequency rather than by adjusting pressure.

Deflection Plate Angle--The value of the deflection
plate angle had a negligible effect on the amount of
charge induced, primarily because the movable plate
was at ground potential. Thus it was not necessary to
include plate angle as a parameter in the model.

51

Deflection Plate Voltage--The effect of the deflection
plate voltage was to reduce induced charge, because its
polarity was opposite to that of the charging potential.
Since it is a dc voltage, it induces an equal charge on
all drops. This effect may be compensated simply by
changing the baseline level of the charging voltage to
a slightly positive value to offset the fringe field of
the deflection plates. Figure 18 is a plot of the ratio
of compensating charging voltage to deflecting voltage
as a function of electrode gap. At low values of d_x, the
effect is negligible, but at large spacing, the deflecting

SA-2055-36
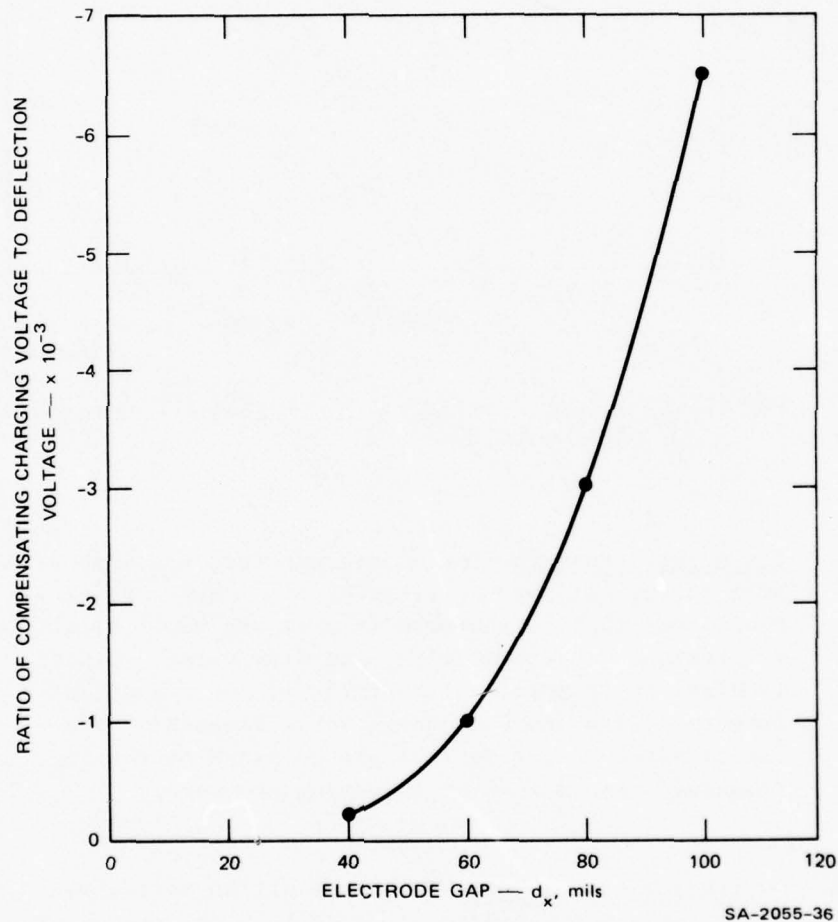
FIGURE 18   CHARGING VOLTAGE COMPENSATION FOR DEFLECTING
FIELD EFFECTS

52

field effect is significant. This effect is also frequency dependent. Figure 18 shows the worst cases encountered, generally at low frequencies.

Since the effect of deflecting field is easily compensated by an adjustment of the charging signal baseline, the model does not include a correction factor.

The results of the analytical and experimental work related to drop charging, which yielded the equations at the beginning of this section and in Appendix C, are discussed in the following paragraphs.

No errors greater than 10 percent were encountered when comparing the predicted drop charge with the measured charge for the parameters in the range of verification. In general, the errors were in the range of 2 to 5 percent.

The largest errors tended to be at low frequencies and with small electrode spacing. Under these conditions, the initial drop shape departs significantly from a sphere and the inductive capacitance between two drops is difficult to model.

For parameter values beyond the range of verification, the model should be reasonably accurate for many cases. In particular, electrode gap can be allowed to take on values from 20 to 140 mils with usable results (errors less than 20 percent). For frequency between 52 and 80 kHz, the model will be useful but will slightly overpredict the charge. Charging voltage may be increased with no additional errors unless satellites are formed.

It is essential that drop formation be stable; few, if any, satellites are allowed for the model to be accurate. It was found that poor drop formation was the cause of most of the problems in collecting and interpreting data.

53

The effect of the preceding drops on a drop being charged was significant in determining the charge for transient operation. This effect was the most difficult to model because of the lack of exact solutions to Laplace's equation and the difficulty of accurately measuring the charge on single drops.

The difficulty in measuring the charge on a single drop, when only one of a group of 24 is charged, is that the other drops must be totally uncharged or else their small charge when multiplied by 23 becomes a significant part of the measured current. The best procedure found was to observe the drop stream with no charging or deflection voltages, note its position, and then apply the desired deflection voltage. The resulting offset was then compensated by adjusting the baseline of the charging voltage to give the original drop stream position. At this point, zero stream current should result. Next, the desired charging voltage should be applied to the appropriate drop and the charging voltage baseline re-checked for its correct value. (Since the baseline is not electronically independent of a charging voltage pulse it is necessary to reset it.) The actual charging voltage is the difference between the charging voltage relative to ground and the baseline voltage. At this point, a few drops following the single charged drop will be deflected downward because of a drop-induced charge of opposite polarity. This is nullified by applying to these drops a charging voltage sufficient to bring them back to the original stream position. The current created by a single charged drop in each group of 24 can then be measured and its charge calculated.

From the experimental work, three recommendations can be made regarding drop charging.

- The electrode gap should be as small as is conveniently set. This reduces the relative influence of the two previous drops and provides the best shielding from other fields.

- Drop separation should take place at the midpoint of travel through the electrode, since the charging field is most uniform there.

- A high charging voltage will reduce the influence of stray fields and the charges on previous drops.

One test is included in subroutine CHARGE. When a signal is applied to the charging electrode, an induced charge appears on the drop being formed. The time required for this is a function of electrode-to-jet capacitance and jet resistance. The resistance of the jet depends on its dimensions and ink resistivity. The charging time should be a small fraction of the time for a drop to form $(1/f)$ to ensure that full charge is developed. Charging time is computed in CHARGE using Sweet's method.[4] If this time is greater than $0.2/f$, a warning message is printed, indicating that ink resistivity is too high. Since all the A. B. Dick inks have low resistivity, it is doubtful that this problem will ever arise.

After CHARGE subroutine is completed, control returns to the executive routine. This concludes the drop formation section of the computer model, which has determined drop characteristics and initial velocity. The remainder of the program deals with drop ballistics. It should be noted that ink properties play a role only in the drop formation section. Once the drops are formed and charged, their ballistic behavior is independent of all ink properties except density, which determines drop mass.

The executive routine performs several functions before calling the next subroutine. First, it computes a time interval for incrementing the drops toward the printing surface. This is initially set at $1/f$. Then, a counter, NPTS, is set to zero.

At this point, the loop for following the ballistic behavior of the drops is entered. A test within the loop determines if all the

55

desired drops have been created. If they have not, the drop counter NPTS is incremented by 1 and CREATE subroutine is called, which creates one more drop. From there, the deflecting, repulsive, and aerodynamic forces on all existing drops are computed. Each time through the drop ballistics loop, an additional drop is created, until MAXPTS drops exist.

Once the desired number of drops has been created (NPTS = MAXPTS), CREATE subroutine is no longer called. A test is performed to see if any drops are near the printing surface. If not, a longer time increment $(5/f)$ is used for incrementing the drops. If any drops are near the surface, the time increment is again set to $1/f$. After the time interval check, the subroutines to compute forces on the drops are again used.

After the forces on the drops have been found, the corresponding accelerations are determined. Then, the velocity and position are incremented. In this way, the drop ballistics loop steps the drops through space to the printing surface. This process can be seen in the flowchart, Figure 2, and is further discussed in the following sections.

6. CREATE

As shown in the flowchart, Figure 2, CREATE subroutine is used to create an ink drop and initialize its state vector. CREATE is used to form one drop each time through the drop ballistics loop, until MAXPTS number of drops has been formed. When this point is reached, CREATE is not called on again, and the existing drops continue to be incremented through space to the imaginary printing surface. The value of MAXPTS is set via a user-made punched card in the executive routine.

Properties of all existing drops are contained in a state vector. The state vector is an array in the form STATE (I, J), where I is an integer between 1 and NPTS and J is an integer between 1 and 11.

56

I refers to the number of a drop; J refers to various properties of the I-th drop. For example, STATE (I, 1) is the x-coordinate of the drop. Similarly,

J = 2 refers to the y-coordinate of the drop

J = 3 refers to the z-coordinate of the drop

J = 4 refers to the x-component of velocity of the drop

J = 5 refers to the y-component of velocity of the drop

J = 6 refers to the z-component of velocity of the drop

J = 7 refers to the x-component of acceleration of the drop

J = 8 refers to the y-component of acceleration of the drop

J = 9 refers to the z-component of acceleration of the drop

J = 10 refers to the electrical charge of the drop

J = 11 refers to the elapsed time in flight from the orifice to the present drop position.

The coordinate directions used in the drop ballistics section of the program are shown in Figure 19 in which x is the direction of the jet as it leaves the printing head; y is the vertical direction, perpendicular to the lower deflection plate; and z is the direction mutually perpendicular to x and y according to the right-hand rule. During CREATE, all the position, velocity, and acceleration components are set to zero except for the x-coordinate of position and the x-component of velocity. The x-position is taken as the drop separation distance plus
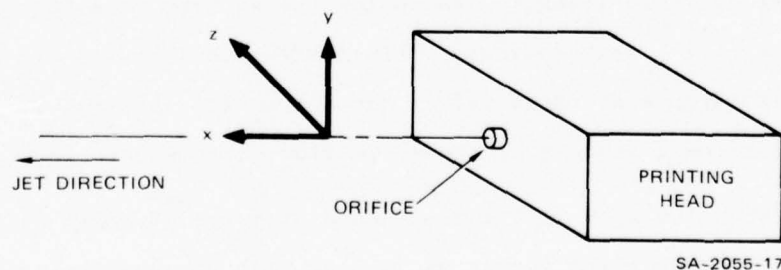
SA-2055-17

FIGURE 19   COORDINATE SYSTEM FOR COMPUTER MODEL

57

the drop radius. The x-velocity is set to the initial jet velocity. The charge on each drop is established earlier in CHARGE subroutine. Initial elapsed time equals position divided by velocity. No verification of CREATE subroutine is needed.

After CREATE has formed the desired drop and assigned initial values to its state vector, control is returned to the executive routine. If MAXPTS number of drops has not been formed, control branches to ELECT subroutine, with the time interval for drop stepping set at the reciprocal of drop rate. If all the drops have been formed, the incrementing time interval is increased to five times the earlier rate. Once any drop has traveled 95 percent of the way to the printing surface, the time increment for drop stepping is reduced back to 1/f. After checking and adjusting the stepping interval, control branches to ELECT subroutine.

7.   ELECT

As the drops leave the charging electrode with their trapped charge, they enter an electrostatic field which tends to deflect them from a free trajectory. ELECT subroutine, together with the function PHI (described next), computes the force on each ink drop caused by the electric field that the deflection plates produce. Function PHI provides ELECT with the value of electric potential at the coordinate position of the I-th drop and at adjacent locations. Field strength is then computed as the space derivative of the potential. For example, to obtain the y-component of field strength, the potential at drop location (x,y,z) and at location $(x, y + \delta, z)$ is found. Field strength in the y-direction is then the difference of these values divided by the interval δ. In ELECT, δ is taken to be 2 percent of the deflection plate separation.

When the x, y, and z components of field strength have been found, the corresponding forces on the ink drop in question are calculated from the simple relation,

58

$$F_x = qE_x \text{ , where } F_x = \text{force on ink drop in x direction}$$

$$q = \text{charge on the drop}$$

$$E_x = \text{field strength in x-direction.}$$

The electrostatic forces on every existing drop in the x, y, and z directions are stored in the array STATIC for later use.

As shown in the flow chart, Figure 2, ELECT is the first of three subroutines in the drop ballistics loop that are used to compute the vector components of forces on the drops.

ELECT subroutine is quite simple, relying only on basic physics. It requires no verification by itself, but rather is considered along with the more complex function PHI. Each time ELECT is called, the function PHI is called from ELECT four times.

8.   PHI

The function PHI provides ELECT with the electrostatic potential at points within the deflecting field. The deflecting field is generated by the two deflecting plates, the top plate being grounded and the bottom plate held at a negative potential. The included angle between the plates can vary from 0° to 25°. The field extends beyond the ends of the plates because of fringing effects.

The calculations used in PHI are based on several assumptions:

• The deflecting plates are assumed to have infinite lateral length (in the z-direction in Figure 19). This assumption reduces the problem from three to two dimensions, and is valid as long as the stream passes through the lateral center of the field and if plate separation is small compared with the plate width. Naturally, this approximation is less accurate near the exit of the deflecting field when plate angle is large, since plate separation can be quite large there.

59

- The plates have zero thickness and the ends of the
  plates are vertically in line where the jet enters.
  Neither of these assumptions is completely true, since
  the plates have finite thickness with rounded edges
  and since the upper plate pivots about a point not at
  its end. The physical arrangement can be seen in
  Figure 1.

- The plates are perfect conductors, which for practical
  purposes is true.

- The effect on the field due to the presence of traveling
  charged drops was neglected.

- The presence of the charging electrode was neglected.

These assumptions were needed to make the analytical problem manageable.
Given these assumptions, a complex variable theory to determine the
potential between and near the deflecting plates was justified.

During the project, the complex variable problem was solved
under progressively more difficult conditions. To get a feeling for the
problem, the field within an infinite parallel plate capacitor was studied
first. Next, the semi-infinite parallel plate case was examined, per-
mitting a field strength investigation within and near the end of the two
plates. (In the context of this discussion, "infinite" means extending
from $+\infty$ to $-\infty$ along the jet direction, and "semi-infinite" means ex-
tending to $+\infty$ only. The plates are always assumed to have infinite
lateral length, as mentioned above.) Finally, the finite parallel-plate
capacitor problem was solved using solutions given in a standard reference
book.[5]

Having investigated the parallel-plate field theory, a non-
parallel plate configuration was examined. Again, a semi-infinite non-
parallel plate capacitor and resulting field were first studied. This
problem was solved using conformal mapping techniques from complex
variable theory.[6] Finally the finite nonparallel plate problem was solved
using a complicated set of conformal transformations.

60

Figure 20 shows the geometries studied with some terminology. Part (e) of that figure is the configuration of primary interest.

(a) INFINITE PARALLEL PLATES

(b) SEMI-INFINITE PARALLEL PLATES

(c) FINITE PARALLEL PLATES

(d) SEMI-INFINITE NON-PARALLEL PLATES

ANGLE

UNDEFLECTED JET TRAJECTORY

JET OFFSET   SEPARATION

LENGTH

(e) FINITE NON-PARALLEL PLATES
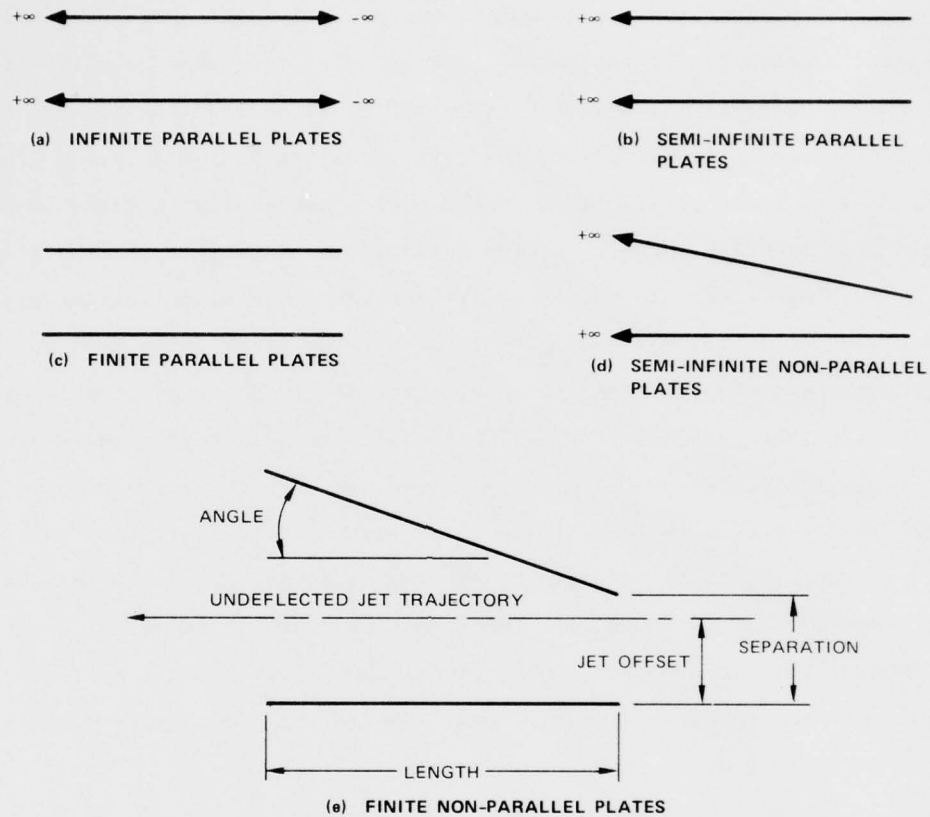
SA-2055-18

FIGURE 20   DEFLECTION PLATE GEOMETRIES

On appraising the solutions to the five cases mentioned, it was found that little accuracy would be lost and much simplicity gained if the semi-infinite nonparallel plate configuration was used to describe the laboratory arrangement. Accordingly, this solution to the field problem is the analytical basis of PHI. A separate section of PHI is used to treat the semi-infinite parallel plate case, whenever the angle between the plates is less than 0.01 radians. The equations used in PHI

61

to evaluate potential at a point are summarized in Appendix D, PHI Equations. The nonparallel plate section of PHI is the only part of the computer model that uses complex arithmetic.

Practical considerations have been included in PHI to tie the analytical model to the apparatus. For example, the field actually fills all space, although its strength drops rapidly away from the plates. Metal parts near the deflecting field will disturb it, since field lines will flow to these parts. Also, the use of a semi-infinite plate length could lead to false large predicted deflections, especially if the flight path were long. For these reasons, limits have been placed on the distance over which the deflecting field acts. The field is assumed to begin at the downstream end of the charging electrode. Here the fringe field is rather weak, but its strength builds rapidly nearer the plates. The field is assumed to end when the drops are more than 10 percent of the plate length beyond the end of the lower plate. Both limits are built into the program; the field strength is assumed to be zero beyond them. Note that the entrance field is more important than that at the exit, since a deflecting velocity imposed there has a longer time to cause deflection. Also, entrance forces are higher than those at the field exit whenever the plate angle is greater than zero.

One measured value is required by PHI and is contained in a DATA card in the program. That value is the jet offset distance (see Figure 20). This value is constant for a given physical assembly. Note that plate separation distance is not constant, but varies with angle. This necessitates occasionally measuring separation distance.

The potential difference between the plates can be varied, but general limits do exist; arcing will occur with high enough voltage. The limit for arcing varies with plate angle, as seen in Figure 21. Note that at large angles, plate separation is smaller and arcing occurs between the plates. At small angles the arcing path is to the charging

62

10,000 — 8,000 — 6,000 — 4,000 — 2,000 — 0

MAXIMUM VOLTAGE BEFORE ARCING — volts

ARC TO CHARGING ELECTRODE

ARC TO GROUNDED DEFLECTION PLATE

0   5   10   15   20   25
DEFLECTION PLATE ANGLE — degrees

SA-2055-19
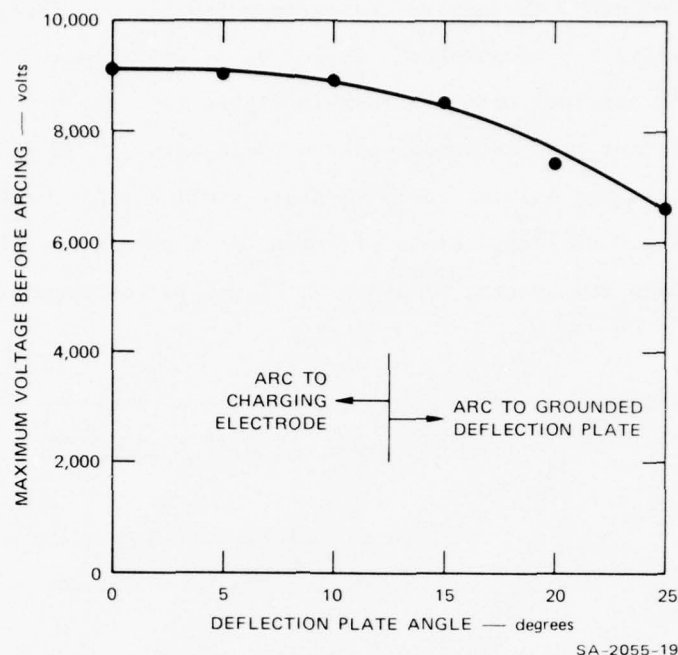
FIGURE 21   PEAK DEFLECTING VOLTAGE VERSUS PLATE ANGLE

electrode. Corona noise was heard at over about 6500 volts, and so DATIN subroutine delivers a warning message in such case. Corona presence will alter the charge on the drops in flight and render the computer model invalid. Furthermore, high deflecting voltages can affect the induced drop charge. Thus, a practical limit on lower plate voltage is roughly 5000 volts.

No experimental verification of the field predictions was performed, primarily because of the difficulty of doing so. Verification would have required imposing a high-voltage ac field on the plates and sensing the induced potential on a capacitive probe. This would have required a very fine probe accurately placed, and it was felt that adequate resolution would be difficult to obtain. Instead, PHI and ELECT were evaluated by noting the magnitudes and directions of forces acting

63

on the charged drops as they passed through the field. These have been found to be entirely reasonable. A plot of field strength in the y-direction for one test case is shown in Figure 22. The data were derived from the optional program output of the force arrays. In the case shown, the lower plate was held at -3450 V; plate angle was 15°; minimum plate separation was 0.09 inch. Field strength for a parallel plate case with similar voltage and spacing is shown in Figure 22 for comparison.

SA-2055-38
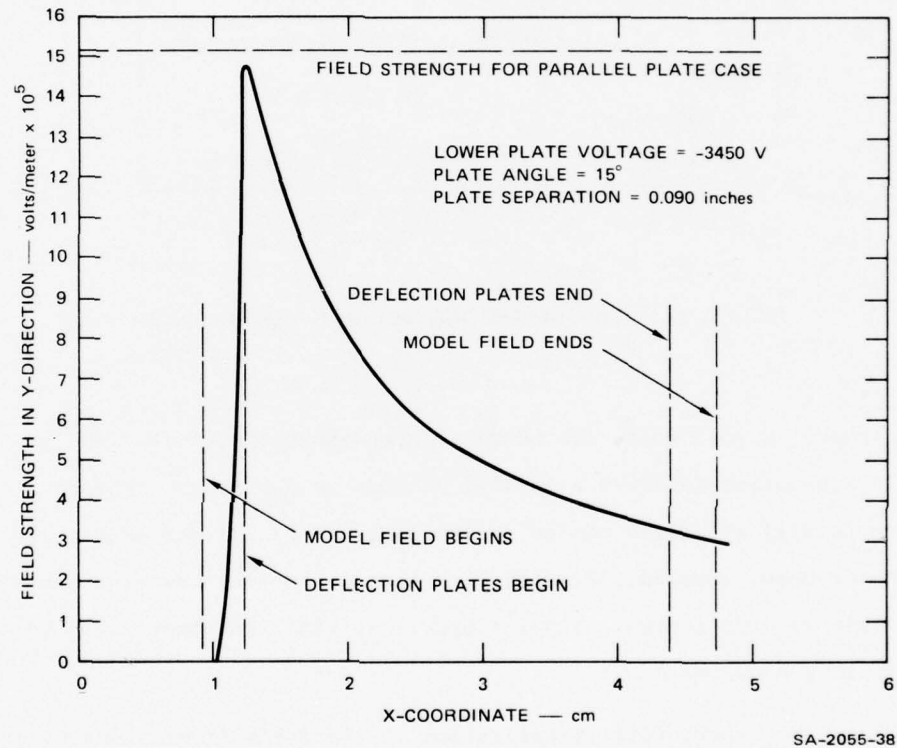
FIGURE 22   DEFLECTING FIELD STRENGTH VERSUS X-COORDINATE

An important check on the model was to note the y-force on a given drop in the parallel plate case. Here, the field strength is simply potential difference divided by plate separation. The computer model exactly agrees in this case, showing that the parallel plate

64

analysis is correct. To check the nonparallel plate theory, a very small angle (0.6°) was assumed. In this case, all the complex variable theory was used. The force predictions were about 3 percent smaller than the parallel plate case, with force dropping slowly through the field.

When the x, y, and z components of deflecting field force on all drops have been computed and stored, control is returned to the executive routine. An immediate branch is made to MUTUAL subroutine. Note that the two-dimensional model in PHI causes all z-forces to be zero.

9.   MUTUAL

In the printing process, unused drops are given no charging signal, and so will travel along the free jet trajectory to strike an ink catcher. The printing drops hold specific charges of like sign, so that they can be deflected above the catcher. MUTUAL subroutine is used to compute the electrostatic forces between each drop and its neighbors. The forces are primarily repulsive and tend to push the drops apart, although small attractive forces can be present when a positive charge is trapped on a drop (see Section III-D-5).

The computing routine is straightforward. The position and charge on a particular drop are noted, as are the charge and relative position of the three preceding and three trailing drops. The force between the drop in question and one of these neighbors is then found from the relation,

$$F = k\frac{q_i q_j}{r^2}$$, where k = electrostatic constant,

$$8.987 \times 10^9 \ \frac{n-m^2}{coul^2}$$

$$q_i = \text{charge on ith drop}$$

65

q_j = charge on jth drop

r = distance between drops i and j.

This force is a vector, lying along a line connecting the two drops. MUTUAL subroutine finds the orthogonal components of the force between the drop in question and its three leaders and three followers. The x-components of the six forces are summed and then stored in REPEL array; the same is true for the y and z force components. This procedure is followed for every drop in flight. When a drop does not have three others in front or behind, those force components are set to zero.

Three assumptions are included in MUTUAL subroutine.

- Drops beyond the adjacent six have no effect. This is justified primarily by the $1/r^2$ factor in the force equation. Also, the magnitude of repulsive forces is typically one or more orders of magnitude less than the deflecting and aerodynamic drag forces.

- The drops are considered to be point charges rather than spheres with a charged surface. This is valid at normal drop spacings. When two drops get very close together, charge redistribution on the surface will occur. This will lower the actual repulsive force below that predicted.

- Within a colinear group of drops, the drops immediately next to the drop in question will not shield it from those farther away. In fact, such shielding does occur and results in less influence from the more distant drops. Shielding occurs when the field is altered because one drop is directly between two others. Ignoring this phenomenon is justified by the small magnitude of force from distant drops and the analytical difficulty of describing the interdrop fields.

MUTUAL subroutine also provides a convenient check point for relative drop positions. Under some circumstances, two drops will collide in flight, resulting in a single larger drop. The computer model will not treat such a case, since it is of no value in printing

66

applications. In MUTUAL, the drop-to-drop distances are computed to find force. If this distance is less than a drop diameter between any of the deflected drops indicating a collision, an error message is printed and the program stops. If drops that were given no charging signal collide, the program continues to run, since these are assumed to be unused.

No experimental verification of MUTUAL subroutine was performed because of the simplicity of the model and the difficulty of observing pure repulsive effects. The computed force values were found to agree with hand calculations based on predicted drop positions and charges. The relatively small magnitude of repulsive forces indicates their small role in drop trajectory. Repulsive forces are most significant on the leading and last drop of a deflected group, since these see a charged body on only one side.

Once the total x, y, and z forces on all existing drops have been found and stored in REPEL array, control returns to the executive routine. An immediate branch is then made to AERO subroutine.

10. <u>AERO</u>

The ink drops in flight are affected by aerodynamic drag. The magnitude of the drag force on a drop depends on its velocity and its position relative to neighboring drops and the undeflected jet. When AERO subroutine is called, the state vector for all existing drops is known. AERO then computes the orthogonal components of aerodynamic drag force on each existing drop. These force values are stored in DRAG array.

Aerodynamic drag experienced by a single sphere moving in a fluid medium has been extensively measured. The standard drag coefficient versus Reynolds' number curve is well-known.[7] The same cannot be said, however, when the number of spheres becomes greater than one. Although

67

it is known that the presence of other spheres in its proximity will significantly influence the drag on the sphere of interest, quantitative information is very limited.

This fact required an experimental approach to creation of the subroutine, in which the single sphere drag coefficient is modified by empirical factors derived from observations. Interference drag coefficients for an ink drop in various flight formations were obtained by measuring the motion of the drop versus time.

If the drop of interest were a single sphere isolated in space, the drag coefficient would simply be

$$(C_D)_{ss} = \frac{24}{R_e} + \frac{4}{(R_e)^{1/3}} \quad ,$$

where

$$R_e = \frac{\rho_a d v_o}{\mu_a} \quad ,$$

the Reynolds number for the drop; ρ_a is air density, d is drop diameter, v_o is drop speed, and μ_a is air viscosity.

A drop formation pattern is shown in Figure 23, where the drop of interest is preceded by two drops and followed by another and is near to the undeflected jet. Such a configuration results in a modified drag coefficient of the form

$$C_D = C_D^* \bullet (C_D)_{ss}$$

where

$$C_D^* = 1 - 0.84 \exp(- y_o/d) - \left[1 - \exp(-y_o/d)\right] \left[(C_D)_{1L} + (C_D)_{2L} + (C_C)_{1T}\right]$$

68
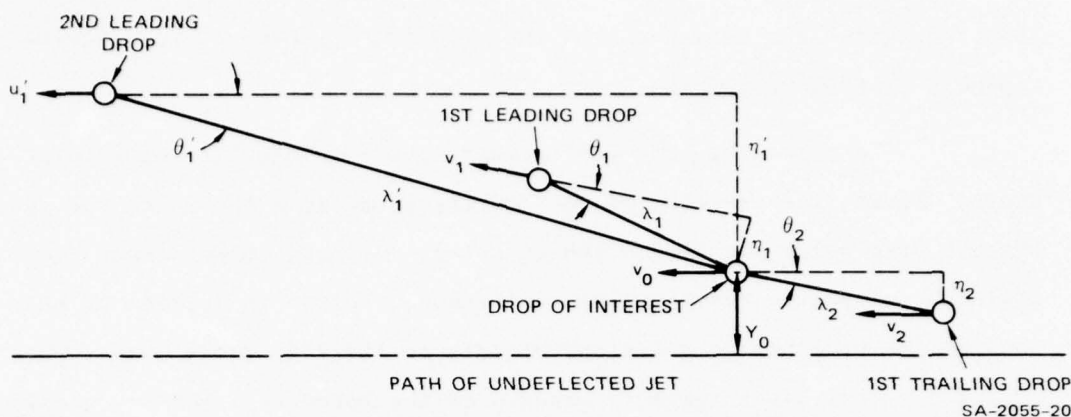
FIGURE 23   DROP SEPARATION AND OFFSET DISTANCES

and

$$(C_D)_{1L} = 0.435 \exp\left[-0.020(\lambda_1/d) - 0.188(\eta_1/d)^2\right]$$

$$(C_D)_{2L} = 0.178 \exp\left[-0.022(\lambda_1'/d) - 0.188(\eta_1'/d)^2\right]$$

$$(C_D)_{1T} = 0.217 \exp\left[-0.147(\lambda_2/d) - 0.188(\eta_2/d)^2\right] \quad .$$

The λ's and η's are defined in Figure 23; y_o is the vertical deflection
of the drop of interest. The subscripts 1L, 2L, and 1T refer to the two
leading and one trailing drop, respectively. The term $0.84 \exp(-y_o/d)$
is used to account for the nearness to the undeflected jet. Note that
when the drop is three or four diameters from the jet, the equation
essentially becomes

$$C_D^* = 1 - (C_D)_{1L} - (C_D)_{2L} - (C_D)_{1T} \quad .$$

69

The coefficients in these equations are based on experimental measurements. These equations and an account of the measuring procedure are described in Appendix E, AERO Derivation.

The resulting drag coefficient equation demonstrates several facts. First, the presence of neighboring drops acts to reduce the aerodynamic drag below its single sphere value. Second, interference effects diminish as spacing between drops increases. Third, the effect of nearness to the undeflected jet drops rapidly as the drop moves away. This empirical result is actually a measure of the boundary layer surrounding the jet.

A number of assumptions were required during the creation of this subroutine. The drag on a particular drop was assumed to be affected only by the two closest leading drops and the one closest trailing drop. Other neighboring drops also have an effect but of diminishing magnitude. The measuring procedure also becomes much more complicated as the number of effective drops increases.

The aerodynamic Reynolds number of drops from the print head can be varied within limits (from about 100 to 200). Over this range, the dependence of C_D on R_e was not evident. As a result, it is assumed that the functional dependence of C_D on R_e is the same as for $(C_D)_{ss}$. This is reflected in the fact that C_D^* is not a function of R_e.

A third assumption was that aerodynamic effects are independent of all electrostatic effects. The main reason for this is the fact that drag force is typically an order of magnitude or more greater than the deflecting or repulsive forces on the drops.

A fourth assumption is that the drops are spheres. This is true only after the drops have traveled 10 to 20 spacings from the separation point. Surface tension forces usually result in drop "wobble" that damps out after separation.

70

A limitation on AERO subroutine is that derivation of the equation for C_D^* was based on ink drop data taken when $R_e \approx 130$. The equation will give less accurate drag estimates when Reynolds number greatly differs from this value. Within the limits of the apparatus, R_e cannot be radically changed from this value.

AERO subroutine computes drag coefficient for the drop of interest using the equations given. In the process, the most influential preceding and trailing drops must be found. To do this, the program first finds the value of $(C_D)_{1L}$ due to all preceding deflected drops and stores the largest value. Then, the value of $(C_D)_{2L}$ is found due to all preceding deflected drops except for the drop giving the largest $(C_D)_{1L}$ value. Again, the maximum value of $(C_D)_{2L}$ is stored. The same testing procedure is used to find the largest value of $(C_D)_{1T}$. Using these three values will correctly yield the smallest drag coefficient C_D. Note that the presence of neighboring drops is always such that the drag on the drop of interest is reduced.

Once the drag coefficient value is obtained, the drag force is found from the relation

$$D = \frac{\pi}{8} \rho_a d^2 C_D v_o^2 \quad ,$$

where D is drag force. This force is a vector in a direction opposite to the drop velocity vector. The force on each drop is broken into its x, y, and z components; these are stored in DRAG array for later use.

The calculations in AERO require values for the density and viscosity of air. These are entered via a DATA card. The values used are for 71°F and sea level conditions.

71

No specific verification procedure was used for AERO subroutine, since it is based on a large body of experimental data. The aerodynamic drag model was created to fit the observations. The lack of prior work in this area of multiple spheres in flight dictated this approach.

A number of cases were studied during the AERO experiments. These included a drop shielded by one preceding drop, by two preceding drops, and by two preceding drops plus a trailing drop. The procedure outlined in Appendix E allowed the lab measurements to yield drag coefficient values for these cases. The experimental cases and resulting drag coefficients are summarized in Table 2. As a point of comparison, the drag coefficient of a single sphere, traveling with $R_e = 130$, is $(C_D)_{ss} \approx 0.98$. The tabulated values of C_D under the conditions shown were used in deriving the empirical expressions given at the beginning of this section.

When AERO subroutine is completed, control is returned to the executive routine. The executive routine then checks the value of the print control; if IPRT = 1, the values of the x, y, and z force components in the arrays STATIC, DRAG, and REPEL are printed for every existing drop. This optional output lists forces in the order:

- x-components of deflecting field, aerodynamic drag, and repulsion forces
- y-components of these forces
- z-components of these forces.

This output is quite valuable, since it indicates what is happening to each drop. Note that nowhere in the program are any z-forces applied to the drops, so these will all be zero. The program has retained the z-component for completeness and in case any z-forces are to be considered at a later time.

Table 2

DRAG COEFFICIENTS OF A DROP
WITHIN VARIOUS DROP FORMATIONS

	λ_1/d	$\lambda_1'd$	$\lambda_2 d$	C_D
Drop shielded by	3.5	∞	∞	0.54
one preceding drop	7.3	∞	∞	0.56
	10.8	∞	∞	0.59
	21.3	∞	∞	0.64
	75.0	∞	∞	0.75
Drop shielded by	3.3	6.0	∞	0.40
two preceding drops	3.3	19.5	∞	0.43
	3.5	73.0	∞	0.50
Drop shielded by two	40.0	72.0	2.5	0.56
preceding drops and	40.0	71.0	3.5	0.63
followed by one	40.0	67.0	7.5	0.63
trailing drop	40.0	63.0	11.5	0.65

Trial runs of the program have indicated several notable points relative to the forces acting on the drops. In the x-direction, the dominant force is from aerodynamic drag, with magnitudes on the order of 10^{-6} to 10^{-7} newtons. Deflecting field forces can get as large as 10^{-8} newtons in the x-direction; these result from the curved field lines present in field fringes and when plate angle is not zero. Repulsion forces can get as large as 10^{-8} newtons in the x-direction.

In the y-direction, the dominant force is due to the deflecting field, with peak magnitudes on the order of 10^{-6} newtons. Typical drag y-forces can get as large as 10^{-7} newtons, especially if the drop is strongly deflected. Repulsion forces in the y-direction can also get as large as 10^{-7} newtons.

73

These results indicate that predictions of drop deflection distance and arrival time primarily depend on accurate computation of field strength and aerodynamic drag, respectively. Drop repulsion plays a minor but important role.

Gravitational force on the drops is on the order of 10^{-8} newtons in the y-direction. This is considered to be small enough to justify ignoring this force.

After the executive routine has checked the print control and possibly printed the force values, it computes the acceleration of each drop in the three component directions. The simple dynamic equation is

$$a_i = \frac{\Sigma F_i}{m} \quad ,$$

where

$a =$ acceleration in the i-direction

$m =$ drop mass

$\Sigma F_i =$ sum of the 3 forces in the i-direction.

Acceleration is calculated in this manner each time the program passes through the drop ballistics loop. Thus, acceleration is constantly updated to account for current force values. The new values of drop acceleration then replace the previous values in the state vector. At this point, the executive routine calls STEP subroutine.

11. STEP

STEP subroutine is used to increment the state vector for every existing drop. At the time STEP is called, the updated acceleration components are known, as are the drop position, velocity, and elapsed time for which the forces were computed. The incremental time interval δ is

74

also known. The state vector is then updated according to the relations

$$x_{new} = x_{old} + \dot{x}\,\delta$$

$$\dot{x}_{new} = \dot{x}_{old} + \ddot{x}\,\delta$$

$$t_{new} = t_{old} + \delta \quad ,$$

where the dot indicates a time derivative. Position and velocity in y- and z-directions are similarly treated. The updated state vector is then used the next time through the drop ballistics loop. Forces are computed based on the new positions and velocities. This incremental procedure is followed until the drops have propagated through space to strike the imaginary printing surface.

Two checks on drop flight are made within STEP. First, the x-positions of all the drops are surveyed. If any have traveled 95 percent or more of the distance to the printing surface, the indicator NEAR is set to 1. This will result in decreasing the incremental time interval when control is returned to the executive routine. This is done to more accurately find drop arrival time and deflected distance.

The second check deals with the x-position of each drop. If it equals or exceeds the distance to the printing surface, the state vector for that drop is frozen; its position and velocity are not incremented further. When all existing drops have reached this point, the indicator IDONE is set to 1. This will allow an exit from the drop ballistics loop when control is returned to the executive routine.

Because of the straightforward nature of STEP, no verification was required. One subtle inaccuracy introduced in STEP, however, should be mentioned. The freezing of the state vector for drops that have

75

arrived implies the existence of a drop frozen in space with a given velocity and charge. When forces on the drops are recomputed in a following pass through the drop ballistics loop, they will be based on these positions and velocities. Drops that are frozen are not affected since they cannot be moved. Drops about to strike the surface can be influenced, however, since they will see misplaced preceding drops that affect their aerodynamic drag and produce repulsive forces, when in reality such drops would already be deposited on the printing surface. This inaccuracy does not cause significant problems because the time for the erroneous forces to act is small; influence of these forces on final drop position will be even smaller because of the double integration present in the stepping method.

After STEP is completed, control is returned to the executive routine. If variable NEAR = 1, the stepping time increment will be shortened when the drop ballistics loop is rerun, since the drops are nearing their destination. If the variable IDONE = 0, indicating that some or all drops are still in flight, the print control is checked. If IPRT = 1, the updated values in the state vector for all existing drops are printed. These appear in the order: x, y, z, $\dot{x}$, $\dot{y}$, $\dot{z}$, $\ddot{x}$, $\ddot{y}$, $\ddot{z}$, q, and t. From this point, the drop ballistics loop is run again. If all drops to be created do not yet exist, CREATE subroutine will be called. If all drops have been created, a new computation of forces will begin immediately, based on the new state vector quantities and beginning with ELECT. If IDONE = 1, indicating that all drops have arrived, the state vector will not be printed and the executive routine will leave the drop ballistics loop by calling DATOUT.

12. DATOUT

  DATOUT subroutine is used to deliver the output parameter values resulting from the operating conditions imposed on the computer model. This subroutine is called after all drops to be studied (MAXPTS) have arrived at the imaginary printing surface. Many of the output values are converted to common units before printing.

  The output parameters with units as delivered by the Analytical Computer Model are:

- Velocity of jet just outside the orifice, inches per second
- Flow rate of ink, cubic centimeters per minute
- Rate of drop production, drops per second
- Diameter of drop, inches
- Drop spacing just after formation, inches
- Size of a character (distance between the most deflected and least deflected drop), inches
- Distance from orifice to drop separation point, inches.
- Drop charge level, coulombs, for all created drops
- Drop deflection distance, inches, for all created drops
- Drop flight time, seconds, for all created drops.

  At the time DATOUT is called, all the output parameters are known except for character size. This value is determined from the y-position values in the state vector array. It is assumed that only the drops given positive charging voltages are to be used in a character; others may be deflected because of drop-induced charge, but are assumed to hit the ink catcher. Furthermore, it is assumed that the deflection distances and arrival times for the first 24 drops will be ignored. This is because these drops have no predecessors, which has a great effect on the computed aerodynamic drag and repulsion forces. Later drops, which have these as forerunners, are more closely related to the drops in real applications.

77

Thus, the y-displacements of all deflected drops after the first 24 are surveyed. The difference between the maximum and minimum values is then the predicted character size.

While the output values are self-explanatory, a comment is in order about the drop deflection distances and arrival times. As mentioned above, the first drops break the way for those following. Thus, distance and time for the leading drops are unrealistic. Drops following the first 12 or 24 are more likely to portray actual performance. In fact, by observing the position of the same drop in successive groups of 24, the time for the startup transient in the model to die out can be noted.

The y-positions and arrival times together yield an indication of character appearance. In this type of ink jet printing system, there must be a relative velocity between the printing head and printing surface in the z-direction (see Figure 19). Knowing the y-position gives one coordinate on the surface. Knowing arrival time and relative z-velocity of the surface gives the other. Thus, if a slanted bar is to be printed, the output should show decreasing y-deflections with increasing arrival times for the drops used.

The testing and vector holding procedure used in STEP halt the drop only after its x-coordinate equals or exceeds the distance to the printing surface. Since the stepping interval is $1/f$ at this point, that is the possible error in arrival time. The y-coordinates are fixed at the particular arrival time, so they also may have a small error as a result of this termination procedure.

After the output values have been printed, control is returned to the executive routine. The executive then calls EXIT, and the analysis of the ink jet configuration studied is finished.

78

IV   PROGRAM PERFORMANCE

The Analytical Computer Model as a complete tool was evaluated by comparing intermediate and final program predictions with laboratory observations, using the same input conditions in both cases. This could be done only after all the subroutines had been verified, and only a few tests of overall program performance were made.

The comparison proceeded as follows. In the laboratory, an operating pressure, frequency, and voltage were chosen so that drop formation would be stable and few satellites would be present. Drop separation point had to be within the first half of the charging electrode. Under these conditions, a pattern of charging voltages and a deflecting voltage was imposed, such that the deflected pattern was of printing size. The laboratory input conditions were noted and these values used in the computer analysis.

Two comparisons between the corresponding computer output and observations were made. First, the optional state vector output was noted at a time when the drops were near the downstream end of the deflection plates. In effect, this provided values of drop coordinates at a particular moment. The same situation could be observed in the laboratory under stroboscopic illumination, allowing comparison of the actual and predicted flight patterns. The second comparison was that of the program output parameters with measured values.

Two test cases are described, not as exceptionally good or bad cases, but rather as an indication of levels of performance that can be expected. Predictions with more or less accuracy probably exist for different input conditions.

In each example, 36 drops were created (MAXPTS = 36) and flew to an imaginary printing surface 2.5 inches away. The first 12 drops were considered as forerunners, breaking the way for those following. Their motion was ignored, since in actual operation, there is never a "first" drop, but always a stream. The remaining 24 drops were broken into four groups of 6 drops each; two groups were given no charging voltage, while the other two groups were deflected as if to print. The drops given no charging voltage could also be neglected, since from a practical standpoint they would not be used for printing. Thus, attention in the examples was focused on 12 deflected drops.

A.   Test Case 1--Parallel Plates

The input parameters for this test case were as follows:

Type of ink used	A. B. Dick 16-6000
Ink temperature	70°F
Ink density	1.026 gm/cm^3
Ink surface tension	37.0 dyne/cm
Ink resistivity	62.1 ohm-cm
Ink viscosity	1.75 cp
Ink sonic velocity	1573 m/sec
Ink supply pressure	40.0 psig
Crystal voltage	45 V, zero-to-peak
Crystal driving frequency	65,270 Hz
Charging electrode spacing	0.040-inch
Deflection plate length	1.25-inch
Deflection plate separation	0.130-inch
Deflection plate angle	0.0°
Deflection plate voltage	-1350 volts
Distance to printing surface	2.5 inches

80

Drop Number	Charging Voltage	Drop Number	Charging Voltage	Drop Number	Charging Voltage
1	0	9	250	17	0
2	0	10	225	18	0
3	0	11	200	19	300
4	0	12	150	20	275
5	0	13	0	21	250
6	0	14	0	22	225
7	300	15	0	23	200
8	275	16	0	24	150

In this case, the charging sequence is repeated for each of the two deflected groups. Also, the entire sequence is started over for following drops, so that drop 25 sees 0 volts at the electrode, drop 31 sees 300 volts, and so on.

The predicted and actual drop coordinates in flight are compared in Figure 24. The agreement at this intermediate point is good. For the 12 deflected drops, the errors in y-coordinate range from 9 percent low to 11 percent high in the worst cases; 8 of the 12 drops are within ± 5 percent of predicted positions. In the x-direction, the greatest deviation is less than two drop diameters.

The output parameters given by the program are shown in Table 3, along with measured values and errors. In this example, the deflection distances of only one group of 6 drops are of concern.

These results indicate considerable accuracy of the predictions in this case. The error in character size is primarily due to the error in deflection distance of drop 31. These results are discussed further in Section IV-C.

81

FIGURE 24   IN-FLIGHT DROP COORDINATES, TEST CASE 1

SA-2055-39

82

Table 3

OUTPUT PARAMETERS, TEST CASE 1

Output Parameter	Predicted Value	Measured Value	Error
Initial jet velocity	784.8 in/sec	783.2 in/sec	+0.2%
Ink flow rate	3.80 cm^3/min	*	
Drop rate	65,270 drops/sec	65,270 drops/sec	
Drop diameter	4.88 mils	*	
Initial drop spacing	12.02 mils	12.0 mils	+0.2%
Character size	67.1 mils	56 mils	+20%

Drop Number	Charging Voltage, volts	Predicted Charge Level, coulombs x 10^{-12}	Predicted Deflection, mils, @ x = 2.5 in.	Measured Deflection, mils, @ x = 2.5 in.	Error
31	300	-2.07	105.3	95.5	+10%
32	275	-1.51	75.7	77.0	- 2%
33	250	-1.37	67.6	68.0	- 1%
34	225	-1.24	62.3	61.0	+ 2%
35	200	-1.10	55.1	54.5	+ 1%
36	150	-0.78	38.2	39.5	- 3%

*These terms were not measured, since they are a direct consequence of jet velocity and drop spacing.

B.   Test Case 2--Angle Plates

The input parameters for this test case were as follows:

Type of ink	A. B. Dick 16-6000
Ink temperature	72°F
Ink density	1.026 gm/cm^3
Ink surface tension	37.0 dynes/cm
Ink resistivity	60.8 ohm-cm
Ink viscosity	1.70 cp
Ink sonic velocity	1574 m-sec

83

Ink supply pressure			32.9 psig		
Crystal voltage			110 volts, zero-to-peak		
Crystal driving frequency			53,000 Hz		
Charging electrode spacing			0.040-inch		
Deflection plate length			1.25 inches		
Deflection plate separation			0.090-inch		
Deflection plate angle			15.0°		
Deflection plate voltage			-3450 volts		
Distance to printing surface			2.5 inches		

Drop Number	Charging Voltage	Drop Number	Charging Voltage	Drop Number	Charging Voltage
1	0	9	88	17	0
2	0	10	74	18	0
3	0	11	55	19	86
4	0	12	38	20	75
5	0	13	0	21	65
6	0	14	0	22	55
7	135	15	0	23	48
8	115	16	0	24	65

In this case, the charging pattern is different for each of the two groups of deflected drops. As before, the first 12 drops created act as forerunners; drops 25 through 36, with the same charging pattern as the first 12, are considered instead.

Comparison of the predicted and actual drop coordinates in flight is shown in Figure 25. The agreement in this case is not as good as in Test Case 1. With the exception of one deflected drop, all the predicted deflections are too low, some by as much as 22 percent, In the x-direction, the greatest error is about 2 drop diameters.

The output parameters for this test case are given in Table 4. In this example, the deflection distances for both groups of 6 deflected drops are of interest, since their charging patterns were different.

84

DEFLECTION PLATE VOLTAGE = -3450 V
DEFLECTION PLATE ANGLE = 15°
INK SUPPLY PRESSURE = 32.9 psig
FREQUENCY = 53 kHz

■ Measured Locations
● Predicted Locations

END OF DEFLECTION PLATES

◄— JET DIRECTION

Y-COORDINATE — mils

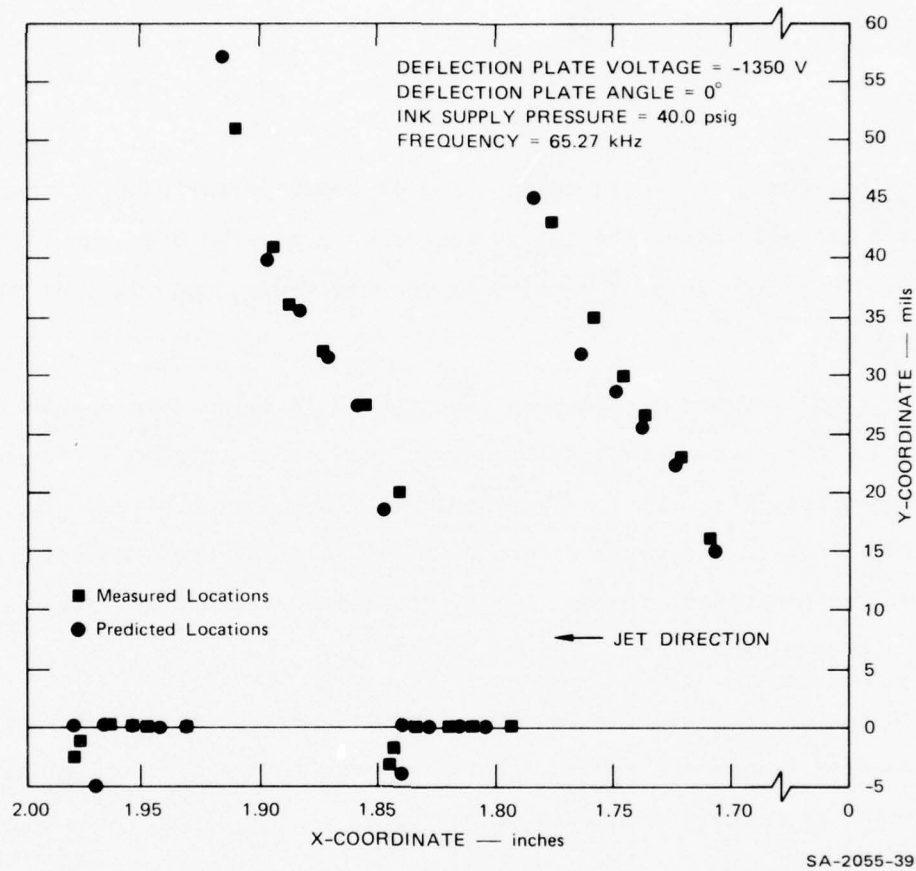X-COORDINATE — inches

SA-2055-40
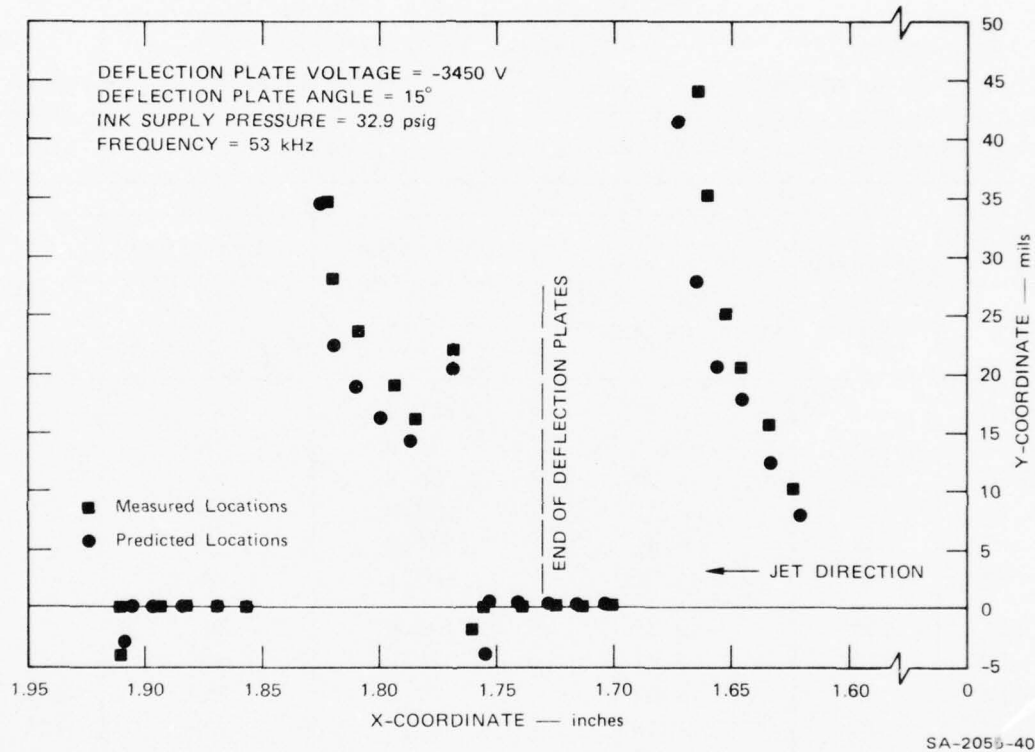
FIGURE 25   IN-FLIGHT DROP COORDINATES, TEST CASE 2

85

Table 4

OUTPUT PARAMETERS, TEST CASE 2

Output Parameter	Predicted Value	Measured Value	Error
Initial jet velocity	706.2 in/sec	713.7 in/sec	-1.1%
Ink flow rate	3.43 cm^3/min	*	
Drop rate	53,000 drops/sec	53,000 drops/sec	
Drop diameter	5.06 mils	*	
Initial drop spacing	13.33 mils	13.43 mils	-1.0%
Character size, 1st Group	37.6	35	+7.0%
Character size, 2nd Group	85	75	+13%

Drop Number	Charging Voltage, volts	Predicted Charge Level, coulombs x 10^{-13}	Predicted Deflection, mils, @ x = 2.5 in.	Measured Deflection, mils, @ x = 2.5 in.	Error
19	86	-6.57	65.5	67	-2%
20	75	-4.51	42.3	52	-19%
21	65	-3.89	35.6	44	-19%
22	55	-3.31	30.8	37	-17%
23	48	-2.91	27.9	32	-13%
24	65	-4.30	41.1	45	-9%
31	135	-10.31	104.9	100	+5%
32	115	-6.87	65.6	78	-16%
33	88	-5.07	47.9	60	-20%
34	74	-4.46	41.6	48	-19%
35	55	-3.19	29.3	36	-19%
36	38	-2.15	19.7	25	-21%

*These terms were not measured, since they are a direct consequence of jet velocity and drop spacing.

These results indicate less accuracy than those in Test Case 1. The errors are of larger magnitude and with one exception show a low prediction.

C.   Comments

The two examples demonstrate a number of things about the Analytical Computer Model. First, the model provides a general picture of how the drops will behave in flight and where they will land. The accuracy of the predictions depends on the input conditions used. The predictions in Test Case 1 were quite good; errors were larger in Test Case 2, but a qualitative view of drop behavior was still delivered. Second, the predictions of jet velocity and drop characteristics are very accurate; errors greater than $\pm$ 3 percent over the range of parameters are not expected. Third, drop separation point was not accurately predicted in either case; the value was too low, so a dummy value stored in SEPDIS was used instead.

Laboratory measurements were required to make the comparisons. In most cases, these may contain errors as large as $\pm$ 5 percent. This is particularly true of the charging voltage levels, since the charging signal was not always flat during drop separation. Measurements of x-coordinates for the in-flight comparison were repeatable to within $\pm$ 0.004-inch; y-coordinates were accurate within $\pm$ 2 mils. It was noted during measurement of drop coordinates that the drops would sometimes drift. This was attributable to air currents, pressure variations, and phase shift between the charging signal and drop separation. This made the measurements difficult; thus, the reported values should not be taken as absolute.

It is felt that three interrelated sources of error exist. First, the measurements of input and output parameters contain some error. Second, the analytical treatment required that numerous approximations and assumptions be made. Third, the charging electrode plates and the deflection plates could not be perfectly aligned.

The errors in predicted drop positions come from the subroutines used to compute charge and forces on the drops. Most of the errors are random in nature, with predicted values being slightly greater or less than actual.

87

CHARGE subroutine appears to be responsible for part of the error in predicted deflection distances. This distance is a direct function of the y-forces on a drop; the primary y-force is the product of deflecting field strength and drop charge. Since all drops pass through the same field, random differences in errors can be attributed to charge discrepancies. Errors in induced charge prediction are explainable by the strong dependence on the geometry of the jet and drops near the drop separation point. If this geometry deviates from that used in the empirical correction factors, errors will result.

Drop deflection is influenced to a lesser extent by repulsive forces between drops. Errors can exist here because of the assumption that the drops are point charges instead of spheres. The error in position of the leading drops in the test groups is more positive than the errors for following drops. If the charges on the drops distribute themselves to form a dipole, the repulsive forces will be reduced, as will the deflection caused by these forces. The field strength predictions based on the assumed geometry are thought to be good, especially for small plate angles. The large errors in the same direction in Test Case 2 indicate that actual field strength is greater than that predicted, particularly at the field entrance. This is probably caused by the nonideal geometry at the entrance and because the drops pass only about four diameters away from the upper plate at that point. Since more time exists for entrance forces to affect drop deflection, small errors in entrance field strength can become proportionately larger in terms of deflection. Thus, the systematic errors in Test Case 2 are mainly due to the difference between the actual and idealized field geometry. The aerodynamic drag calculations are acceptably accurate. Measurement of transit time for one drop in Test Case 2 showed an error less than 2 percent. Thus, errors in predicted deflection are not due to inaccurate residence time in the deflecting field.
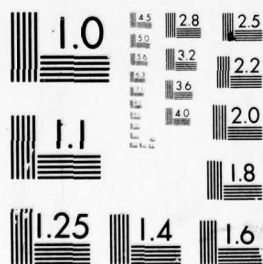
88

2 OF

AD
A038438

MICROCOPY RESOLUTION TEST CHART
NATIONAL BUREAU OF STANDARDS-1963-

As mentioned in the subroutine descriptions, the arrival time of each drop is also listed as an output. Because of the incrementing procedure used, this arrival time can be accurate only to within 1/frequency. In Test Case 1, the drops land in the order in which they left the print head, although they are much closer together in the x-direction than when formed. Predictions show that the first four drops will arrive at the same time, followed by drops 5 and 6. This crude comparison shows that in this case, a general picture of arrival time is given. For a more accurate prediction of flight time, a shorter stepping interval near the printing surface or an interpolation routine would be needed. In Test Case 2, predicted arrival times are not entirely consistent with observations.

As mentioned earlier in this report, the program contains a starting transient. The first drops created must break the way for the followers. They will see greater aerodynamic drag, and thus be displaced in the x-direction. This displacement will affect the following drops, since drag and repulsion forces on a drop depend on the positions of those ahead. In reality, the main stream is always present, so there is no starting transient. Several groups of deflected drops must be created before these starting effects die out. The duration of the starting transient depends on the input conditions. In general, the second or third group of drops with a particular charging pattern will be within 2 percent of the steady-state predictions. The transient errors usually predict deflections greater than the steady-state values.

V PROGRAM LIMITS

Throughout the discussions of the subroutines, various limits on program parameters or combinations of parameters have been mentioned. These limits are summarized in Table 5 along with the basis for each limit. In most cases, if the limit is exceeded, a warning message is printed; in some cases, the program will stop.

The limits shown in the table should be considered general and approximate. Ink properties are those for the five A. B. Dick inks; other inks will work in ink jet printers. Regarding pressure, crystal voltage, and frequency, working combinations of these beyond the stated limits could surely be found, although they would have little application in printing applications. The geometric limits are based on the physical apparatus and practicality. For example, a larger charging electrode gap could be designed, but since a small gap is most desirable, there is no reason to do so. Trade-offs are also available regarding the charging and deflecting voltages, and exceptions to the limits probably exist. The ranges shown are based on practical considerations and familiarity with ink jet printing systems.

At least two other limits appear in the program. One is a test of time to charge a drop. If the time is greater than 20 percent of the time between drops, a message is printed indicating that ink resistivity is too high. In the other test, if two of the deflected drops come together in flight, the program stops. Such a case would be unacceptable in printing applications.

The overall program was evaluated under only a limited number of test conditions. Thus, although the program will function over the

Table 5

PARAMETER LIMITS

Parameter	Minimum	Maximum	Basis
Ink temperature, $^\circ$F	50	90	Likely room temperature range.
Ink density, gm/cm^3 Ink viscosity, cp Ink surface tension, dyne/cm Ink resistivity, ohm-cm Ink sonic velocity, m/sec	1.023 1.34 36.8 55 1553	1.050 3.28 65 222 1617	All ink properties are based on the five A. B. Dick inks within the given temperature range.
Ink supply pressure, psig Ink supply pressure, psig	10	80	Jet velocity too low below this. System safety; excessive jet momentum.
Crystal Voltage, v,z-p Crystal Voltage, v,z-p	15V	200V	Poor breakup without some modulation. No benefit from higher voltages.
Driving frequency, kHz Driving frequency, kHz	15	→	Poor breakup below this value. $\pi d_{jo} f/v_{jo} \leq 1.0$

Charging electrode gap,
  inch
Charging electrode gap,
  inch
	0.020	0.120	Practical limit.
			
			Physical limit.

Deflection plate length,
  inch
Deflection plate length,
  inch
	0.5	2.5	Needed for deflection.
			
			Little benefit from longer plate.

Deflection plate angle, degrees	0	25	Physical limit.
Deflection plate separation, inch	0.060	0.130	Physical limit.
Deflection plate Voltage, volts	-500	-6500	Needed for deflection Danger of arcing above this level.

Drop Charging Voltage,
  volts
Drop Charging Voltage,
  volts
	20	400	Needed to deflect above catcher.
			
			Higher voltages interfere with jet breakup.

Distance to Printing Surface, inch Distance to Printing Surface, inch	1.0	4.0	Minimum deflection; short deflection plates. Danger of distortion at larger distances.

ranges of parameters given, little feeling is available as to how accurate the predictions will be with various parameter combinations. Additional tests and comparisons of the entire computer model should be performed to better define its accuracy under various combinations of input parameters. In general, the program is expected to be the most accurate with nonextreme parameter values and under conditions simulating useful ink jet printing applications. For example, the A. B. Dick printing head is most useful at frequencies above about 40 kHz.

In addition to parameter limits, the computer model also has one distinct limitation: it is highly dependent on the particular printing head and deflection plate geometry in use. Printing head dependence exists in the orifice coefficient relations, stream perturbation at an impressed voltage, and the details of drop formation. Only gross similarity between different heads is expected. Deflecting plate geometry plays a role in relative jet location and fringing effects. Both facts require that the program be "fitted" to the physical apparatus on hand. Comments were made in Section III, and are also present in the program listing, where such fitting is needed.

VI EXPERIMENTAL HARDWARE

Test apparatus was assembled for the verification phase of this project. Figure 26 shows the test station. Testing apparatus included an ink delivery system, mechanical hardware, and electrical apparatus.
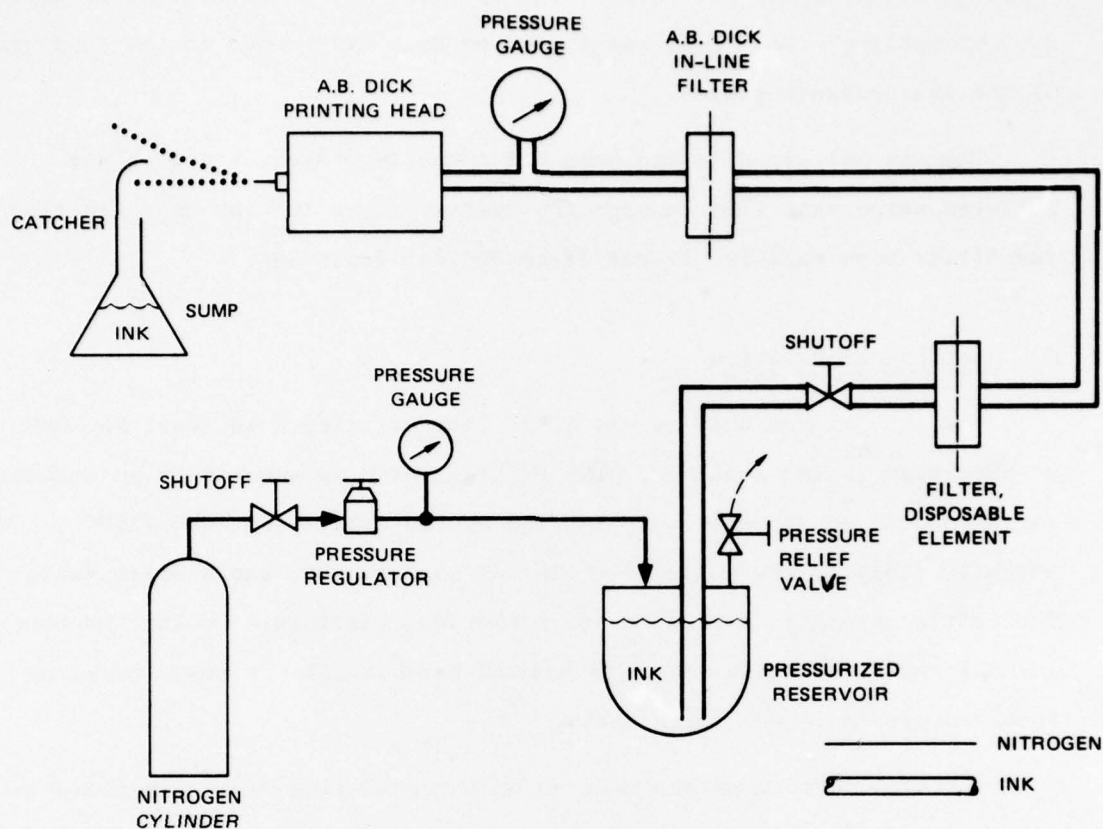
A. Ink Delivery System

A diagram of the ink delivery system is shown in Figure 27. The pressure source is a bottle of compressed nitrogen. The gas flows through a pressure regulator to the ink reservoir. The reservoir consists of a thick-walled glass cup covered by an anodized aluminum plate. A gasket between the cup and plate provides the pressure seal. The plate contains the nitrogen inlet, a pressure relief valve, a stainless steel ink outlet tube, and a filling port. The ink outlet tube connects to a stainless shutoff valve and disposable element filter. The filter, made by Millipore Corporation, typically held a Teflon element of 10 μ pore size. The filter outlet adapted to the plastic inlet tube provided with the A. B. Dick printing head assembly. An in-line filter was part of this assembly. It contains a stainless steel mesh element. Although this element can be removed and cleaned, it is not easily done. Just before entering the printing head, the plastic ink tube was broken and a stainless "T" inserted. One leg of the "T" went to an accurate pressure gauge, whose reading was taken as pressure just upstream from the orifice. Ink leaving the print head passed into a catcher. A grounded electrode in the catcher dissipated the charge carried by the drops.

When ink in the system was changed, all wetted parts were flushed with deionized water and blown dry. Occasionally, sediment from the ink was

95
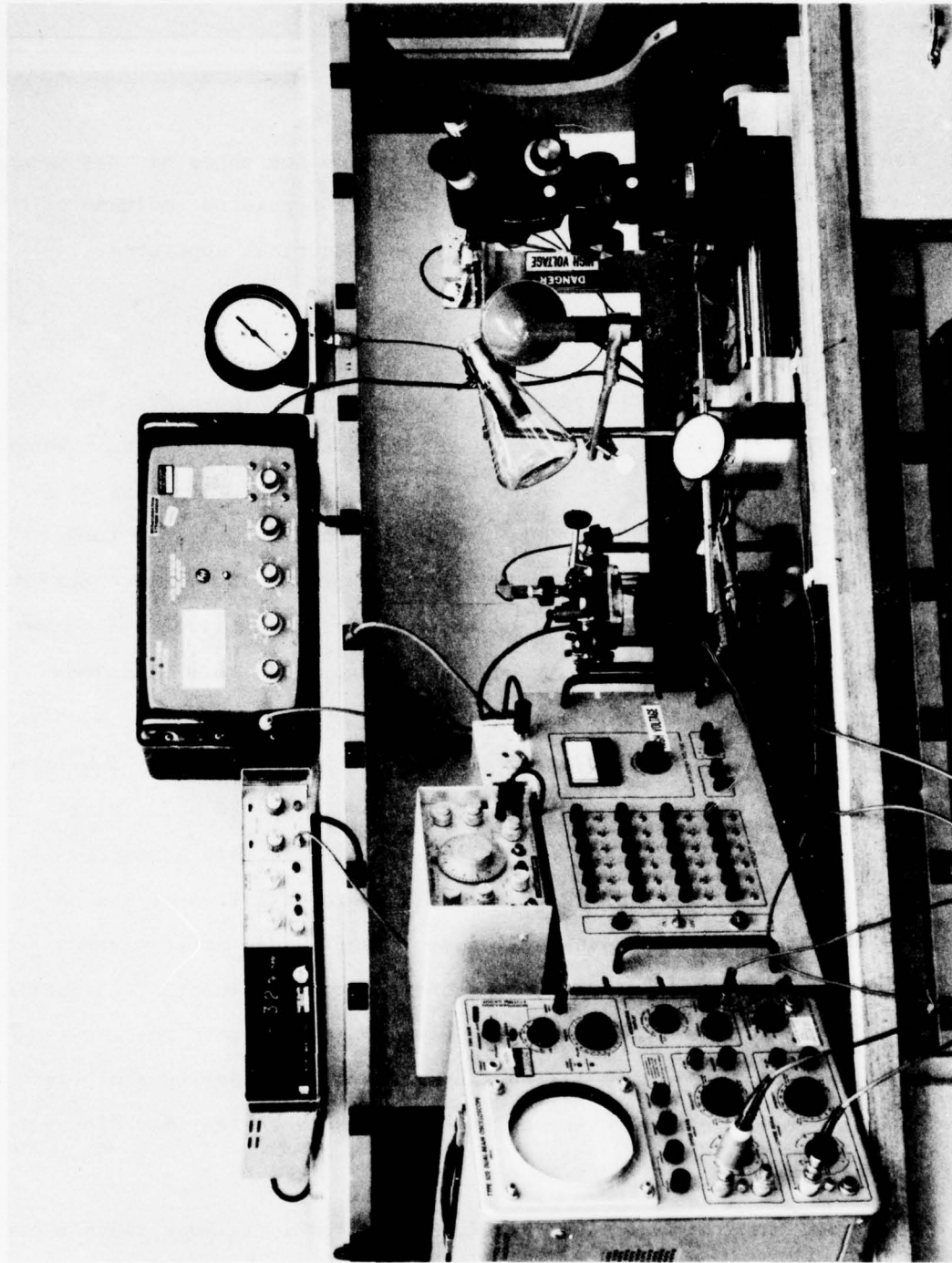
SA-2055-25

FIGURE 26   COMPUTER MODEL VERIFICATION TEST STATION

96

FIGURE 27   INK DELIVERY SYSTEM

found in the bottom of the reservoir. These deposits may have been in
part products of corrosion, since small pits were observed in the cover
plate where the anodized surface was disrupted.

To initiate flow, the shutoff valve on the nitrogen bottle was opened.
The ink valve on the reservoir was normally open. To stop flow, the nitro-
gen was shut off and reservoir pressure exhausted through the relief valve.
This arrangement was acceptable, but did not provide a quick start or stop
of ink flow, resulting in somewhat messy operation. This problem should
be remedied in real printing applications, such as by use of a quick-acting
solenoid valve near the print head.

It was necessary to change the disposable filter element after a few days of running. This need was indicated by a difference in the readings of the two pressure gauges.

The ink collected in the sump was normally reused, since it was filtered twice each time through the system. When the ink began to clog the filter more rapidly, it was discarded for fresh ink.

B.   Mechanical Hardware

The ink jet gun used is the A. B. Dick printing head (Part No. 338018), as specified in the contract. The printing head is mounted in an assembly corresponding to the drawings supplied by the client (No. ONO-71606). The assembly contains the deflecting plates, the ink gun, and a drain duct. The entire assembly is mounted on an elevated platform. During the experimental work, the drain duct was removed so that all the drops could be observed over a longer flight path.

A stereo microscope was mounted on a translating base near the printing head. The microscope could be moved parallel to the direction of the jet so that the field of view could follow the entire flight path. A zoom feature allowed study of drop formation and separation as well as overall flight observations. A dial indicator was used to read out microscope position, with resolution along the x-coordinate of 0.001 inch. A reticle in the microscope eyepiece was used to measure vertical drop displacements (y-coordinate); resolution again was 0.001 inch. The microscope translator and ink jet assembly were attached to a common base plate. A ringstand was used to support the ink sump and strobe lamp. The arrangement is visible in figure 26.

C.   Electrical Hardware

Figure 28 is a block diagram of the electrical circuitry used in the experimental work. A Wavetek signal generator provides a sine wave input

98

FIGURE 28   BLOCK DIAGRAM OF ELECTRICAL CIRCUITRY USED IN VERIFICATION OF COMPUTER MODEL

SA-2055-2R

99

at a selectable frequency. The Wavetek output goes to a waveform generator block and a crystal-phasing block. The wave form generator supplies a shaped signal at the driving frequency to the charging amplifier and also interacts with the crystal-phasing block.

The charging amplifier supplies the charging electrode with a sequence of 24 voltage pulses. Each pulse is used to charge a single drop. Each pulse can be individually set to a voltage level between 0 volts and about +400 volts; the pulse width is equal to the reciprocal of driving frequency. The charging signal is continuously repeated; after each group of 24 drops leaves the gun, the charging signal is started again.

The crystal-phasing block is an interface between the driving signal and the crystal power amplifer. It is necessary to hold the charging signal constant at the moment of drop separation; the crystal-phasing circuit makes this possible. Since it is difficult to predict when a drop will separate during each cycle of the crystal-driving signal, the crystal-phasing circuit provides for manual adjustment of the phase between the driving and charging signals.

The crystal power amplifier boosts the phase-adjusted sinusoidal crystal drive signal. This signal is amplified again by the auxilary power amplifier. The output of that unit is applied to the electrode between the piezoelectric crystals.

The waveform generator also provides an output to a strobe divider and a strobe delay circuit. These circuits deliver a trigger signal to a stroboscope. The divider circuit is necessary since the strobe cannot flash at the same frequency as drops are formed. For convenience in observations, the driving frequency is divided by an integral multiple of 24. (The integer multipliers, manually selected, are 4, 8, and 16.) This allows the groups of 24 drops each to be frozen in flight. The

100

strobe delay circuit allows manual adjustment of the time between drop formation and strobe trigger; this permits continuous observation of a drop through its flight path.

The deflection circuit is an adjustable high voltage power supply. The upper deflection plate is held at ground. The lower plate can be supplied with any potential between 0 and -10,000 volts.

Two modifications to the circuitry discussed in the Task 1 report were necessary. The first was a redesign of the charging amplifier circuit. It was found that the original circuit allowed undesirably long pulse rise times. The redesigned circuit will deliver a 400-volt pulse with 6 μs rise time at any driving frequency up to 100 kHz. The second modification was the use of the auxiliary power amplifier. The crystal power amplifier alone delivered a driving signal whose amplitude fell with increasing frequency. To test printer operation at high voltages and frequencies, the auxiliary amplifier was installed. This tube-type amplifier could deliver a 400-volt peak-to-peak sinusoidal signal at up to 65 kHz. Peak voltage fell slightly above that frequency.

With the exception of the Wavetek, auxiliary power amplifier, and stroboslave, the electrical apparatus of Figure 28 is contained in a single cabinet. The cabinet is visible in Figure 26. The front panel of the cabinet contains the following manual controls:

- Power On-Off switch.
- Potentiometers to adjust charging voltage for each of the 24 drops in a group.
- Switches to short charging voltage to ground for each of the 24 drops that is to be undeflected.
- Potentiometer adjustment and meter for deflecting voltage.
- Crystal power amplifier gain and phase adjustments.
- Strobe divider range selector (A, B, or C) and delay adjustment.

101

Less necessary controls are within the cabinet. Schematic diagrams of
the electrical hardware are contained in the Data Package. The electrical
hardware was essentially trouble-free, although fuses occasionally opened
if arcing or a short occurred. Arcing never caused failure of any electrical
components.

VII   RECOMMENDATIONS FOR SYSTEM OPERATION

During this contract effort and past projects, a good deal of experience with ink jet systems was obtained. This background has produced a number of observations related to the operation of ink jet printers. Although these are not directly related to the Analytical Computer Model, they will hopefully be useful to anyone using this technology.

Ink is driven through the orifice by pressure. In experimental apparatus at SRI, compressed nitrogen has been used as the pressure source. Some commercial equipment made by A. B. Dick Company uses a positive displacement pump instead. Each method has advantages and disadvantages. The gas source provides an even pressure with little chance for contaminating the ink, but gas bottles are bulky. Furthermore, gas pressurization is not compatible with a recirculating ink system. Pump pressure permits both recirculation and self-contained operation, but adds hardware to the ink delivery system. This can lead to ink contamination that will stress the filtering system. A choice between the two methods must be based on the particular system being considered.

The possibility of pressurized gas going into solution in the ink and then coming out when the ink leaves the orifice has been raised. If this occurs, unstable drop formation would be expected. If fact, drop formation at a fixed operating point is quite stable. Also, no effervescence has been observed in the ink within the clear glass reservoir when pressure is released. These facts seem to reject the possibility of ink "carbonation." It is conceivable, however, that some combinations of ink, gas, and pressure will indeed cause this undesirable effect.

In Section VI-A it was mentioned that experimental apparatus for this project provided relatively slow starting and stopping of ink flow.

103

A quick-acting valve near the printing head is much more desirable, since it can minimize the ink deposits on the charging electrode, deflection plate, and orifice. These deposits, if allowed to grow, can lead to arcing, altered fields, and poor jet formation.

Materials used in ink delivery systems should be carefully chosen. Since the inks must be conductive, they usually contain an acid or solvent component, making them likely to attack many materials. Thus inert materials are favored such as glass, passivated stainless steel, anodized aluminum, and a few plastics. Plastics should be tested in ink samples before their use in a system. Teflon is generally acceptable. Some corrosion of an anodized aluminum surface was noted where the surface had been damaged.

A puzzling problem developed involving a brass "T" in the ink line. A symptom of the problem was jitter of the drops under stroboscope illumination. The cause was found to be a galvanic cell set up between the brass piece and stainless parts, with ink as the electrolyte. Brass, being the cathode, was the site of gas bubble formation. The bubbles passing through the orifice caused the observed jitter. This example makes a case for using a single type of metal throughout the ink delivery system. Stainless steel is the most practical, since many purchasable items are available in this material.

Clogging of the orifice was occasionally observed, although usually after the ink line downstream of the second filter had been broken. It is also felt that some contaminants came from the ink pressure gauge. Clean, sealed systems ran quite regularly. It was also noticed that if the system were left alone for several days, with ink and air standing beyond the second filter, clogs were somewhat more likely on startup. These observations favor leaving clean, sealed systems intact, and suggest keeping the line to the orifice completely filled with ink or with air

104

when out of service. The relatively large orifices (~2.5- to 3-mil diameter) used in the A. B. Dick print heads were much more trouble-free than smaller (1.5-mil) orifices used previously at SRI.

Clearing a clogged filter usually meant breaking the line before the print head and back-flushing through the head. Several tries were sometimes needed. Reassembling the ink lines could then cause new problems since shavings can come off the inner walls of plastic tubing when they are pressed over metal tubes.

The ink collector shown in Figure 1 was seldom used, since the drops were usually observed over longer flight paths. When it was in place, it was found that ink splattered and frothed in the collector. This should be avoided; the stream should be slowed more gently. Splattering can lead to deposits on the deflection plates and evaporation of some ink components.

From observations related to drop charging, it was evident that small charging electrode spacing was desirable. Small spacing reduces the proportional effects of charge on preceding drops and increases the importance of the electrode itself. Small spacing also more effectively shields the charging region from the deflecting field. One drawback of small spacing is the increased difficulty in centering the jet. With large spacing, centering is less critical.

An alternative to the present U-shaped electrode would be a metal tube through which the jet passed. Although alignment would be difficult, this configuration would provide excellent capacitive coupling to the jet and shielding from the deflecting field. It would also be axisymmetrical, which the U-channel is not.

Deflecting plate angle and length provides room for trade-offs. If the angle is small, the field will be concentrated and deflection greater

105

than if the angle is large. However, the chance exists that with a small angle, deflected drops will strike the upper plate. Thus, large deflections require a relatively large angle, which in turn creates a weak downstream field. No case can be made for using longer plates, unless the flight path is quite long or very large deflections are needed. The reason for this is that downstream parts of the field have less time to influence drop deflection. When a drop nears the printing surface, even a strong acceleration will not be able to alter its trajectory by much. Thus, a general rule is that the strongest deflecting forces should be applied early in the flight. Once a significant y-velocity is reached, the deflecting field is less essential.

Trade-offs are also available regarding the selection of charging and deflecting voltages. Since deflecting force is roughly proportional to the product of these values, many combinations would result in the same deflection distance. Keeping drop charge low will reduce mutual repulsion forces and will have less tendency to affect jet breakup. Furthermore, the electrical problem of providing sharp charging signals is diminished if voltage levels are kept low. High charging voltages, on the other hand, will reduce the influences of stray fields and the charges on the preceding drops.

As mentioned earlier in this report, aerodynamic drag is the dominant force opposed to drop flight. The effects of drag are usually manifested in late arrival at the printing surface of drops with few or distant predecessors. This causes printing distortion. In the past, this problem has been eliminated by providing laminar air flow across the jet (in the ± z-direction) over most of the flight path. The effect of this air flow is apparently to blow the wake of each drop aside so that every drop sees the same aerodynamic environment independent of the position of its neighbors. The velocity of the air stream has been experimentally adjusted in past work at SRI, with values roughly 10 to 20 percent of the jet velocity.

106

Care must be taken to ensure that air flow past the jet is laminar. Turbulent flow can cause gross distortion.

In selecting an operating point for a printing application, several things must be considered. First, drop rate will be based on the desired number of drops per character and characters per second. At such a rate, ink supply pressure (and hence jet velocity) should be set so that disturbance wavelength ($\lambda = v_j/f$) is slightly greater than jet circumference (πd_j). With these general criteria, observations of drop formation at various crystal voltages should be made, with small adjustments of pressure and frequency permitted. A point should be chosen where the following criteria are met:

- Drop separation well within the charging electrode
- Drop formation with few or no satellites
- Stable drop formation with small shifts in voltage, pressure, or frequency.

The last point is quite important, since conditions were observed where small changes in the parameters would have a large effect on stream breakup. It should be noted that many acceptable operating points have been observed, but such conditions are often surrounded by unacceptable combinations of operating parameters.

edEDFILMED

VIII   RECOMMENDATIONS FOR FUTURE WORK

Work under this contract has naturally raised thoughts regarding further effort. Since study of nonimpact printing techniques in general and ink jet printing systems in particular will continue at SRI, these suggestions are presented here.

Most of the effort during this project went into creation of the Analytical Computer Model by studying the separate physical phenomena concerned. Comparisons between the overall model and experimental results were limited to a few test cases. The results indicate that the computer model is a functioning, useful tool of modest accuracy. At this point, it is recommended that more comparisons between overall computer predictions and experimental test cases be made. This type of work would require a lower rate of effort than in the project. Study of additional test cases would yield two results:

(1) The capabilities and shortcomings of the Analytical Computer Model in its present form could be better defined. A wide range of test conditions should be evaluated to note the situations in which intolerable inaccuracies result.

(2) By noting weak points in the computer model, further refinement could be accomplished, hopefully extending the usefulness of the program.

Given the familiarity with the existing program and the available experimental apparatus, this work is a natural extension of what has already been accomplished.

The second area in which SRI is qualified is that of applying ink jet printing technology for specific purposes. Designing systems to meet specific criteria is well within our capability; two such systems

109

have been designed at SRI for other clients. This background has been supplemented in the past year by four contracts (including this one) related to ink jet printing. These projects have covered all aspects of the subject, including analysis, construction of experimental hardware, and ink formulation.

SRI will be pleased to submit proposals covering any of the points mentioned above.

IX CONCLUSIONS

The Analytical Computer Model is a useful tool. Over the defined ranges of input conditions, the model predicts drop characteristics and behavior with modest accuracy. With some combinations of input conditions, the predictions are accurate within a few percent.

The computer model consists of an executive routine and 11 subroutines, each of which treats a different aspect of the ink jet printing process. The predictions of jet velocity and drop characteristics are in excellent agreement with observations. A method for accurately predicting drop separation point and quality of drop formation was not realized; fortunately, this has little effect on the rest of the program. The subroutines used to compute induced charge and forces on the drops in flight are generally accurate. Errors are primarily a result of the assumptions and idealizations that had to be made to permit analytical study. In most cases, the subroutines were refined on the basis of experimental observations.

The Analytical Computer Model in its present form should be quite useful for studying a wide variety of ink jet printer operating configurations. By simply giving the program a set of input conditions, a picture of expected performance is generated. In this way, the dependence of printer output on particular parameters can be observed. In many cases, this procedure will be more expedient than performing lengthy laboratory experiments. Optional program outputs can be used to indicate which forces on the drops are dominant and how they behave through flight.

The study on which the Analytical Computer Model is based has provided new insights into ink jet printing systems. The printer is seen

111

to be a complex physical device whose operation is dependent on numerous parameters.   The model will hopefully lead to a better understanding of the behavior of ink jet printers.

Appendix A

JETPER THEORY

Appendix A

JETPER THEORY

1. Results

This appendix gives the analytical background for deriving the following formula for the perturbation in jet velocity at the orifice:

Amplitude of initial velocity perturbation

$$= \left| \widetilde{u}_o \right| = a_F \left| \widetilde{u} \right| / C_c a_o \quad (m/sec)$$

where

$$\left| \widetilde{u} \right|^2 = \omega^2 L_c^2 (d_o/k_7)^2 (1 + w_5^2) / \left\{ (1 + w_8 \tan \Omega)^2 \right.$$

$$\left. + [w_5 + (w_5 w_8 + k_6) \tan \Omega]^2 \right\}.$$

2. Notation

The parameters and dimensionless ratio used in the analysis are listed below. These are derived from the physical apparatus and the imposed operating point. The variables of the theory, such as geometric coordinates, are defined where needed. Figure A-1 shows the idealized jet perturbation apparatus and some system parameters.

115
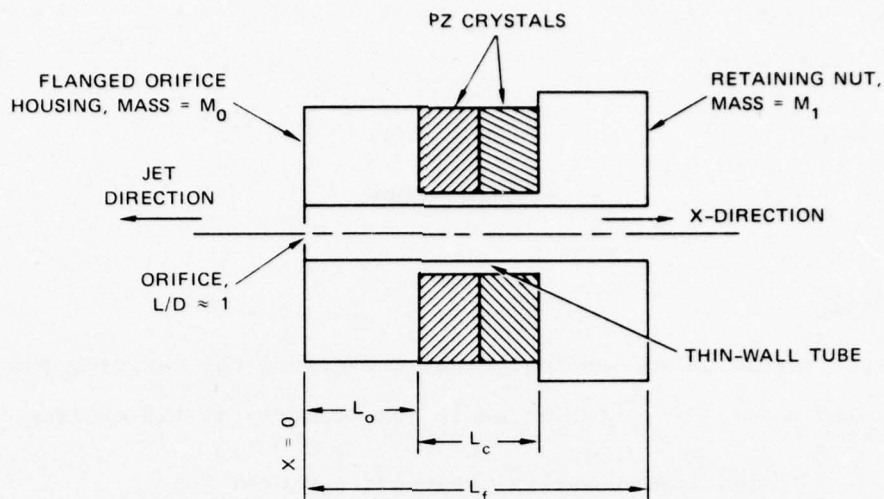
FIGURE A-1   IDEALIZED JET PERTURBATION APPARATUS

System Parameters

a_c axial cross-sectional area of crystal (m^2)

a_F axial cross-sectional area of fluid column (m^2)

a_o axial cross-sectional area of orifice (m^2)

r_o radius of orifice (m)

L_c length of crystal (m)

L_F length of fluid column (m)

L_{oo} length of orifice (m)

L_o distance from orifice to crystal (m)

M_o mass of orifice housing (kg)

M_1 mass of retaining nut (kg)

C_v orifice velocity coefficient (1)

f orifice friction factor (1)

C_c jet contraction coefficient (1)

u_1 mean flow velocity, upstream from orifice (m/sec)

ρ_1 steady flow density, upstream from orifice (kg/m^3)

p_1 steady flow pressure, upstream from orifice ($newton/m^2$)

116

c_1 steady flow sound speed, upstream from orifice (m/sec)

p_o atmospheric pressure (newton/m^2)

ω circular frequency (radian/sec)

A_v amplitude of applied potential (volts, zero-to-peak)

d piezoelectric constant (m/volt)

Y Young's modulus for crystal (newton/m^2)

K_T tube spring constant (newton/m)

ν kinematic ink viscosity (m^2/sec)

Dimensionless Ratios

$$\Omega = \omega L_F \dot{c}_1 / (c_1^2 - u_1^2)$$

$$M_c = u_1/c_1$$

$$d_o = 2dA_v/L_c$$

$$k_m = M_o/M_1$$

$$k_\omega = \omega^2 L_c M_o/Ya_c$$

$$k_t = K_T L_c/Ya_c$$

$$k_3 = (a_F/r_o) \left[(L_{oo}/a_o) + (2/\pi a_F C_v)^{1/2} \right]$$

$$k_4 = (1/2 \, C_v^2) + f \, L_{oo} \, a_F^2 / 4r_o a_o^2$$

$$k_5 = k_3/2 \, M_c k_4$$

$$k_6 = (1 - M_c^2 k_4)/2 \, M_c k_4$$

$$k_7 = k_\omega - (1 + k_t)(1 + k_m)$$

$$k_8 = (a_F \rho_1 c_1^2 / Ya_c) \left[1 - (1 + k_t)k_m/k_\omega \right]$$

$$w_5 = \omega k_5 \, r_o/c_1$$

$$w_8 = \omega L_c \, k_8/k_7 c_1$$

117

Solution of the jet perturbation problem required analysis of the fluid column, imposed boundary conditions, and orifice motion.

3. Fluid Column

The equations of one-dimensional flow of a viscous, compressible, barotropic fluid read

$$\rho_t + (\rho u)_x = 0$$

$$u_t + u u_x + (1/\rho)\rho_x = (4/3)\nu u_{xx}$$

$$dp = c^2 d\rho \quad,$$

where x is the distance coordinate down the column, t the time, ν the kinematic viscosity, and variable subscripts denote partial differentiation. The flow velocity u is a sum of the steady velocity u_1 and the perturbation $\tilde{u}$. In a similar notation for the other flow variables, linearized equations for the perturbations read

$$\tilde{\rho}_t + \rho_1 \tilde{u}_x + u_1 \tilde{\rho}_x = 0$$

$$\tilde{u}_t + u_1 \tilde{u}_x + (1/\rho_1)\tilde{\rho}_x = (4/3)\nu \tilde{u}_{xx}$$

$$\tilde{p} = c_1^2 \tilde{\rho} \quad.$$

Oscillations at frequency ω correspond to solutions with $\tilde{u}$ a sum of constant multiples of

$$e^{i\omega(t-\lambda x)} \qquad \text{or} \qquad e^{-i\omega(t-\lambda x)} \quad,$$

where λ is a constant and $i = \sqrt{-1}$. For one such term, set

$$\tilde{u} = u_o e^{\pm i\omega(t-\lambda x)} \quad.$$

118

Then

$$\widetilde{p} = p_o \, e^{\pm i\omega(t-\lambda x)}$$

$$\widetilde{\rho} = \rho_o \, e^{\pm i\omega(t-\lambda x)} \quad ,$$

and substitution in the equations gives

$$\rho_o = \rho_1 \, u_o \lambda / (1 - u_1\lambda) \ ,$$

$$p_o = c_1^2 \, \rho_o \ ,$$

u_o is arbitrary, and λ is a root of

$$\lambda^2(u_1^2 - c_1^2) - 2u_1\lambda + 1 - (4/3)\nu(\pm i\omega)\lambda^2(1 - \lambda u_1) \quad .$$

In the absence of viscosity,

$$\lambda = 1/(u_1 \pm c_1) \quad .$$

For small viscosity, λ changes to

$$\lambda = [1/(u_1 \pm c_1)][1 - (2/3)\nu(\pm i\omega)/(u_1 \pm c_1)^2] \quad .$$

For a typical ink and operating point, ν is approximately 10^{-2} cm^2/sec, c_1 is 1.5×10^5 cm/sec, and u_1 is negligibly smaller than c_1. At a frequency of 40 KHz, one finds $\omega = 2.5 \times 10^5$ (sec^{-1}) so that

$$(2/3) \, \nu \, \omega/c_1^2 \approx 7 \times 10^{-8} \quad .$$

Therefore, the assumption of small viscosity is justified and, since this term is subtracted from 1, the influence of viscosity on λ and the remainder of the computation is negligible.

The one-dimensional, inviscid velocity oscillation of the fluid column is given by

119

$$\tilde{u} = c_1 \left\{ U_0 \, e^{i\omega[t-x/(u_1-c_1)]} + U_1 \, e^{i\omega[t-x/(u_1+c_1)]} \right.$$

$$\left. + U_2 \, e^{-i\omega[t-x/(u_1-c_1)]} + U_3 \, e^{-i\omega[t-x/(u_1+c_1)]} \right\} \quad ,$$

where U_0, U_1, U_2, and U_3 are as yet undetermined constants. The pressure and density variations are

$$\tilde{p} = \rho_1 c_1^2 \left\{ -U_0 e + U_1 e - U_2 e + U_3 e \right\}$$

$$\tilde{\rho} = \tilde{p}/c_1^2 \quad ,$$

where the exponent on e in the term $U_j e$ is the same as it is in the $\tilde{u}$ expansion.

4. Boundary Conditions

Constants U_j are determined by the boundary conditions at the two ends of the fluid column. At the upstream end of the column, $x = L_F$, and the perturbation in pressure is zero. It follows that coefficients of $\exp(i\omega t)$ and of $\exp(-i\omega t)$ are separately zero so that two equations are obtained:

$$U_0 e^{-i\omega L_F/(u_1-c_1)} = U_1 e^{-i\omega L_F/(u_1+c_1)}$$

$$U_2 e^{i\omega L_F/(u_1-c_1)} = U_3 e^{i\omega L_F/(u_1+c_1)} \quad .$$

At the downstream end of the column, $x = 0$, and the dynamic orifice condition[2] reads

$$p_1 + \tilde{p} - p_o = (\rho_1 + \tilde{\rho}) \left\{ \left[(2/\pi a_F C_v)^{1/2} + (L_{oo}/a_o) \right] \dot{q} \right.$$

$$\left. + \left[(1/2a_F^2 C_v^2) + (fL_{oo}/4r_o a_o^2) \right] q^2 \right\}$$

120

where

$$q = -a_F(u_1 + \tilde{u} - \dot{x}_o) \quad ,$$

x_o is the orifice displacement, and the dot indicates the time derivative. After subtracting off the steady-state relation

$$p_1 - p_o = \rho_1 k_4 u_1^2$$

the linearized remainder may be written

$$\lfloor(\tilde{u} - \dot{x}_o)/c_1\rfloor + \lfloor k_5(\dot{\tilde{u}} - \ddot{x}_o)r_o/c_1^2\rfloor + (k_6\tilde{p}/\rho_1 c_1^2) = 0 \quad .$$

This condition becomes useful when $x_o(t)$ is found.

5. Orifice Motion

Equations of motion for the masses M_o and M_1 and the stress-strain relation for the piezoelectric crystal are

$$M_1\ddot{x}_1 = -\sigma a_c - K_T(x_1 - x_o - L_c)$$

$$M_o\ddot{x}_o = \sigma a_c + K_T(x_1 - x_o - L_c) - \tilde{p}a_F$$

$$(x_1 - x_o - L_c)/L_c = \sigma/Y + d_o \cos \omega t \quad ,$$

where σ is the stress in the crystal, assumed to be uniform, and x_1 is the displacement of the retaining nut, mass M_1. The applied alternating potential is represented by the term $d_o \cos \omega t$.

Eliminating x_1 and σ gives

$$(M_1 k_m/Ya_c)\ddddot{x}_o + \lfloor(1 + k_t)(1 + k_m)/L_c\rfloor\ddot{x}_o + (a_F/Ya_c)\ddot{\tilde{p}}$$

$$+ \lfloor(1 + k_t)/M_1 L_c\rfloor a_F\tilde{p} = d_o \omega^2 \cos \omega t \quad .$$

121

Since, at $x = 0$,

$$\widetilde{p} = \rho_1 c_1^2 \left[(U_1 - U_0) e^{i\omega t} + (U_3 - U_2) e^{-i\omega t} \right] ,$$

one may solve for x_o to find

$$x_o = (L_c/k_7) \left\{ \left[(d_o/2) + k_8 (U_1 - U_0) \right] e^{i\omega t} \right.$$

$$\left. + \left[(d_o/2) + k_8 (U_3 - U_2) \right] e^{-i\omega t} \right\} \quad .$$

6. Solution

Substitution of x_o, $\widetilde{p}$, and $\widetilde{u}$ into the orifice boundary condition gives two more equations connecting the U_j. Solving the equations gives

$$U_1 = U_o \exp(2i\Omega)$$

$$U_2 = \bar{U}_o$$

$$U_3 = \bar{U}_1 \quad ,$$

where the bar denotes the complex conjugate operation and

$$U_o = (i\omega L_c d_o/4k_7 c_1)(1 + i\omega k_5 r_o/c_1) e^{-i\Omega} \Big/$$

$$\left\{ (1 + i\omega k_5 r_o/c_1)[\cos \Omega + (\omega L_c k_8/k_7 c_1)\sin \Omega] + ik_6 \sin \Omega \right\} .$$

It follows that, at $x = 0$,

$$\widetilde{u} = \text{Re } c_1(U_o + U_1) e^{i\omega t}$$

$$= 4 c_1 \text{ Re } U_o \cos \Omega \, e^{i(\Omega + \omega t)}$$

so that

$$|\widetilde{u}| = 4 c_1 |U_o \cos \Omega| \quad .$$

122

Taking the absolute value of the complex quantity gives the formula presented at the beginning of this appendix.

To realize a numerical solution, several measurements of the physical apparatus were required. These included taking dimensions and weighing the printing head components. The stiffness of the thin-wall tube connecting the flange and nut masses was calculated based on tube dimensions and material properties. Properties of the piezoelectric crystal material (PZT-4) were obtained from the manufacturer's data. The orifice friction factor was derived from the velocity coefficient value found in ORIFIC subroutine. The numerical values for the experimental printing head used in this project can be found within the listing of subroutine JETPER.

Appendix B

SEDPIS THEORY

Appendix B

SEPDIS THEORY

1. Results

On the basis of linearized theory, the oscillation at the orifice with velocity amplitude $|\tilde{u}_o|$ computed in JETPER grows to form separate drops at distance x along the jet path where

$$x = (r_j/b) \text{ arc sinh } (B \ u_J/|\tilde{u}_o|) \ ,$$

$$b = \text{Im } \alpha \ ,$$

$$B = \text{Im}(\alpha - w)/I_1(\alpha) \ .$$

and α is a particular root of

$$(\alpha - w)^2 = T \ f(\alpha)$$

$$f(\alpha) = \alpha(\alpha^2 - 1) \ I_1(\alpha)/I_o(\alpha) \ .$$

Jet growth and SEPDIS coordinates are shown in Figure B-1.

In the above expressions, r_J and u_J are the steady jet radius and velocity, I_o and I_1 are the modified Bessel functions, and frequency parameter w and surface tension parameter T are defined by

$$w = \omega r_J/u_J$$

$$T = T_1/\rho u_J^2 \ r_J \ ,$$

where ω (radian/sec) is the circular frequency of the applied oscillation, ρ (kg/m^3) the ink density, and T_1 (newton/m) the ink surface tension.

127
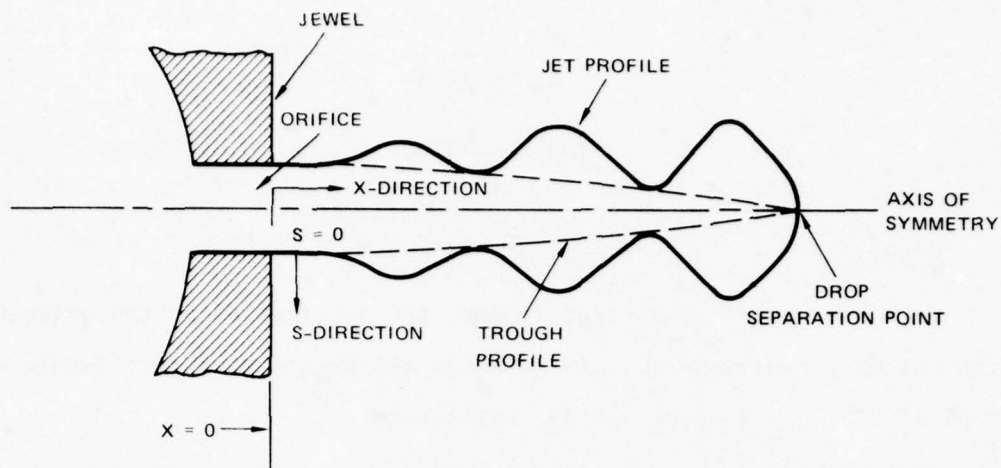
SA-2055-22

FIGURE B-1   JET PROFILE AND COORDINATE SYSTEM FOR SEPDIS SUBROUTINE

Finding the roots α in general is difficult. However, the limiting case with T being small and $0 < w < 1$ does apply to the ink jet and gives the approximate formulas:

$$b = \left[-T\ f(w) \right]^{1/2} \quad ,$$

$$B = b/I_1(w) \quad ,$$

where $f(w)$ is evaluated in the same way as $f(\alpha)$ above. These formulas are valid if $0 < w < 1$ and

$$T \ll 2w / \left| f'(w) \right| \quad ,$$

where

$$f'(\alpha) = \alpha \left\{ (\alpha^2 - 1) \left[1 - I_1^2(\alpha)/I_0^2(\alpha) \right] + 2\alpha\ I_1(\alpha)/I_0(\alpha) \right\} \quad .$$

2.   Perturbed Jet Flow

Since the pressure in the free jet does not vary appreciably from that of the atmosphere, the compressibility of the ink may be neglected. Assuming the flow to be irrotational implies the existence of a potential

128

function F that is a solution of Laplace's equation. For a cylindrically symmetric flow that is considered to be a sum of standing waves, F is a sum of terms of the form

$$F = (r_J |\widetilde{u}_o|/\alpha) \; I_o(\alpha r/r_J) \left(A e^{i\alpha x/r_J} + B e^{-i\alpha x/r_J} \right) \; ,$$

where α is a constant and A and B are functions of time.

If s is the perturbation in jet radius, the kinematic condition that the time rate of change of s following a fluid particle in the jet surface equals the radial component of the perturbation velocity reads in linear approximation

$$s_t + u_J s_x = F_r \; , \qquad \text{on } r = r_J \; .$$

This implies that the term for s corresponding to the standing wave above is

$$s = (r_J |\widetilde{u}_o|/u_J) \; I_1(\alpha) \left(C e^{i\alpha x/r_J} + D e^{-i\alpha x/r_J} \right)$$

where C and D are functions of time and are related to A and B by

$$A = w \, C' + i\alpha C \; ,$$

$$B = w \, D' - i\alpha D \; .$$

The prime indicates differentiation with respect to the dimensionless variable (ωt).

The balance of forces at the jet surface reads[a] in linear approximation

$$\rho (F_t + u_J F_x) - T_1 (s_{xx} + s/r_J^2) = 0 \qquad \text{on } r = r_J \; .$$

Substitution of the previously given expressions for F and s and simplification give

129

$$w^2 C'' + 2i\alpha w C' - \alpha^2 C + T\,f(\alpha)C = 0$$

$$w^2 D'' - 2i\alpha w D' - \alpha^2 D + T\,f(\alpha)D = 0 \quad,$$

where function f is as defined in the previous section.

Solving these equations and substituting into the forms for F and s gives

$$F = (r_J|\widetilde{u}_o|/\alpha)\,I_o(\alpha r/r_J)(-Tf)^{1/2}$$

$$\cdot\left[e^{i\alpha x/r_J}\!\left(C_1 e^{-itm_-} - C_2 e^{-itm_+}\right) + e^{-i\alpha x/r_J}\!\left(D_1 e^{itm_-} - D_2 e^{itm_+}\right)\right]$$

$$s = (r_J|\widetilde{u}_o|/u_J)\,I_1(\alpha)\left[e^{i\alpha x/r_J}\!\left(C_1 e^{-itm_-} + C_2 e^{-itm_+}\right)\right.$$

$$\left. + e^{-i\alpha x/r_J}\!\left(D_1 e^{itm_-} + D_2 e^{itm_+}\right)\right]$$

$$m_\pm = (u_J/r_J)\left[\alpha \pm (Tf)^{1/2}\right] \quad,$$

where C_1, C_2, D_1, and D_2 are constants to be determined.

Since $f(\alpha)$ is an even function of α, changing the sign of α merely interchanges the roles of C and D. Therefore, one may restrict consideration to one-half the complex α plane, here taken to be Re $\alpha \geq 0$.

Since $(Tf)^{1/2}$ appears with both signs, it is necessary only to work with a particular definition of this square root. Branch points for the root occur at zeros and poles of f. These are found on the imaginary axis, Re $\alpha = 0$, and also on the real axis at $\alpha = \pm 1$. If cuts from the branch points are all taken as running to the left, the right half α plane, except for the segment $0 < \alpha < 1$ of the real α axis, is a region in which $(Tf)^{1/2}$ is continuous and has real and imaginary parts whose signs agree with those of the real and imaginary parts of α.

130

The expressions for F and s above are now unambiguously defined. Also consideration may be restricted to values of α with Re $\alpha \geq 0$.

3. Frequency Condition

Since the perturbation is a steady oscillation at circular frequency ω,

$$m_{\pm} = \pm \omega \; ,$$

where all four choices of the ambiguous signs are permitted. Rearranging and squaring reduces this to the pair of equations for α,

$$(\alpha \pm w)^2 = T \; f(\alpha) \; .$$

Since f is a real function of α, roots of each of these equations occur in complex conjugate pairs. Therefore, consideration can be restricted further to the first quadrant of the complex α plane where Re $\alpha \geq 0$ and Im $\alpha \geq 0$.

4. Outgoing Waves

Since function f contains Bessel functions, there are many roots α to the frequency equation. The physically meaningful ones represent outgoing waves (traveling in the jet direction). One may first consider the case of negligible surface tension, where the outgoing waves are readily identified.

After clearing fractions and setting T to zero one obtains the simplified frequency equation

$$(\alpha \pm w)^2 \; I_o(\alpha) = 0 \; .$$

Roots of this equation in the first quadrant of the complex α plane are $\alpha = w$ and $\alpha = i k_n$ $(n = 1, 2, 3, \ldots)$ where k_n is the n-th (real) root of the unmodified Bessel function J_o. In the absence of surface tension, there

131

is no mechanism for maintaining pressure variations in the jet far from the orifice. Hence the perturbations cannot grow as x becomes large. Each imaginary root, $\alpha = ik_n$, contributes an exponentially growing or decaying factor depending on the sign with which it is used. A growing factor is not part of an outgoing wave, while a decaying one does not contribute to the instability that gives eventual breakup of the jet into drops. Hence the real root $\alpha = w$ is the only useful one in the case of negligible surface tension. For positive T (nonnegligible surface tension), the meaningful roots are real ones or ones arising from real ones as T increases from zero.

In Figure B-2, function $f(\alpha)$ is sketched for real α as are the parabolas $(\alpha \pm w)^2$ for a value of w on $0 < w < 1$. One sees that the root $\alpha = w$ for $T = 0$ is a double root that splits into a pair of complex conjugate roots as T increases. Since f is proportional to α^3 for large α,
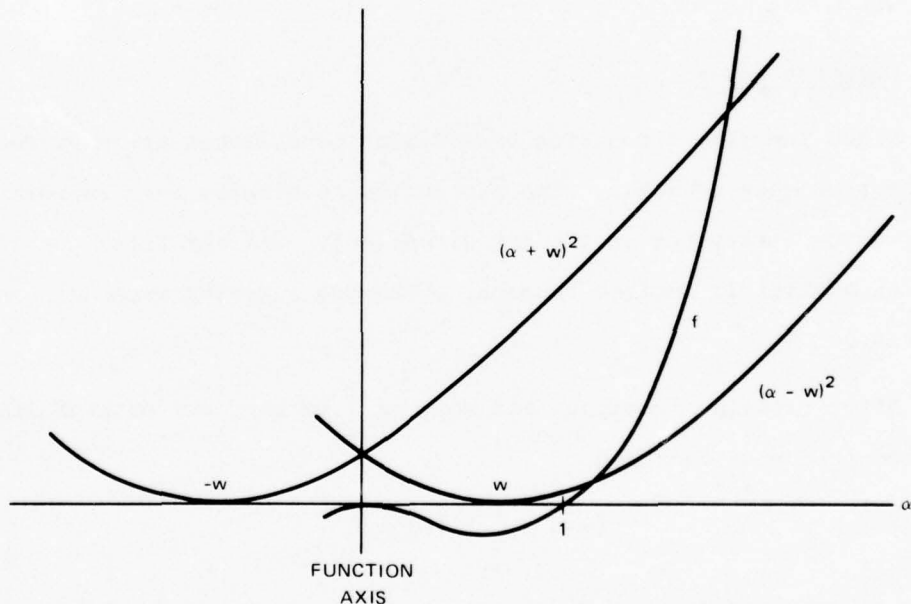
SA-2055-23

FIGURE B-2   FUNCTION f IN THE FREQUENCY EQUATION VERSUS REAL α

132

there are two further real roots, one on each parabola, that are large when T is small and remain real as T increases. The instability due to surface tension is shown by the complex roots arising from $\alpha = w$. A Taylor expansion of the frequency equation about $\alpha = w$ shows that

$$\alpha = w + i \left[-Tf(w)\right]^{1/2} .$$

This is the two-term result quoted above. It is a valid approximation if T is negligibly small with respect to $2w/\left|f'(w)\right|$, which is the case in all operating conditions that were examined.

If $1 < w$, the double root at $\alpha = w$ for $T = 0$ splits into two real roots as T increases. One of these remains between w and 1, while the other moves out toward increasing α to meet the decreasing large real root. As T increases further, the two roots come together to form a double root, say $\alpha = \alpha^*(w)$ at $T = T^*(w)$. Then for $T > T^*$ a pair of conjugate complex roots arise indicating the instability being sought. This implies that under certain conditions, an unstable region for $w \leq 1$ is followed by a stable region and then by a second unstable region as w grows larger than 1 (see Fig. 8, Section III-D-4).

Since the curves for $(\alpha - w)^2$ and $Tf(\alpha)$ are tangent at $\alpha = \alpha^*$, $T = T^*$, these values are found by solving

$$(\alpha^* - w)^2 = T^*f(\alpha^*)$$

$$2(\alpha^* - w) = T^*f'(\alpha^*) .$$

One finds for very large w,

$$\alpha^* \approx 3w - 1/3, \quad T^* \approx (4/27w)(1 + 6/w), \quad 1 \ll w ,$$

while for w near 1, there are the two solutions:

$$\alpha^* = 1.84, \quad T^* = 2.40, \qquad w = 1$$

$$\alpha^* \approx 2 - w, \quad T^* \approx 4.48(1 - w), \qquad w \approx 1$$

133

The stability boundary $T = T^*(w)$ is sketched in the (w,T) parameter plane in Figure 8.

5. Orifice Conditions

Consideration of the signs shows that the complex root α in the first quadrant is the solution to the equation

$$m_- = +\omega \ .$$

Hence constants C_2 and D_2 are set to zero in the solution formulas given above. Along with α, in the half plane $\mathrm{Re}\ \alpha \geq 0$, is the root $\bar{\alpha}$. Adding to the solutions terms for $\bar{\alpha}$ with coefficients C_3 and D_3 gives the general forms

$$F = (r_J |\widetilde{u}_o|/\alpha)\ I_o(\alpha r/r_J)(-Tf)^{1/2} \left(C_1 e^{i\alpha x/r_J - i\omega t} + D_1 e^{-i\alpha x/r_J + i\omega t} \right)$$

$$+ (r_J |\widetilde{u}_o|/\bar{\alpha})\ I_o(\bar{\alpha} r/r_J)(-\bar{T}f)^{1/2} \left(C_3 e^{i\bar{\alpha} x/r_J - i\omega t} + D_3 e^{-i\bar{\alpha} x/r_J + i\omega t} \right),$$

$$s = (r_J |\widetilde{u}_o|/u_J) \left[I_1(\alpha) \left(C_1 e^{i\alpha x/r_J - i\omega t} + D_1 e^{-i\alpha x/r_J + i\omega t} \right) \right.$$

$$\left. + I_1(\bar{\alpha}) \left(C_3 e^{i\bar{\alpha} x/r_J - i\omega t} + D_3 e^{-i\bar{\alpha} x/r_J + i\omega t} \right) \right] \ .$$

One boundary condition at the orifice is that the radius of the jet has its unperturbed value. To have $s = 0$ at $x = 0$, one sets

$$C_1 I_1(\alpha) + C_3 I_1(\bar{\alpha}) = D_1 I_1(\alpha) + D_3 I_1(\bar{\alpha}) = 0 \ \ .$$

The other orifice boundary condition is that the axial velocity component has a known perturbation on the axis of symmetry:

$$F_x = |\widetilde{u}_o| \sin \omega t \quad \text{at } r = x = 0 \ .$$

134

From this,

$$2i[C_1(\alpha - w) + C_3(\bar{\alpha} - w)] = 1$$

$$2i[D_1(\alpha - w) + D_3(\bar{\alpha} - w)] = 1 \quad .$$

Solution of the four equations gives

$$D_1 = C_1 \quad , \quad D_3 = C_3 = -C_1 I_1(\alpha)/I_1(\bar{\alpha}) \quad ,$$

$$C_1 = I_1(\bar{\alpha})/(2i)[(\alpha - w)I_1(\bar{\alpha}) - (\bar{\alpha} - w)I_1(\alpha)]$$

so that

$$s = (r_J|\tilde{u}_o|/u_J B) \sin[(\alpha - \bar{\alpha})x/2r_J] \sin[(\alpha + \bar{\alpha})x/2r_J - \omega t] \quad ,$$

where

$$B = Im[(\alpha - w)/I_1(\alpha)] \quad .$$

6. Drop Separation

Drop separation occurs at the smallest value of x for which $(r_J + s)$ can be zero for some t. This condition is equivalent to finding the smallest x such that

$$\left(|\tilde{u}_o|/u_J B\right) \sin(ibx/r_J) = 1 \quad , \quad b = Im\alpha \quad .$$

One obtains

$$x = (r_J/b) \text{ arc sinh} \left(Bu_J/|\tilde{u}_o|\right) \quad .$$

135

Appendix C

CHARGE THEORY

Appendix C

CHARGE THEORY

This appendix describes the derivation of the drop charging equation used in the model and gives the functional forms of the factors F_1 and F_2.

Figure C-1 shows the electrode configuration just as the i-th drop is breaking off. The free drops, the jet, and the charging electrode are conductive bodies acting as electrodes. The i-th drop is being
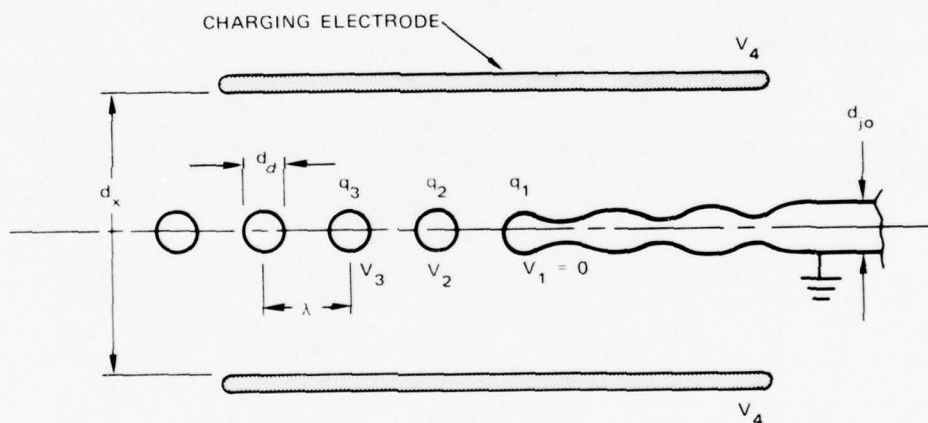

SA-2055-33

FIGURE C-1   ELECTRODE ARRANGEMENT FOR DROP CHARGING

charged to q_1 by a potential V_4 on the charging electrode plates. Two previously charged drops with charges q_2 and q_3 are also present and are at potentials V_2 and V_3, respectively. The charge on any drop may be written in terms of the potentials V_i and coefficient c_{ij} such that

$$q_j = \sum_{i=1}^{4} c_{ij} V_i \quad .$$

The coefficients c_{ii} are called the coefficients of self-capacitance and are the ratio of the charge on the electrode i to its potential when all other conductors are grounded. The c_{ij}, $i \neq j$, are the coefficients of inductive capacitance and are the ratios of the charge on conductor j to the potential on conductor i, with all other conductors being grounded. Other important properties of the coefficients are that $c_{ii} \geq 0$ and $c_{ij} \leq 0$, $i \neq j$, and $c_{ij} = c_{ji}$.

Known quantities are V_1, V_4, q_2, and q_3. It is desired to find q_1 in terms of these quantities and the coefficients c_{ij}. In the process it is also necessary to find V_2 and V_3, at least implicitly. To solve for the three unknowns requires the three equations

$$q_1 = c_{11} V_1 + c_{21} V_2 + c_{31} V_3 + c_{41} V_4$$

$$q_2 = c_{12} V_1 + c_{22} V_2 + c_{32} V_3 + c_{42} V_4$$

$$q_3 = c_{13} V_1 + c_{23} V_2 + c_{33} V_3 + c_{43} V_4 \quad .$$

Note that since the continuous portion of the jet is grounded, $V_1 = 0$. If the approximation is made that the drop being formed is a sphere, then from the symmetry of the configuration the following simplifications can be made:

140

$$c_{11} = c_{22} = c_{33}$$

$$c_{41} = c_{42} = c_{43}$$

$$c_{32} = c_{23} = c_{21} = c_{12} \quad .$$

The second two equations may be solved for V_2 and V_3 and then substituted into the first equation giving

$$q_1 = c_{41}V_4 + c_{21}\left[\frac{(c_{11} - c_{31})q_2}{(c_{11}^2 - c_{21}^2)} - \frac{c_{41}}{(c_{11}^2 - c_{21}^2)}V_4\right]$$

$$+ c_{31}\left[\frac{q_3}{(c_{11} + c_{21})} - \frac{c_{41}}{(c_{11} + c_{21})}V_4\right] \quad .$$

From experiments it is known that

$$c_{11} \approx 10\,c_{21} \quad \text{and} \quad c_{11} \approx 20\,c_{31} \quad ,$$

so that to a good approximation

$$(c_{11} - c_{31}) \approx c_{11} \quad , \quad (c_{11} + c_{31}) \approx c_{11}$$

$$(c_{11}^2 - c_{21}^2) \approx c_{11}^2 \quad , \quad (c_{11} + c_{21}) \approx c_{11} \quad .$$

141

The equation for q_1 thus simplifies to

$$q_1 \approx c_{41}V_4 + c_{21}\left[\frac{q_2}{c_{11}} - \frac{c_{41}}{c_{11}}V_4\right] + c_{31}\left[\frac{q_3}{c_{11}} - \frac{c_{41}}{c_{11}}V_4\right] \quad .$$

The factors F_1 and F_2 are defined by

$$F_1 = -\frac{c_{21}}{c_{11}}$$

$$F_2 = -\frac{c_{31}}{c_{11}} \quad ,$$

so that

$$q_1 = c_{41}V_4 - F_1(q_2 - c_{41}V_4) - F_2(q_3 - c_{41}V_4) \quad .$$

This equation may be rearranged to give

$$q_1 = c_{41}V_4(1 + F_1 + F_2) - F_1 q_2 - F_2 q_3 \quad .$$

Since c_{41} is negative, the charging capacitance, C, is defined as

$$C = -c_{41} \quad .$$

142

This yields the equation

$$q_i = -CV_i - F_1(q_{i-1} + CV_i) - F_2(q_{i-2} + CV_i) \quad .$$

Rearranged, this equation is the one used in CHARGE subroutine:

$$q_i = -CV_i(1 + F_1 + F_2) - F_1q_{i-1} - F_2q_{i-2} \quad .$$

In steady-state operation, $q_1 = q_2 = q_3$, so that

$$q_1(1 + F_1 + F_2) = c_{41}V_4(1 + F_1 + F_2) \quad ,$$

or $q_1 = c_{41}V_4$. This result is the same as Sweet's model.[4] The fact that c_{41} is negative indicates that the charge induced is of opposite polarity to the charging voltage. This also implies that $V_2 = V_3 = 0$ and explains why Sweet's model is accurate for steady-state operation.

The functional forms for c_{11}, c_{21}, and c_{31} were obtained from known solutions to Laplace's equation for simple electrode configurations. To calculate c_{21} and c_{31}, the electrode configuration was assumed to be two spheres of equal radius a and their centers separated by a distance d. The inductive capacitance for this configuration is

$$c_{k1} = -4\pi\epsilon a \, \sinh\beta_k \sum_{n=1}^{\infty} \text{csch}(2n\beta_k) \quad k = 1,2 \quad ,$$

where $\beta_k = \cosh^{-1}(d/2a)$. For both c_{21} and c_{31}, $a = d_d/2$; for c_{21}, $\beta_1 = \cosh^{-1}(\lambda/d)$; for c_{31}, $\beta_2 = \cosh^{-1}(2\lambda/d_d)$. ϵ is the permitivity of

143

free space, d_d is the drop diameter, and λ is the drop spacing. To obtain six place computational accuracy the summation needs to be carried out to only six terms.

The capacitive model for c_{11} was taken to be a cylinder of length b and diameter b centered between two plane infinite conductors separated by a distance f. The functional form for c_{11} is then

$$c_{11} = 2\pi\epsilon b \ln(4f/\pi b) \quad .$$

Since $b = d_d$ and $f = d_x$,

$$c_{11} = 2\pi\epsilon d_d \ln(4d_x/\pi d_d) \quad .$$

The ratio of c_{k1} to c_{11} is then

$$\frac{c_{k1}}{c_{11}} = -\frac{\sinh \beta_k \sum\limits_{n=1}^{6} \operatorname{csch}(2n\beta_k)}{\ln(4d_x/\pi d_d)} \quad .$$

To experimentally verify that the above ratio is sufficiently accurate as a model, an observable quantity was needed. If the variables q_1, q_2, q_3, and V_4 in the charging equation are subscripted as events in time such that the i-th drop is the drop currently being charged by charging voltage V_i, then the equation may be written

$$q_i = c_{41}V_i\left(1 - \frac{c_{21}}{c_{11}} - \frac{c_{31}}{c_{11}}\right) + \frac{c_{21}}{c_{11}}q_{i-1} + \frac{c_{31}}{c_{11}}q_{i-2} \quad .$$

144

Let all drops up to the (i-1)-th be uncharged, and the (i-1) charged by a potential V_{i-1}. To measure the magnitude of the charge that the (i-1)-th drop inducts on the i-th drop, it is necessary to observe how much the i-th drop is deflected and to apply a charging potential V_i to it so that its net charge is zero and it therefore experiences no deflection. Consequently, the conditions are that $q_{i-2} = q_i = 0$, giving

$$\frac{c_{21}}{c_{11}} q_{i-1} = - c_{41} V_i (1 - \frac{c_{21}}{c_{11}} - \frac{c_{31}}{c_{11}}) \quad .$$

The (i-1)-th drop was formed under the conditions

$$q_{i-2} = q_{i-3} = 0$$

or

$$q_{i-1} = c_{41} V_{i-1} (1 - \frac{c_{21}}{c_{11}} - \frac{c_{31}}{c_{11}})$$

which, when substituted into the other equation, gives

$$\frac{c_{21}}{c_{11}} c_{41} V_{i-1} (1 - \frac{c_{21}}{c_{11}} - \frac{c_{31}}{c_{11}}) = - c_{41} V_i (1 - \frac{c_{21}}{c_{11}} - \frac{c_{31}}{c_{11}})$$

or

$$\frac{V_i}{V_{i-1}} = - \frac{c_{21}}{c_{11}} \quad .$$

145

Thus, by measuring the two charging voltages when the deflection of the i-th drop is zero, a measure of the accuracy of the theoretical model for c_{21}/c_{11} was obtained. In a similar manner, it can be shown that

$$\frac{V_i}{V_{i-2}} = -\frac{c_{31}}{c_{11}} \quad .$$

Measurements were made for the conditions listed in the main report, and a family of curves was obtained for V_i/V_{i-1} and V_i/V_{i-2} as functions of drop rate (f) and spacing (λ). Because the initial drop shape departs significantly from a sphere at the lower frequencies and the effective drop spacing from the standpoint of the capacities is less than λ, empirical correction factors were derived from the data to correct the model. To correct the ratio c_{21}/c_{11}, the factor k_1 was derived, with

$$k_1^{-1} = 1.20 + 0.194 \times 10^{-4} f \quad ;$$

and to correct $\dfrac{c_{31}}{c_{11}}$,

$$k_2^{-1} = 0.70 + 0.403 \times 10^{-4} f \quad .$$

Combining the above relations yields the final form for the factors F_1 and F_2:

$$F_1 = -\frac{c_{21}}{c_{11}} k_1 = \frac{\ln(4d_x/\pi d_d)\sinh\beta_1 \sum\limits_{n=1}^{6} \operatorname{csch}(2n\beta_1)}{(1.20 + 0.194 \quad 10^{-4} f)} \quad ,$$

146

$$F_2 = -\frac{c_{31}}{c_{11}} k_2 = \frac{\ln(4d_x/\pi d_d)\sinh\beta_2 \sum\limits_{n=1}^{6} \operatorname{csch}(2n\beta_2)}{(0.70 + 0.403 \times 10^{-4}\, f)} \quad.$$

The charging capacitance $C = -c_{41}$ is the same as in Sweet's model and is given by

$$c_{41} = -2\pi\epsilon\lambda/\left[\ln(4d_x/\pi d_{jo})\right] \quad,$$

where ϵ is the permitivity of free space.

147

Appendix D

PHI EQUATIONS

Appendix D

PHI EQUATIONS

The equations in this appendix are used to compute the potential at
(x, y)-coordinates between and near the deflecting plates for the parallel
and nonparallel plate cases. The field is assumed to be two-dimensional.
The coordinate system used in PHI differs from that used in the executive
routine and is shown in Figure D-1. The origin is located at the edge
of the lower plate that is nearest the orifice. Furthermore, the coor-
dinate system is scaled such that the distance between the plates is
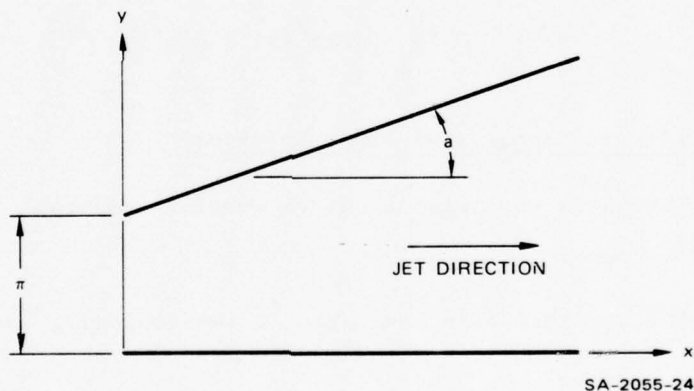always π. The potential field itself is called $\varphi(x, y)$.

SA-2055-24

FIGURE D-1   COORDINATE SYSTEM AND SCALING CONVENTION IN PHI

1.   Semi-Infinite Parallel Plate Solution

In this case, the potential field can be specified without using
complex numbers, although trigonometric and hyperbolic functions are
included. The solution for $y \leq \pi/2$ reads

151

$$\varphi(x, y) \;=\; V_o \left\{ \frac{1}{2} - \frac{1}{\pi} \arccos(q) \right\} \quad,$$

and for $y > \dfrac{\pi}{2}$ reads

$$\varphi(x, y) \;=\; V_o \left\{ 1 - \frac{1}{\pi} \arcsin(q) \right\} \quad.$$

In these equations, V_o is the potential difference between the plates, q is given by

$$q \;=\; \frac{A}{B}, \text{ and } A \;=\; \exp(x/2)\,\sin(y)$$

$$B \;=\; \left[\sinh(x) + C \right]^{1/2}$$

$$C \;=\; \left[\sinh^2(x) + \sin^2(y) \right]^{1/2} \quad.$$

2. <u>Semi-Infinite Nonparallel Plate Solution</u>

The solution in this case requires several conformal transformations and complex algebra.

A complex variable W is evaluated in the following way:

$$W \;=\; \left[A \cos^t(a) + B \right]/C \quad,$$

where

$$A = (1 + b)^t$$

$$B = 1/2 \left[1/2 - \cos^t(a) \right]$$

152

$$C = 1/2[1/2 + \cos^t(a)]$$

$$t = \pi/a$$

$$b = (z/\pi) \tan(a)$$

$$z = x + iy$$

Here a is the angle between the deflection plates. The real and imaginary parts of W are designated U and V, respectively.

The second variable is defined as

$$S = 1/2[(r^2 - 1) - [(r^2 - 1 + 4V^2)^{1/2}] \quad ,$$

where r denotes the scaler magnitude of the complex variable W.

For U > 0, the potential solution is given by

$$\varphi(x, y) = V_o\left[\frac{1}{2} - \frac{1}{\pi} \arccos(V/S)\right] \quad .$$

For U ≤ 0, the solution is

$$\varphi(x, y) = V_o\left[1 - \frac{1}{\pi} \arcsin(V/S)\right] \quad .$$

153

Appendix E

AERO DERIVATION

Appendix E

AERO DERIVATION

1. Results

The drag on a single sphere in flight is given by[7]

$$(C_D)_{ss} = \frac{24}{R_e} + \frac{4}{(R_e)^{1/3}} \quad , \tag{1}$$

where

$$R_e = \text{Reynolds Number} = \frac{\rho_a d v_o}{\mu_a} \quad ,$$

and

ρ_a = air density

μ_a = air viscosity

d = drop diameter

v_o = drop speed .

If the drop in question has neighbors in flight, the two preceding drops and the one following modify the drag coefficient, such that

$$C_D = C_D^* \cdot (C_D)_{ss} \quad .$$

The equation for the modifier, C_D^*, is a function of separation and off-set distances from the neighboring drops. Its value is given by

$$C_D^* = 1 - 0.84 \exp(-y_o/d) - \left[1 - \exp(-y_o/d)\right]\left[(C_D)_{1L} + (C_D)_{2L} = (C_D)_{1T}\right]$$

157

and

$$(C_D)_{1L} = 0.435 \exp \left[-0.020(\lambda_1/d) - 0.188(\eta_1/d)^2 \right] \quad ,$$

$$(C_D)_{2L} = 0.178 \exp \left[-0.022(\lambda_1'/d) - 0.188(\eta_1'/d)^2 \right] \quad ,$$

$$(C_D)_{1T} = 0.217 \exp \left[-0.147(\lambda_2/d) - 0.188(\eta_2/d)^2 \right] \quad . \tag{2}$$

Notation is illustrated in Figure E-1. The subscripts refer to the effects of leading and trailing drops. The terms containing $\exp(-y_o/d)$ account for the nearness of the drop to the undeflected jet.

If one denotes the coordinates of the drop under consideration by (x_o, y_o, z_o), those of the first leading drop by (x_1, y_1, z_1), the second leading drop by (x_1', y_1', z_1'), and the first trailing drop by (x_2, y_2, z_2), then the λ's and η's can be calculated by using the following equations.

$$\lambda_1 = \sqrt{(x_1 - x_o)^2 + (y_1 - y_o)^2 + (z_1 - z_o)^2} \tag{3}$$

$$\lambda_1' = \sqrt{(x_1' - x_o)^2 + (y_1' - y_o)^2 + (z_1' - z_o)^2} \tag{4}$$

$$\lambda_2 = \sqrt{(x_o - x_2)^2 + (y_o - y_2)^2 + (z_o - z_2)^2} \tag{5}$$

$$\theta_1 = \cos^{-1} \left[\frac{(x_1 - x_o)\dot{x}_1 + (y_1 - y_o)\dot{y}_1 + (z_1 - z_o)\dot{z}_1}{\lambda_1 \sqrt{\dot{x}_1^2 + \dot{y}_1^2 + \dot{z}_1^2}} \right] \tag{6}$$

$$\theta_1' = \cos^{-1} \left[\frac{(x_1' - x_o)\dot{x}_1' + (y_1' - y_o)\dot{y}_1' + (z_1' - z_o)\dot{z}_1'}{\lambda_1' \sqrt{\dot{x}_1'^2 + \dot{y}_1'^2 + \dot{z}_1'^2}} \right] \tag{7}$$
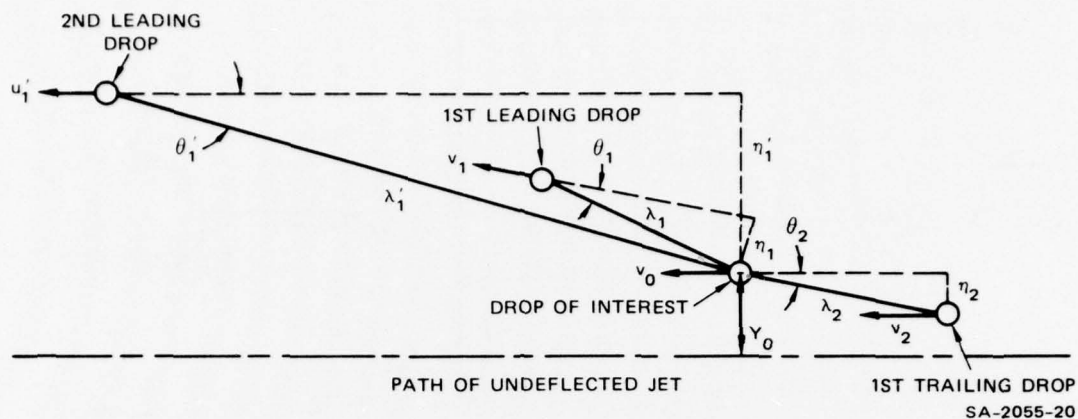
158

FIGURE E-1 DROP SEPARATION AND OFFSET DISTANCES

$$\theta_2 = \cos^{-1}\left[\frac{(x_o - x_2)\dot{x}_o + (y_o - y_2)\dot{y}_o + (z_o - z_2)\dot{z}_o}{\lambda_2\sqrt{\dot{x}_2^2 + \dot{y}_2^2 + \dot{z}_2^2}}\right] \quad (8)$$

$$\eta_1 = \lambda_1 \sin \theta_1 \quad (9)$$

$$\eta_1' = \lambda_1' \sin \theta_1' \quad (10)$$

$$\eta_2 = \lambda_2 \sin \theta_2 \quad . \quad (11)$$

Once the modififed drag coefficient has been found, drag force on the drop is determined from the relation

$$D = \frac{\pi}{8} \rho_a d^2 C_D v_o^2 \quad .$$

2. Drag Coefficient Determination

When operating correctly and under the illumination of a stroboscopic light flashing at submultiples of the crystal driving frequency, the stream of drops originating from the print head appears frozen in space as shown in Figure E-2. Also seen in that figure is a single drop being

159

DEFLECTED DROP

v'

x'

δ

λ

INK JET
HEAD

$v = dx/dt$

$t = 0$
$x = 0$
$v = v_o$

x
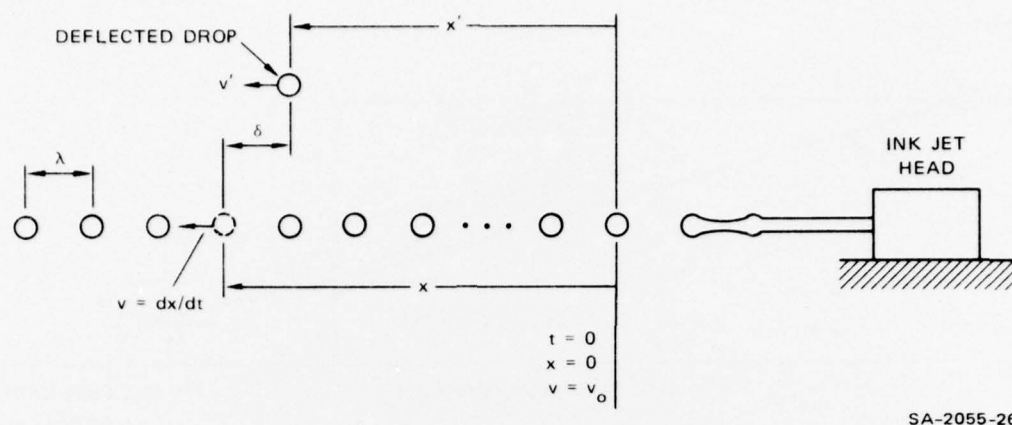
SA-2055-26

FIGURE E-2   INK JET SEEN UNDER STROBOSCOPIC LIGHT

charged and deflected away from the column of uncharged drops. From such
a "still" picture, various physical dimensions, such as the drop diameter
d, the regular drop-to-drop spacing in the column λ, and the displacement
of the deflected drop from its original position δ, can be measured
readily.

A less obvious but nonetheless easily deducible parameter from such
a picture is the time for each drop to reach its present location from
the drop separation point, or from any other reference point. For ex-
ample, it takes 1/f second (f being the crystal driving frequency in Hz)
for a drop in the column to travel from its present location to the loca-
tion now occupied by its neighboring drop on the left. It will take this
drop n/f second to reach a distance n spacings downstream. For the de-
flected drop, its position in time with respect to other drops can be
determined by its original location in the column. Furthermore, its
position in space 1/f second later can be found by returning this drop
to its original position in the column and instead deflecting the next
drop to its left with the same charging and deflection voltages.

160

By using the information and drop manipulation technique just described, motion of any drop can be measured. As it turned out, the ability to measure drop motion alone was not sufficient to determine reliable drag coefficient data. It was necessary to use a more subtle approach in selecting the exact quantities to measure. As an example, one of the unsuccessful measuring schemes used the most obvious method of measuring the absolute position of a drop versus time in which drop deceleration would then be an indication of drag forces and coefficient. The problem with this seemingly straightforward method is that the absolute positions of the drops do not remain fixed (slight drifting or oscillation of drops caused by slow pressure variation, natural draft in the room, or other factors is observed). The percentage error in the position measurement exceeded the percentage reduction in drop velocity due to aerodynamic drag. As a result, the calculated drag coefficient was untrustworthy.

The technique eventually adopted entailed the measurement of a drop displacement from its undeflected position in the column versus time. More specifically, two separate measurements were required. First the velocity versus time of the interested drop is measured while it is still in column. Then, its lag in the streamwise direction as a function of time after it has been deflected away from the column is noted. Referring to Figure E-2, the first measurement gives us $v(t)$. When all the drops lie in a single column, the drag experienced by each drop is not only much lower than the single sphere drag but also constant for all practical purposes. Because of this, the measured $v(t)$ can be fitted by an expression of the form

$$v(t) = v_o (1 - ct) \quad , \qquad (12)$$

where c is a constant determinable by the measured data. The second measurement gives $\delta(t)$. As can be seen in Figure E-2

161

$$\delta = x - x' \quad . \tag{13}$$

Hence

$$\frac{d\delta}{dt} = \frac{dx}{dt} - \frac{dx'}{dt} = v - v' \quad , \tag{14}$$

$$\frac{d^2\delta}{dt^2} = \frac{dv}{dt} - \frac{dv'}{dt} \quad . \tag{15}$$

Now

$$\frac{dv}{dt} = -cv_o \quad , \tag{16}$$

and

$$\frac{dv'}{dt} = -\frac{D}{m} = -\frac{3}{4} \frac{\rho_a}{\rho_\ell} \frac{v'^2}{d} C_D \quad , \tag{17}$$

where D is the drag, m is the mass of a single drop, ρ_a and ρ_ℓ are the densities of air and liquid ink, respectively, and C_D is the drag coefficient. Combining Eqs. (12) through (17), one obtains

$$C_D = \frac{4}{3} \frac{\rho_\ell}{\rho_a} d \frac{\frac{d^2\delta}{dt^2} + cv_o}{\left[v_o(1 - ct) - \frac{d\delta}{dt} \right]^2} \quad . \tag{18}$$

This is the fundamental equation used to calculate C_D once $v(t)$ and $\delta(t)$ have been measured.

With respect to Figure E-2, it is shown that the position of the first detached drop is chosen to be $x = o$ and the corresponding time to be $t = o$. This is not essential. In fact, any drop in the column can be selected to be the origin as long as both $v(t)$ and $\delta(t)$ are measured against the same origin and v_o is the drop velocity at the selected origin.

162

3.   Ink Drop Measurements

Given the above background, the actual measuring procedure was as follows.   The method of measuring v(t) is illustrated in Figure E-3.
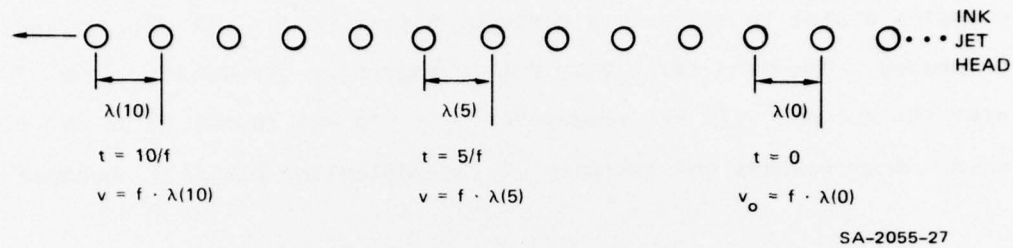

FIGURE E-3   METHOD OF MEASURING v(t)

It amounts to keeping track of the numerical order of a particular drop from the chosen origin and measuring its spacing from the neighboring drop. A typical result of such measurements is shown in Figure E-4.   Such a plot
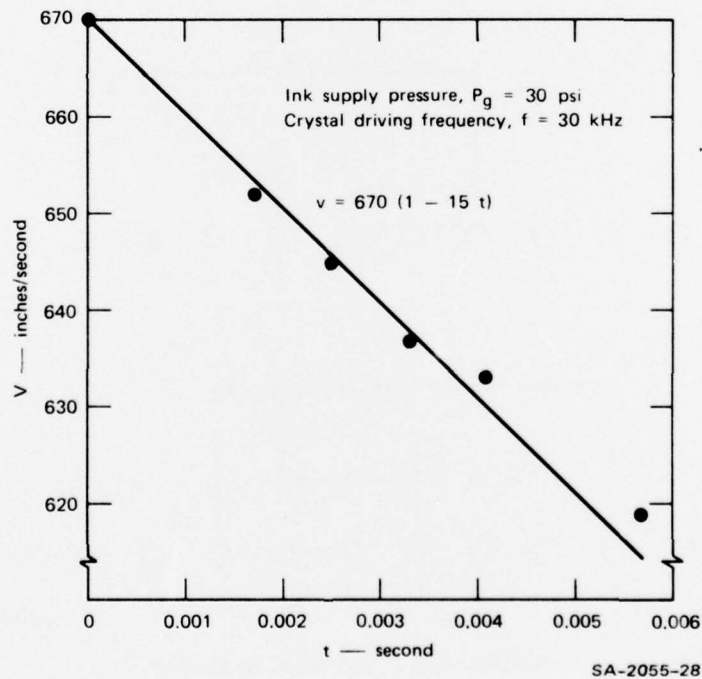

FIGURE E-4   VELOCITY OF A DROP IN THE COLUMN

163

is applicable to any one of the drops in the column as long as the ink supply pressure and the crystal driving frequency are unchanged.

The measurement of $\delta(t)$ is shown in a sequence of illustrations in Figure E-5. The top illustration shows that a drop that originally occupies a slot in the column corresponding to $t = t_1$ is charged and deflected. The drop falls back due to increased aerodynamic drag outside the column. (In all measurements, $t = o$ was chosen to be the time when a drop reaches the entrance of the deflection plates.) Because the
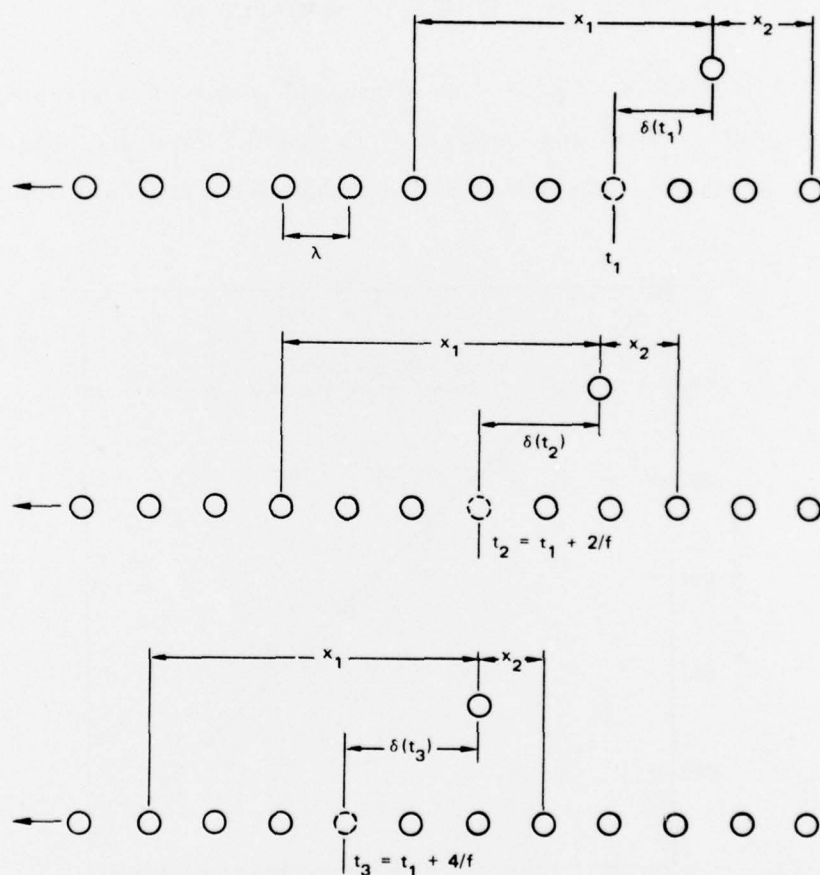
SA-2055-29

FIGURE E-5 $\delta(t)$ MEASUREMENT

164

drop is absent from its original position, $\delta(t_1)$ cannot be directly measured. Instead, x_1 and x_2 are measured, and

$$\delta(t_1) = \frac{1}{2} (x_1 - x_2) \qquad . \qquad (19)$$

This procedure is permissible because λ remains practically constant within a span of 10 or even 20 drops.

Once $\delta(t_1)$ is obtained, this drop is returned to its original position by nullifying its charging voltage. Then another drop n spacings down from the first drop is deflected (n is equal to 2 in the example shown), with the same charging and deflection voltages. The position occupied by this newly deflected drop is then the exact position that the first drop would have occupied at $t_2 = t_1 + n/f$; $\delta(t_2)$ is then measured. This process is repeated a number of times so that δ as a function of t can be plotted. One example of such a plot is shown in Figure E-6. The fact that δ is proportional to t^2 indicates that deceleration, and hence the drag experienced by the drop is constant within the time period of measurement, i.e., from t = 2.0 to 2.33 ms.

Having obtained v(t) and $\delta(t)$ (shown in Figures E-4 and E-6, respectively), C_D can then be calculated by using Eq. (18). For the particular example shown, C_D is equal to 0.71. Note that this entire series of measurements is necessary to compute a single value of C_D.

4.   Cases Studied
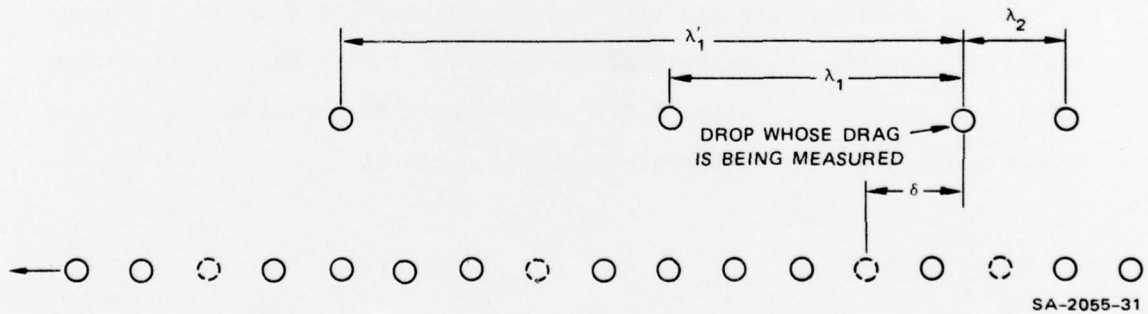
Four cases were studied. They are:

• Drop shielded by one preceding drop

• Drop shielded by two preceding drops

• Drop shielded by two preceding drops and followed by one drop

• Effect of offset.

165
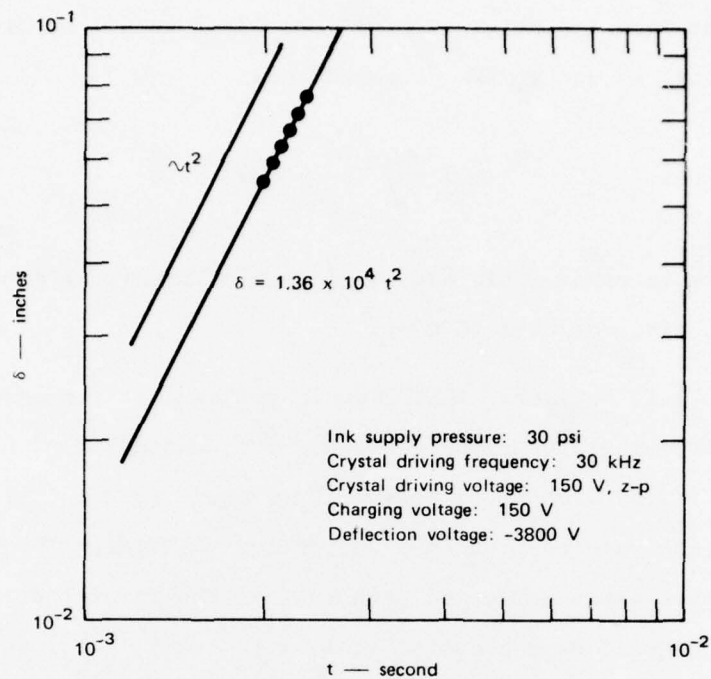
FIGURE E-6   δ VERSUS t

Figure E-7 illustrated how the drop measurements were made in case (3).

FIGURE E-7   CASE OF ONE DROP SHIELDED BY TWO LEADING AND ONE TRAILING DROP

To examine the effect of offset, the experiment illustrated in Figure E-8 was performed. One drop is first deflected to a fixed height above the column. Then by varying the charging voltage on a drop
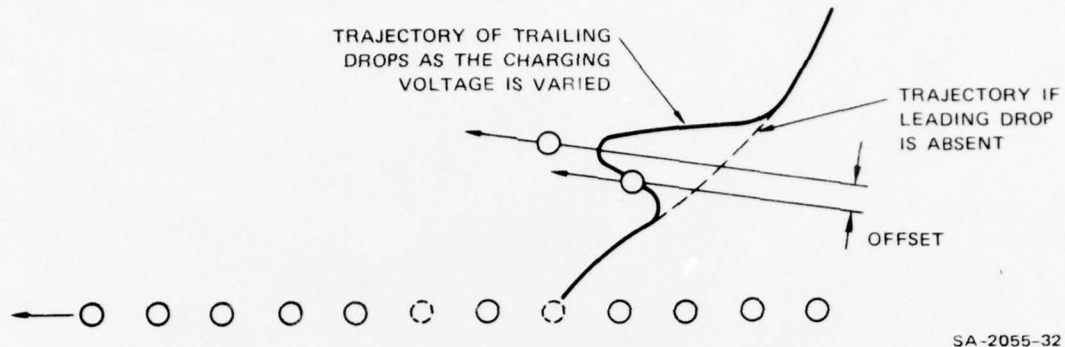
166

FIGURE E-8   WAKE WIDTH OF LEADING DROP EXPERIMENT

following in the column, the trajectory of this latter drop is traced.
As shown in Figure E-8, at a certain offset distance, the wake of the
leading drop begins to be felt by the trailing drop, causing its tra-
jectory to deviate from the one that it would have been following if
the leading drop were absent. From such a measurement, the shielding
effect as a function of the offset distance can be obtained.

The effect of the nearness of the drop in question to the undeflected
stream was found by noting the trajectory of a single charged drop as its
distance from the undeflected jet increased. Plotting such data yielded
the exponential term cited earlier.

An empirical formula was derived to fit the data collected under
all conditions. (Table 2 in Sec. III-D-10 summarized these data.) The
empirical formula, with its variables normalized, is given at the begin-
ning of this appendix.

167

REFERENCES

1. "Evaluation of A. B. Dick Videojet Ink 16-6000 Under Various Conditions," Report to DoD Contract DAAB03-72-C-0078, A. B. Dick Company, Chicago, Ill.

2. J. E. Funk, D. J. Wood, S. P. Chao, "The Transient Response of Orifices and Very Short Lines," Journal of Basic Engineering, Transactions of the ASME, pp. 483-491 (June 1972).

3. Lord Rayleigh, The Theory of Sound, Vol. 2, Dover Publications, Inc., New York, Section 357.

4. "High Frequency Oscillography with Electrostatically Deflected Ink Jets," Richard G. Sweet, Technical Report No. 1722-1, Stanford Electronics Laboratories, Stanford University, Stanford, Ca. (March 1964).

5. Morse and Feshbach, Methods of Theoretical Physics, McGraw Hill Book Co., New York, pp. 1245-1247 (1953).

6. H. Kober, Dictionary of Conformal Representations, p. 85ff, Dover, New York (1952).

7. L. B. Tarabin and W. H. Gauvin, "Fundamental Aspects of Solid-Gas Flow; Part 1-Introductory Concepts and Idealized Sphere Motion in Viscous Regime," Can. J. Chem. Eng., pp. 129-141 (August 1959).

8. Sir Horace Lamb, Hydrodynamics, Dover Publications, Inc., Section 265, New York (1945).